UNIVERSITÀ
DEGLI STUDI
FIRENZE

DOTTORATO DI RICERCA IN
Tecnologie Elettroniche per l'Ingegneria dell'Informazione

CICLO XXVI

COORDINATORE Prof. Piero Tortoli

High Framerate Imaging of Ultrasound Contrast Agents

Settore Scientifico Disciplinare ING-INF/01

Dottorando
Dott. *Jacopo Viti*

Tutore
Prof. *Piero Tortoli*

Co-tutore
Prof. dr. *Nico de Jong*

Coordinatore
Prof. *Piero Tortoli*

Anni 2011/2014

High Framerate Imaging of Ultrasound Contrast Agents

JACOPO VITI

Cover Design: Jacopo Viti

A digital version of this thesis is available at http://repub.eur.nl/pub/

ISBN 979-12-200-0605-7

High Framerate Imaging of Ultrasound Contrast Agents

Thesis

to obtain the degree of Doctor from the
Erasmus University Rotterdam
by command of the Rector Magnificus

Prof.dr. H.A.P. Pols

and in accordance with the decision of the Doctorate Board

The public defense shall be held on
Wednesday 20th of January, 2016, at 11:30 hours
by

Jacopo Viti
born in Firenze, Italy

Erasmus University Rotterdam

Doctoral Committee

Promotors:	Prof.dr.ir. N. de Jong Prof. P. Tortoli
Other members:	Prof.dr.ir. A.F.W. van der Steen Prof.dr. P.N. Burns Dr.ir. M. Mischi
Copromotor:	Dr.ir. H.J. Vos

.

The work in this thesis was conducted at the Microelecronics System Design Lab of the Department of Information Engineering (DINFO) of the Università degli Studi di Firenze, Firenze, Italy; and at the Department of Biomedical Engineering of Thorax Center of the Erasmus Medical Center, Rotterdam, The Netherlands

Contents

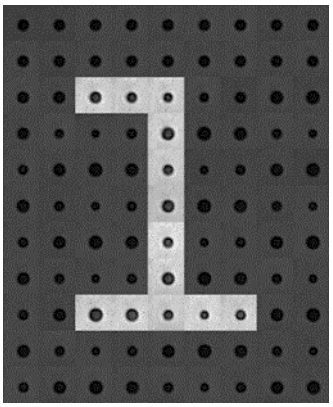

1. Introduction

1.1. BLOOD IMAGING CHALLENGES

Imaging blood with a conventional ultrasound scanner is quite hard, if not impossible. The typical B-Mode images that are obtained when scanning an artery with standard 7.5 MHz linear arrays are similar to the one shown in Figure 1:1. This presents a black area in correspondence of blood. The main reason for this behavior is that blood is mostly composed by plasma, that is poorly echogenic, whereas the scattering of ultrasound is solely due to the various particles suspended in it. The greatest portion of these particles is comprised of the red blood cells (erythrocytes), biconcave disks with diameter, D, in a range around 7 μm. Hence, in a Rayleigh scattering regime (i.e., where D is much smaller than the ultrasound wavelength, λ), only a small portion of the transmitted energy is redirected back to the probe that generated it, and the echoes coming from blood are thus very small, typically 40 to 60 dB more faint than the echoes generated by the vessel walls. Therefore, if the information of the red blood cells is to be preserved, the ultrasound scanner must comply with extremely restrictive constraints in terms of sensitivity and noise figure.

However, there are also cases in which blood becomes "visible" by ultrasound. This happens in large veins, that may produce impressive images like the one seen in Figure 1:2. Actually, the speckle pattern that can be seen here is due to the low shear rate typical of venous flow, which leads to red blood cell aggregation. Hence, in venous flow we mostly observe erythrocyte aggregates rather than individual particles.

The individual red blood cells, in theory, could be imaged using very high ultrasound frequencies, by taking advantage of the principle that Rayleigh scattering is proportional to the 4^{th} power of the incident frequency. However, attenuation also

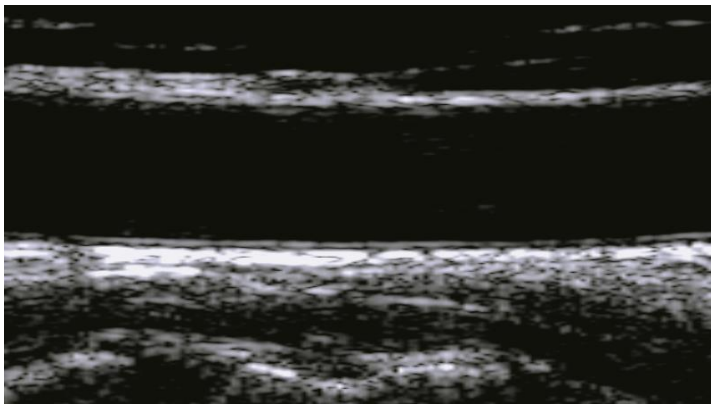

Figure 1:1 Ultrasound B-Mode image of carotid artery on a healthy volunteer. Flowing blood appears as a solid black area inside of the vessel walls.

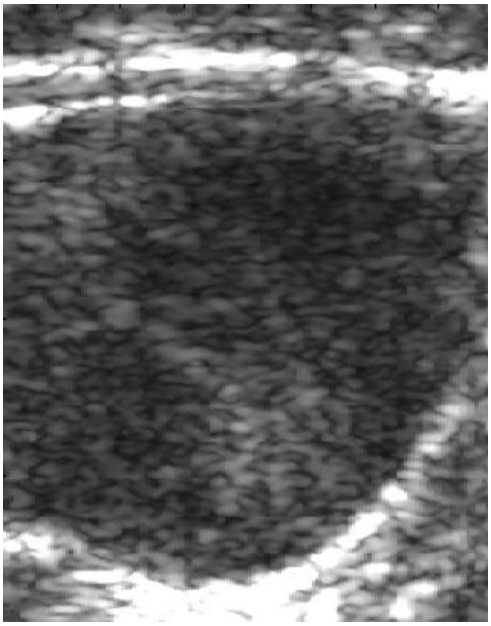

Figure 1:2 Ultrasound B-Mode of the cross-section of a jugular vein. Blood speckle, due to the aggregation of red blood cells, is here visible within the vessel walls.

increases with the frequency, and such an approach could only be valuable for imaging superficial vessels, while deep arteries would continue to appear as dark regions.

1.2. Blood Imaging Methods

The direct visualization of blood by ultrasound may be useful for the early detection of cardiovascular diseases as well as of cancer, which yields an abnormal growth of blood vessels (angiogenesis). Suitable signal or image processing methods have been developed to pursue this objective.

A first method consists in increasing the signal-to-noise ratio (SNR) by transmitting coded signals and using matched filters in receive. This approach is, e.g., used in the so-called, "B-flow" technique introduced by GE ultrasound, that displays in real time the speckle pattern from blood, as shown in Figure 1:3.

An indirect approach for blood visualization exploits the Doppler effect associated to its movement, either pulsatile (in arteries) or quasi-steady (in veins). In these cases, colors are used to highlight the regions where blood movement is detected (e.g. by means of color and power Doppler modes). However, it should be remarked that such colors do not directly identify the red blood cells, but rather their movement.

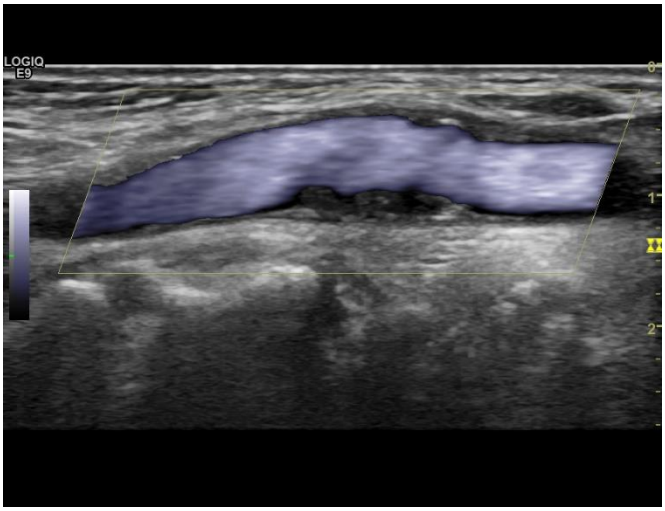

Figure 1:3 Example of B-Flow color image of an internal carotid artery with plaque (Courtesy of GE.)
Source:
http://www3.gehealthcare.com/~/media/images/anz_images/ultrasound/logiq%20e9/1-clinical/b%20flow%20color%20ica%20%20plaque%20ml6-15%20-%20kopie.jpg

Another indirect strategy to "fill" the "empty" vessels in B-Mode images is by increasing the contrast between blood and the surrounding tissue. This goal can be achieved by subtracting the echoes received in consecutive pulse repetition intervals: assuming that tissue is static its echoes cancel out after subtraction; on the other hand, since blood is moving, the difference of two (or more) consecutive echo signals will not yield zero.

Finally, an impressive number of methods were proposed after the introduction of Ultrasound Contrast Agents (UCA). UCA are tiny gas microbubbles encapsulated by a (lipid) shell; they are very echogenic and, when hit by ultrasound pulses, generate echo-signals much stronger than red blood cells. It is thus possible to inject an UCA in blood and then, by detecting the echoes of microbubbles suspended in the blood itself, we get an indirect information about the presence of blood. Despite being originally introduced as simple "echo enhancers", the UCA rapidly outgrew their original capability of increasing the contrast between blood and tissue thanks to the generation of non-linear echoes associated with their pulsation. Several techniques were thus proposed, based on non-linear properties of the UCA, and proved to be more sensitive than the traditional imaging approach: harmonic imaging, most notably second harmonic imaging, and subharmonic imaging, relies on detecting the acoustical energy located around frequencies (sub)multiple of the one of the

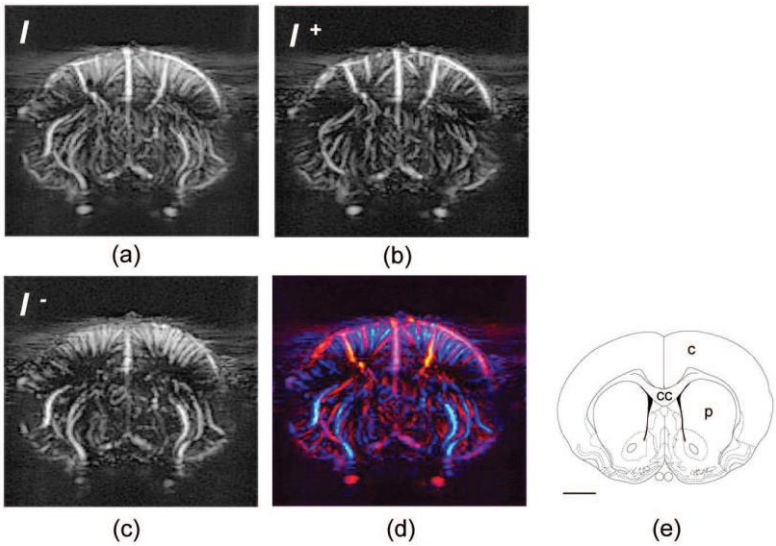

Figure 1:4 Directional power Doppler. (a) Initial µDoppler image. (b) Positive part of the Doppler power spectrum I+ quantifying the volume of blood flowing up. (c) Negative part of the Doppler power spectrum I− quantifying the volume of blood flowing down. (d) Color-coded µDoppler image: in each pixel, the positive part is colored on a red range of intensities and the negative part on a blue range of intensities. (e) Anatomy of the brain slice (bregma + 1.0 mm). ***Reprinted with permission from E. Mace, G. Montaldo, B. Osmanski, I. Cohen, M. Fink, and M. Tanter, "Functional ultrasound imaging of the brain: theory and basic principles," IEEE Transactions on Ultrasonics, Ferroelectrics, and Frequency Control, vol. 60, no. 3, pp. 492–506, Mar. 2013.© 2013 IEEE.***

transmitted tone burst. Multi-pulse imaging techniques, such as pulse-inversion and power-modulation, detect contrast agents by transmitting a coded pulse train, then performing a linear combination of the collected echoes in order to suppress the signal due to linear propagation and scattering, while preserving, or even enhancing, the signal components arising from non-linear phenomena. Additionally, Doppler-based methods such as power Doppler have also been used in conjunction with UCA.

More recently, much attention was dedicated to the so-called high-framerate (HFR) imaging methods, which are capable of producing hundreds or even thousands

of images per second by means of special transmit/receive (TX-RX) strategies. The most popular HFR imaging techniques relies on the transmission of plane waves to insonify a wide region of interest, so that suitable processing of received echo data may allow the production of a full image for each transmitted plane wave.

"Observing" blood at a high frame rate offers interesting opportunities to increase the contrast, both with and without the use of UCA. In particular, HFR imaging allows removing the temporal resolution constraints, which are due to the acquisition time,

typical of color and power Doppler methods. By combining HFR and Doppler algorithms, "ultrafast Doppler" tools were developed, which were successfully employed to obtain impressive images of blood flow in small vessels, as seen Figure 1:4. It is thus expected that the combination of HFR imaging methods with UCA may further improve the indirect visualization of blood.

1.3. THESIS OUTLINE

The general motivation of this thesis is improving the visualization of blood in human arteries through the investigation of optimal methods to increase the Contrast-to-Tissue Ratio (CTR). To pursue such an objective, different approaches were investigated, including the use of non-conventional TX-RX strategies. These were, in most cases, combined with UCA, which are confirmed to be an excellent tool to increase the CTR. The next two chapters are thus dedicated to the description of the Materials (UCA and open ultrasound scanners) used in this Thesis, and to a fundamental study on the behavior of single bubbles during a prolonged ultrasound excitation, respectively. The remaining chapters report on the experimental studies performed by using non standard imaging methods.

The next chapter includes two parts. The first part reviews the main characteristics of UCA, from the methods adopted to improve their stability to the resulting linear and non-linear vibration modes. Special attention is also given to the simulation and experimental methods so far used to describe the behavior of individual microbubbles. The second part focuses on the specific equipment used in the experimental work of this Thesis. Details are provided about the ULA-OP research scanner and the related programming modalities. Finally, the general features of the Brandaris 128 camera, here used to record the behavior of deflating UCA, are described.

Chapter 3 describes the results of the investigation of the behavior of isolated microbubbles during prolonged ultrasound excitation. Isolated microbubbles placed in a thin capillary tube were excited with hundreds of pulses at a low mechanical index, and their oscillations were recorded using the Brandaris-128 ultra high-speed camera. Results show that the microbubbles undergo an irreversible, non-destructive deflation process occurring in discrete steps, with both symmetric and asymmetric radial oscillations around the resting. Strongly asymmetric oscillations, such as compression-only and expansion-only behavior, were also observed, with an expansion-only behavior associated with a rapid size reduction, whereas a compression-only behavior mostly occurs without a noticeable change of the bubble radius.

In Chapter 4, two novel imaging methods are introduced, both characterized by the exploitation of different transmit or receive frequencies for image formation. In the first method, parallel beamforming in transmission is obtained by means of orthogonal frequency division multiplexing (OFDM) implemented on ULA-OP. A 3-fold frame rate increase is obtained with axial resolution of about 2 mm and 1 mm in fundamental and harmonic imaging, respectively. The second study investigates the CTR and signal-to-noise ratio (SNR) of superharmonic UCA scattering in a tissue/vessel mimicking phantom. The results indicate that noise, rather than the tissue signal, is the limiting factor for the UCA detection when using the superharmonics, i.e. the third or higher harmonics.

The following chapters report on the results of experimental investigation of methods addressed to increase the CTR in blood vessel imaging. In Chapter 5, the CTRs measured by using multiple contrast-pulse-sequences (CPS) implemented in the same scanner are reported. This approach permitted to obtain a convenient and consistent evaluation of the main parameters characterizing the various techniques. Chapter 6 evaluates the effectiveness of plane wave transmission with high number of compounding angles on flowing UCA suspensions, as a means to produce good quality images at pressure levels that do not destroy UCA. Ultrafast plane wave imaging is in particular compared to the traditional focused scanning. The influence of the number of compounding angles, peak-negative pressure and flow speed on the final image quality are investigated. The results suggest the feasibility of continuous contrast monitoring at high frame rate. In Chapter 7, a combination of plane-wave transmission with high number of compounding angles and power modulation is shown able to detect even single microbubbles in a realistic phantom setup.

The results of this thesis are further discussed and summarized in the final Chapter 8.

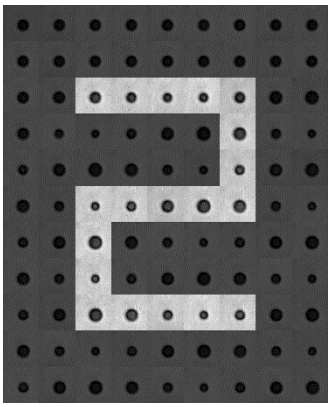

2. Contrast Microbubbles: Background and state of the art.

Different parts of this chapter were based on:

- K. Kooiman, H.J.. Vos, M. Versluis, N. de Jong, "Acoustic behaviour of microbubbles and implications for drug delivery", Adv Drug Deliv Rev. 2014;72:28-7248;
- Jong, N., M. Emmer, et al. (). "Ultrasonic characterization of ultrasound contrast agents." Med Biol Eng Comput 2009, 47(8): 861-873;
- T. Faez, M. Emmer, K. Kooiman, M. Versluis, A. F.W. van der Steen, and N. de Jong, "20 years of ultrasound contrast agent modelling"; IEEE trans ultras ferr, 60 (1): 7 – 20;
- J. Sijl, E. Gaud, P.J.A. Frinking, M. Arditi, N. de Jong, M. Versluis and D. Lohse, "Acoustic characterization of single ultrasound contrast agent microbubbles", J Acoustical Soc Am 2008, 124(6): 4091- 4097

2.1. MICROBUBBLE VIBRATION

2.1.1. Introduction

Normally blood is a poor ultrasound scatterer and it remains relatively dark in an echo image. In 1968, it was reported by Gramiak and Shah [1] that the injection of agitated saline in the aortic root resulted in "a cloud of echoes between the undulating margins of the aortic root" [1]. These gas `mini bubbles' in the agitated saline greatly increased the backscattered ultrasound, and resulted in an enhanced contrast between the aortic root wall and the blood. Nowadays, agitated saline is still used for the detection of right-to-left shunts in the heart [2].

Before gas bubbles could be widely applied as ultrasound contrast agent (UCA), some improvements were necessary. Bubbles produced by agitation are both large and unstable. A gas bubble is unstable and tends to decrease in size due to the surface tension between the gas core and the surrounding liquid. Moreover, the gas bubbles are effectively removed by the lungs. Unless administered by intracoronary or aortic root injection, the bubbles are unable to traverse the pulmonary circulation to opacify the left cardiac chambers. Thus to be useful in an echography study, the bubbles should persist in solution for several minutes and have a size smaller than 10 μm in diameter to be able to enter into the systemic circulation after an intravenous injection.

It was empirically found that a small admixture of the patient's blood to the saline improves the stability and effectiveness of the agitated saline as a contrast agent [6]. Surfactants from the blood form a coating around the gas core and promote the lifetime of the microbubble by greatly reducing the surface tension at the interface. Although this phenomenon was known for many years, it was not before the end of 1980s that sufficiently stable microbubbles were marketed. In 1994 the first commercially available contrast agent, approved for human use in the USA, Albunex (Molecular Biosystems, San Diego, CA, USA), was up for sale. Albunex has a coating made of human serum albumin. The albumin coating forms an elastic solid shell around the gas core and is relatively stiff. It enhances the bubble's stability by supporting a strain to counter the effect of the surface tension, which is different compared to the nowadays more commonly used lipid coatings that act as surfactants.

The second commercial contrast agent, Levovist, was available soon after Albunex in Europe and Japan in 1996. Levovist (Bayer Schering Pharma AG, Berlin, Germany) consists of galactose microcrystals whose surfaces provide absorption sites on which air bubbles form when suspended in water. A trace amount of palmitic acid further stabilizes Levovist microbubbles. Since 1997 contrast agents are further stabilized by replacing the air core with high-molecular-weight inert gases such as SF_6, C_3F_8, or C_4F_{10},

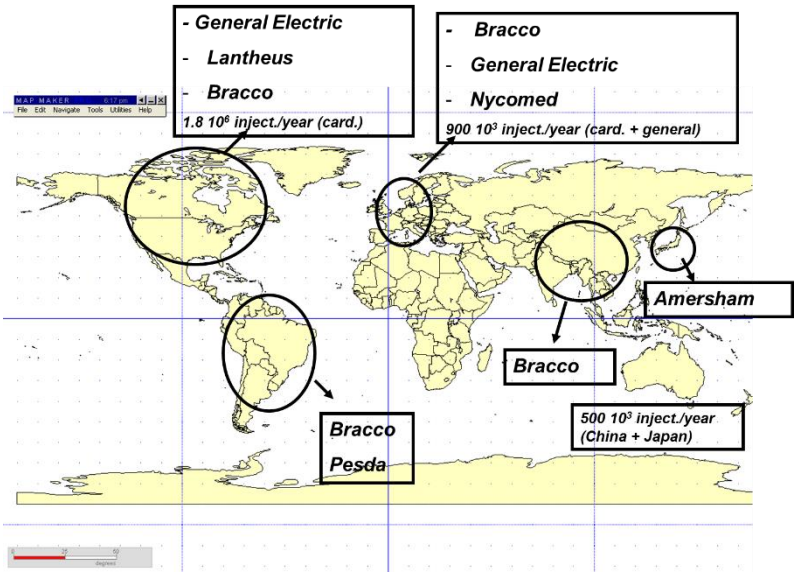

Figure 2:1 The use of ultrasound contrast agents over the world ***source: "20 years of ultrasound contrast agent modelling" Marcia Emmer, Telli Faez, Klazina Kooiman, Michel Versluis, Antonius F.W. van der Steen, and Nico de Jong***

which improve longevity as a result of low solubility in the surrounding medium, compared to air in liquid [5]. The inert gases are exhaled after several passes through the lungs. Examples of these kinds of agents are Optison (GE Healthcare, Chalfont St Giles, UK) that contains octafluoropropane and an albumin shell and SonoVue (Bracco, Milan, Italy) that has a sulfur hexafluoride core and a phospholipid coating. In the latter case the bubbles are not only efficient scatterers due to the stable gas core [7], but also the relative flexibility of the lipid coating allows large bubble vibrations at low acoustic pressures without immediate bubble destruction [8, 9]. The gas bubbles are coated with a lipid, polymer, sugar or protein [8, 10, 15]. The coating reduces the surface tension, and corresponding capillary pressure that forces the gas into solution. Moreover, it provides a gas diffusion barrier.

An overview of currently clinically available contrast agents is given in Figure 2:1.

The ultrasound contrast agents consist of gas microbubbles dispersed in a solution (see Figure 2:2), and are administered intravenously. The typical size of clinically approved microbubbles is between 1 and 10 μm in diameter, with a mean diameter of 2 to 3 μm. Because of their size, the microbubbles are contained within the vasculature and can be considered true blood pool agents [7, 16]

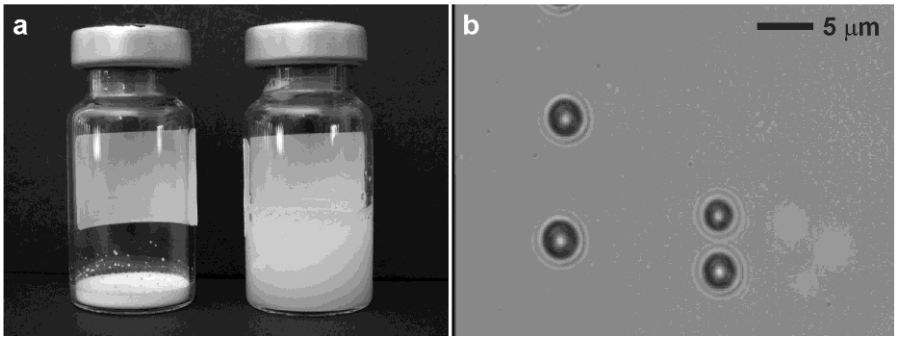

Figure 2:2 a. Contrast agents b. microscopic view

Microbubbles oscillate in a driving pressure field, and for imaging purposes, gas compressibility provides echogenicity with an improvement of several orders of magnitude compared to solid particles of the same size [17, 18]. More intense oscillations will set up an acoustic streaming pattern that may assist in the mixing and delivery of co-administered drugs. Even higher amplitudes of oscillations lead to asymmetrical collapse and jet formation, which may further promote delivery of the co-administered drugs or incorporated payload. An even further increase of the driving pressure may lead to the spontaneous formation of vapor and gas cavities, termed cavitation. Key to the formation of such cavitation bubbles is the presence of pre-existing cavitation nuclei. Stabilized contrast microbubbles provide such nuclei. The 'strength' of the acoustic pressure field and the applied frequency are classified through the mechanical index (MI), and related to the stability of the microbubbles. This relation is based upon the early MI definition by Apfel [19] as follows:

$$MI = \frac{P_N}{\sqrt{f}} \tag{2.1}$$

in which P_N is the peak negative pressure of the ultrasound wave (in MPa), and f the center frequency of the ultrasound wave (in MHz). Even though the MI has a dimension, it is typically reported as a dimensionless number. A value of 1.9 is adopted by the US Food and Drug Administration as the safety limit for clinical ultrasound in the absence of microbubbles. Based on the MI, a classification of microbubble behavior can be given [20]. First, a typical setting for contrast agent imaging (power modulation, pulse inversion, contrast pulsing schemes (CPS), see below) is an MI between 0.05 – 0.2. At higher MIs, between 0.2 and 0.5, destruction of the contrast agent (gas loss, shell material loss, bubble dissolution) causes signal deterioration during a clinical exam, but with the availability of excess gas in the surrounding liquid, these bubbles can sustain stable oscillations during acoustic driving. This regime is

termed the stable cavitation regime. Most of these bubbles dissolve once ultrasound is stopped. An MI above 0.5 is highly destructive for contrast agents [21].

2.1.2. Stability of coated microbubbles

Maintaining a gas bubble at a constant size is technically challenging. Bubbles suspended in a liquid can coalesce, grow or shrink in response to changes in the environment [1]. The surface tension between the gas-liquid interface, the hydrostatic pressure or the acoustic pressure induces consequent diffusion of gas from the gas core into the surrounding liquid. In this way, free gas microbubbles dissolve within seconds after having been introduced in the blood circulation. Smaller bubbles are more susceptible to these influences, because the excess pressure within the bubble that is generated to balance the surface tension inversely scales with the bubble radius, $p\sigma = 2\sigma/R0$. This excess pressure tends to raise the partial pressure of the gas inside the bubble to be greater than the partial pressure of the gas that is dissolved in the surrounding liquid. Using the equation by Epstein and Plesset [2] the dissolution times of gas microbubbles can be calculated, see Table 2-A.

The Ostwald coefficient (L) is an important parameter for the dissolution of bubbles and is defined as the dimensionless ratio of the solubility of the gas in the liquid to the gas density [3]. Gases with lower Ostwald coefficients dissolve more slowly compared to gases with higher Ostwald coefficients. Therefore, the newest generation of contrast agents are composed of high molecular weight gases, such as perfluorocarbons (Definity, Sonazoid, and Optison) or sulfur hexafluoride (SonoVue). The diffusion of a gas is inversely proportional to the square root of its molecular weight, the higher the molecular weight, the slower the solubility or diffusion of the gas. Table 2-A summarizes the Ostwald coefficients of the different gases used in UCA's and shows the predicted lifetime of a gas bubble with a size of 3 µm in diameter in water. It is assumed that the water is saturated with the gas. Clearly, gases with lower solubility provide the bubbles longer persistence. Table 2-A shows that an air bubble dissolves a hundred times faster than a bubble with perfluorohexane, which takes 2 second to dissolve for a 3 µm gas bubble. As reference, it takes at least 12 s for a contrast agent to pass from a peripheral vein (i.e. the site of injection) to the end-organ [5].

Table 2-A Ostwald coefficient and disappearance time for 3 µm diameter bubbles containing different gases

	Ostwald Coefficient ($x10^6$)	**Disappearance time (s) (3 µm)**
Air	23168	0.02
Sulfur hexafluoride (Sf_6)	5950	0.1
Perfluoropropane (C_3F_8)	583	1.1
Perfluorohexane (C_6H_{14})	24	2

Although high molecular weight gases dissolve more slowly compared to air, these free gas microbubbles still do not persist long enough to be of practical use in the human body. A second effective way to slow down dissolution of the microbubbles is the addition of material at the gas-liquid interface. Surfactants such as phospholipids decrease the main driving force for the dissolution of the bubble, which is, as explained above, the surface tension. Other coating materials such as polymers form more rigid encapsulations and support a strain to counter the effect of the surface tension. Current commercially available agents like Sonovue, Definity (both phospholipids), Optison (human albumin), and Sonazoid (lipids) are all coated.

2.1.3. The bubble vibration

The addition of a coating has a strong influence on the microbubble's response to an acoustic pressure. The coating dampens the vibrations of the microbubble and thereby changes the resonance frequency of the microbubbles. This influence of the coating plays a key role in characterizing the behavior of contrast agent microbubbles. Microbubbles in a contrast medium react to an external oscillating pressure field with volume pulsations. Depending on the magnitude of the ultrasound wave, the vibrations will be related either linearly or nonlinearly to the applied acoustic pressure. For very low acoustic pressures, the instantaneous radius oscillates linearly in relation to the amplitude of the applied external pressure field. For higher external field amplitudes, the pulsation of the bubbles becomes nonlinear. In principle, expansion of the bubble is unlimited unlike the compressibility of the bubble.

LINEAR BUBBLE VIBRATION

Let us consider the bubble spherically symmetric and surrounded by a liquid of infinite extent and with constant viscosity (i.e., an uncoated microbubble). The bubble volume is defined by a single variable, the radius, and the motion is assumed to be spherically symmetric. The wavelength of the ultrasound field is assumed to be much larger than the bubble diameter, and only the motion of the bubble surface is of interest. It is assumed that the vapor pressure remains constant during the compression and expansion phases, and that there is no rectified diffusion during the short period of exposure to ultrasound. The gas inside the bubble is assumed to be ideal, and compressed and expanded according to the gas law. At small excitation levels, the displacement of the bubble wall can be compared to the displacement of a simple one-dimensional mass spring oscillator. The oscillator is defined by its mass, restoring force, damping, and applied force. This leads to the equation of motion of the bubble, which is expressed as:

$$m\ddot{x} + \beta\dot{x} + Sx = F_{driv}(t) \tag{2.2}$$

where m is the mass of the bubble-liquid system, β is the mechanical resistance related to the dissipation, S is the stiffness of the system, $F_{driv}(t)$ is the driving force, and x(t) is the radial displacement of the bubble wall relative to the initial radius R0, according to x(t) = R(t) − R0. Since the motion of the bubble is approximated by the simple harmonic oscillation, the bubble then has it own resonance frequency f_r. For an undamped oscillation, it is given by:

$$f_R = \frac{1}{2\pi R}\sqrt{\frac{S}{m}} \tag{2.3}$$

For gas bubbles in a liquid, the stiffness is that of the enclosed volume of gas that acts like a spring when the bubble is disturbed from its equilibrium radius. The inertia is mainly due to the mass of the liquid surrounding the bubble that oscillates with it. Medwin [5] derived values for the mass, the mechanical resistance, and the stiffness as follows:

$$\begin{aligned} m &= 4\pi R_0^3 \rho \\ \beta &= \delta_{tot}\omega m \\ S &= 12\pi\kappa P_0 R_0 \end{aligned} \tag{2.4}$$

where ρ is the density of the surrounding medium, δ_{tot} is the total damping, ω is the angular frequency, κ is the heat capacity ratio (C_p/C_v), and P_0 is the ambient pressure. Substitution of equation 3 into equation 2 gives the final expression for the resonance frequency for a bubble motion without losses,

$$f_R = \frac{1}{2\pi R}\sqrt{\frac{3\kappa P}{\rho}} \tag{2.5}$$

This equation shows that the resonant frequency is inversely proportional to the radius. With the aid of this equation the resonance frequency for various bubbles can be calculated, e.g. for a bubble diameter with a diameter of 4 µm, the resonance frequency in water under normal atmospheric pressure is 1.6 MHz.

The damping β in equation (2.2) is determined by three important parameters responsible for the damping: (1) reradiation damping, (2) damping due to the viscosity of surrounding liquid and (3) thermal damping. The bubble, which can be considered as a secondary source, reradiates ultrasound energy, which decreases the energy of the system. The viscosity of the surrounding fluid, which moves with the bubble wall, causes another source of energy dissipation. Expansion and compression of the bubble cause an increase of the temperature, which results in a net flow of energy outwards into the surrounding medium. The damping coefficients depend on the bubble size and the frequency of the acoustic field and are in the order of 0.1 for bubbles with a diameter between 1 and 10 µm. Exact expressions for the different damping components can be found in [6].

NON-LINEAR BUBBLE VIBRATION

If the bubble vibration becomes larger, equation (2.2) does not hold anymore and more sophisticated models are needed. The bubble model developed by Rayleigh provides the theoretical basis in this section. The bubble is considered spherical, and is surrounded by an incompressible liquid of infinite extent. The liquid is assumed to be Newtonian, so its viscosity is constant. The gas in the bubble is compressed and expanded according to the gas law with the polytropic exponent remaining constant during the vibration. A boundary condition is defined for the pressure at the bubble wall at equilibrium. Solving the equations for the conservation of mass and momentum for the gas and the liquid phase results in the (modified) Rayleigh-Plesset equation, which describes the hydrodynamics of the liquid motion around the bubble. Combining the Rayleigh-Plesset equation and the polytropic gas law with the boundary condition, we obtain the following expression, which describes the motion of an ideal gas bubble and proved to be accurate and robust even in the extreme conditions of sonoluminescence [7],

$$\rho_l\left(R\ddot{R}+\frac{3}{2}\dot{R}^2\right)=\left(p_0+\frac{2\sigma}{R_0}\right)\left(\frac{R}{R_0}\right)^{-3\kappa}\left(1-\frac{3\kappa}{c}\dot{R}\right)-\frac{2\sigma}{R}-\frac{4\mu\dot{R}}{R}-p_0-P_{ac}(t) \tag{2.6}$$

where R, $\dot{R}$ and $\ddot{R}$ represent the radius, velocity and acceleration of the bubble wall, ρl is the density of the liquid, p0 is the ambient pressure, σ the surface tension, κ is the polytropic gas exponent, μ the viscosity of the surrounding water, c is the speed of sound, and $P_{ac}(t)$ the applied acoustic field. For simplicity, only the viscous damping caused by the surrounding liquid has been taken into account.

COATED BUBBLE VIBRATION

Encapsulation of the bubbles dramatically changes their acoustical behavior. The shell causes an increase in resonance frequency due to its stiffness and an increase in damping due to its viscosity. Encapsulated microbubbles were first modeled by De Jong et al. [7] in 1992 and De Jong and Hoff [8] in 1993, incorporating experimentally determined elasticity and friction parameters into the Rayleigh-Plesset model. Church [9] used linear visco-elastic constitutive equations to describe the shell. Later on, many models were defined to predict the influence of the shell on the bubble's vibration, e.g. [10-13].

Marmottant et al. [14] proposed a model for phospholipid-coated bubbles in which the effective surface tension is variable. The effective surface tension at the bubble wall varies along three linear regimes. These regimes are inspired on low frequency observations of phospholipid monolayers using Langmuir-Blodgett balances [14]. The regimes depend on the bubble area, $A = 4\pi R^2$. The model only needs three parameters to describe the effective surface tension: the buckling area of the bubble, $A_{buckling}$, below which the surface buckles, the elastic modulus χ that gives the slope of the elastic regime and the critical break-up tension, $\sigma_{break\text{-}up}$, which predicts the bubble area at which the coating ruptures, with the result that the effective surface tension saturates at σ_{water}. These three regimes can be expressed as follows:

$$\sigma(R) = \begin{cases} 0 & if\ R \le R_{buckling} \\ \chi\left(\dfrac{R^2}{R_{buckling}^2} - 1\right) & if\ R_{buckling} \le R \le R_{break-up} \\ \sigma_{water} & if\ R \ge R_{ruptured} \end{cases} \tag{2.7}$$

Including this effective surface tension σ(R) in equation 5 for the free bubble, and adding an extra viscosity term $4\kappa_s/R^2$ for the coating, results in the equation of motion for a phospholipid-coated bubble:

$$\rho_l\left(R\ddot{R} + \frac{3}{2}\dot{R}^2\right) = \left(p_0 + \frac{2\sigma(R_0)}{R_0}\right)\left(\frac{R}{R_0}\right)^{-3\kappa}\left(1 - \frac{3\kappa}{c}\dot{R}\right) - \frac{2\sigma(R)}{R} - \frac{4\mu\dot{R}}{R} - \frac{4\kappa_s\dot{R}}{R^2} - p_0 . \tag{2.8}$$

For small vibration amplitudes within the tensed elastic state, the surface tension can be linearized around a constant value, with $\sigma(R) \approx \sigma(R0) + 2\chi(R/R0 - 1)$. Implemented in the dynamical equation, it yields the same pressure term $-2\sigma(R)/R = 2\sigma(R0)/R - 4\chi(1/R0 - 1/R)$ as in the model proposed by De Jong et al. [15] for thin elastic shells. The shell stiffness coefficient Sp they introduced is related to the present coating elasticity by $Sp = 2\chi$, while their shell friction coefficient writes $Sf = 12\pi\kappa s$. We stress here again that the model by De Jong et al [15] is limited to small vibration amplitudes for bounded effective tensions between 0 and σ_{break}-up, or for R in between $R_{buckling}$ and $R_{ruptured}$,while the present model extends the oscillation to unbounded, large amplitudes.

At small acoustic amplitude, the presented model provides a linear radius response to the pressure similar to other Rayleigh-Plesset models with constant surface tension. Under large pressure amplitude, the bubble will experience an original non-linear response. It will likely buckle in its compression phase which cancels out any surface tension. On the other hand, the surface tension rapidly rises during the expansion phase, and this asymmetry in surface tension provides an asymmetry in capillary pressure, especially strong for small bubbles.

- SIMULATIONS

Now we are going to analyze the vibrations of a free gas bubble and a coated bubble using the model by Marmottant et al. [14]. We calculate the responses of the phospholipid-coated contrast agent Sonovue with and without the coating. The coating elasticity and viscosity of Sonovue were measured with a fast framing camera system by Van der Meer et al.[16] and were: $\chi = 0.55$ N/m and $\kappa s = 2.3$ 10-8 kg/s. The model by Marmottant et al. [14] requires a third parameter, namely $R_{buckling}$, which is the radius at which the bubble starts to buckle. Currently, the value of $R_{buckling}$ has yet to be established. We therefore consider two situations: a) The bubble vibrates solely in its elastic regime and b) upon compression the bubble will buckle, $R_{buckling} / R0 = 1$. We calculate the response of the bubbles to a driving force consisting of a 3-cycle waveform with a peak negative amplitude of 50 kPa and a center frequency of 2 MHz. Such an excitation is typical for a clinically used pulse echo-system driven in the fundamental or harmonic mode. The radius of the simulated bubbles is 2.5 μm. The scattered pressure is calculated 1 cm away from the bubble wall [17].

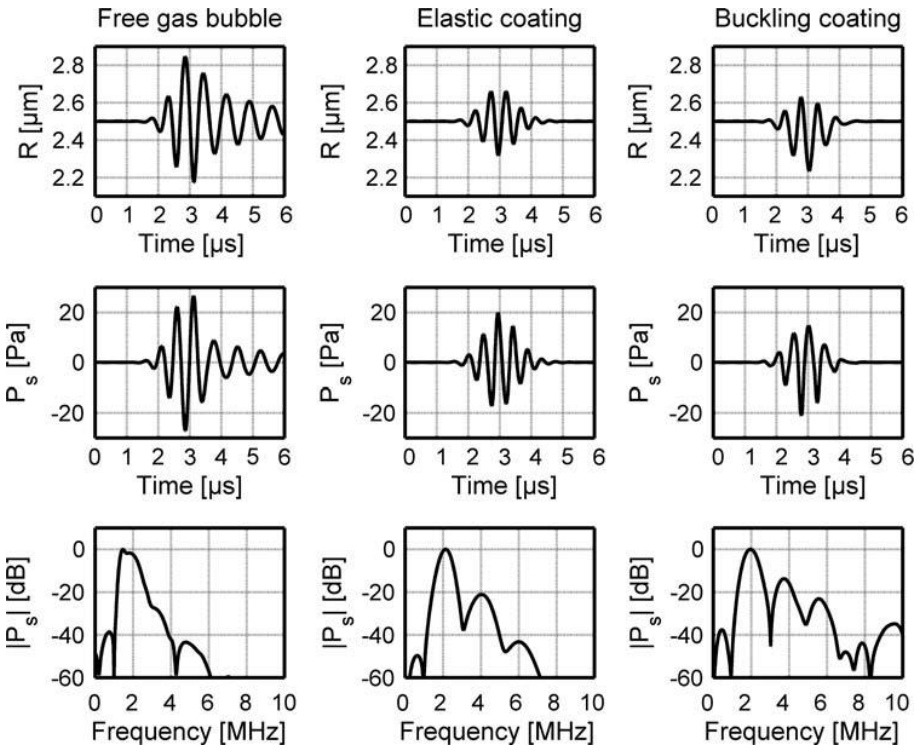

Figure 2:3 Vibration of a 2.5-μm free bubble and coated bubble (v = 0.55 N/m and j_s = 2.3 x 10^8 kg/s.) at 2 MHz in water. Top radial oscillation, Middle scattered pressure at 1 cm, Bottom frequency response of scattered pressure. **{Source: Jong, N., M. Emmer, et al. (2009). "Ultrasonic characterization of ultrasound contrast agents." Med Biol Eng Comput 47(8): 861-873 }**

This yields resonant frequencies of 1.3 MHz for the free gas bubble, 2.2 MHz for the purely elastic coated bubble, and 1.2 MHz for the bubble with a buckling coating. Thus, the bubbles are driven a little below and above their resonant frequency. Figure 2:3 shows the predicted radial motion of the bubbles (R) and the resulting radiated sound pressures (Ps) as a function of time as well as of frequency. The free gas bubble oscillated with the largest amplitude, ΔD = 0.7 μm. The addition of a coating resulted in damping of the oscillation amplitude by a factor of two. The free gas bubble did not immediately stop oscillating after the sound pulse had passed in contrast to the more damped coated bubbles. The effect of coating buckling appears when the results of the elastic coated and buckling coated bubbles are compared. Whereas the elastic coated bubble shows similar expansion and compression phases, the buckling coated bubble expresses a preference for compression. The compression amplitude (0.27 μm) is two times higher than the expansion amplitude (0.13 μm). This asymmetric radial motion leads to elevated subharmonic scattering (at 1 MHz) as is shown in the power spectra of the radiated sound pressures.

2.1.4. Radiation force

Oscillating microbubbles can translate in a medium, through the so-called radiation force [17, 27]. In case of a travelling acoustic wave, the bubbles translate in the direction of wave propagation. In case of a standing acoustic wave, the bubbles translate to nodes or anti-nodes of the acoustic field, depending on the phase difference between the bubble oscillation and the pressure wavefield. For details, the reader is referred to the large amount of literature, e.g., [17, 27].

In mathematical formulation, the radiation force F(t) depends on the volume of the bubble V(t) and the acoustic pressure gradient ∇P(t):

$$F = V \cdot \nabla P \tag{2.9}$$

The equation shows that the force direction is alternating, since ∇P is alternating in direction and V is a positive value. Yet, resonant effects of microbubbles lead to phase differences between the volume oscillation and the pressure gradient. Consequently, the time-averaged force becomes non-zero leading to a translation of the microbubble. The velocity of a freely floating microbubble can reach values up to order of meters per second in case of resonant microbubbles in water, compensated by the duty cycle of the pulses. For example, in case of 10% duty cycle, the bubble average velocity can reach up to 0.1 m/s, which can compete with regular blood flows in medium and small-sized vessels.

The force is called the primary Bjerknes force after (46) when it is a resulting force of the incident acoustic wave. The force is called secondary Bjerknes force when it is a result of a nearby bubble driven by the same field. In this case the oscillating microbubble acts as a secondary ultrasound source, thus producing an additional pressure gradient term ∇P in the equation above. The acoustic radiation force can lead to a clustering effect: microbubbles that are within a distance of a few radii from each other tend to cluster because of an attractive secondary Bjerknes force. Bubble coalescence as well as bubble fission can occur within the cluster. This effect may result in larger bubble clusters, with a lower resonance frequency; yet, it is expected that this effect is low in case of forced flow or convection. Clustering effects have been observed in vitro in no-flow conditions and multiple transmission (order > 100 transmission / s), but the in-vivo concentration of microbubbles may be too low to have ‘a distance of a few radii’ between the bubbles on average.

2.2. EXPERIMENTAL METHODS

In early years, the microbubbles for medical applications were characterized by the acoustical scattering and attenuation properties of a population of bubbles [35]. Acoustic ensemble-averaged characterization is relatively inexpensive and has the advantage of a high sampling rate. However, it is very difficult to relate the ensemble-averaged behaviour to single microbubble dynamics, or even to a subset of microbubbles of similar size. Acoustic experiments on single microbubbles were also carried out [17][40][41][20] (see also Chapter 3), but the scattered pressure of a single bubble is limited (order 1 to 10 Pa) and close to the noise level of any acoustic detection system. To isolate single microbubbles, the concentration should be much smaller than one bubble per mm^3, which is dictated by the transducer focal region, and the size of the microbubble at hand should be measured independently. This has resulted in only few single microbubble acoustical studies, which however could confirm the optically observed relations between microbubble size and acoustic behaviour.

Advances in optical experimental technology gradually provided means for studying individual bubble dynamics. One method exploits laser-light scattering, which gives a relative value of the instantaneous 1-dimensional (1D) size. Other methods rely on ultra high-speed microscopy. A typical setup with a microscope includes an optically and acoustically transparent wall, to which microbubbles float up by buoyancy. In addition this allows for precise focusing of the optical equipment. The application demands that a camera should be able of temporally resolving the dynamics of the microbubbles driven at frequencies the order of a few MHz. The required frame rates make the construction of such a camera expensive, and the recording time is limited by the number of frames. In 1999, bubble dynamics were resolved in a 1D streak image using a microscope and camera setup. In addition, the camera used (Imacon 468) could also store seven 2D frames at high frame rate, facilitating the interpretation of the streak images. Higher frame numbers were available in the Ultranac system (twenty-four 2D frames), and in the Brandaris 128 camera system, which is able to record 128 frames at rates up to 25 million frames per second (Mfps).

Recently, the Brandaris-128 camera was extended with fluorescent imaging capability. Despite the relatively low fluorescent signal compared to bright field imaging, the system is capable of resolving molecular pathways by specific fluorescent binding. Chen et al. report on the development of a similar camera, but redesigned for higher fluorescence sensitivity, leading to higher frame rates for fluorescence

imaging. It is expected that ultrahigh speed fluorescent imaging will further improve the understanding of drug delivery dynamics.

From an acoustical standpoint, contrast agent microbubbles are essentially a delicate, nonlinear system. In order to perform the controlled experiments which are required to completely and correctly understand the dynamics of a few bubbles, usually specialized ultrasound research systems needs to be employed. Such systems typically provide not just high sensitivity to echo signals, which is an unavoidable requirement if single, isolated bubbles are to be investigated, but also fully programmable and customizable transmission patterns, a user-definable strategy to process the received echoes, and the possibility to store, access, and later analyze the raw RF echo signals. On top of that, the transmission and receive electronics must be very linear, to avoid masking or interfering in any way with nonlinear echoes originating from the microbubbles themselves. These featrures are typically not offered by commercial ultrasound scanners; only advanced ultrasound research systems, such as the Verasonics Vantage and the ULA-OP, comply with the desired requirements.

2.2.1. The ULtrasound Advanced Open Platform (ULA-OP)

The ULA-OP is a portable system integrated in a compact metal rack and connected to a PC where a dedicated software runs. The system's hardware configuration consists of a backplane board, a power supply board and two main boards: an analog board (AB) and a digital logic board (DB). The backplane hosts the probe connector and routes the power and the signals between the AB and the DB. The AB includes the RF front-end (transmitters, multiplexers and low-noise receivers) while the DB hosts the digital devices in charge of numerical beamforming and signal/image processing.

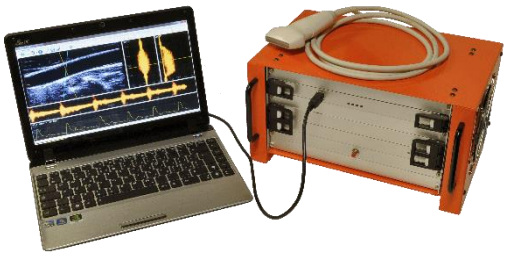

Figure 2:4 The ULA-OP system, connected to a laptop PC.

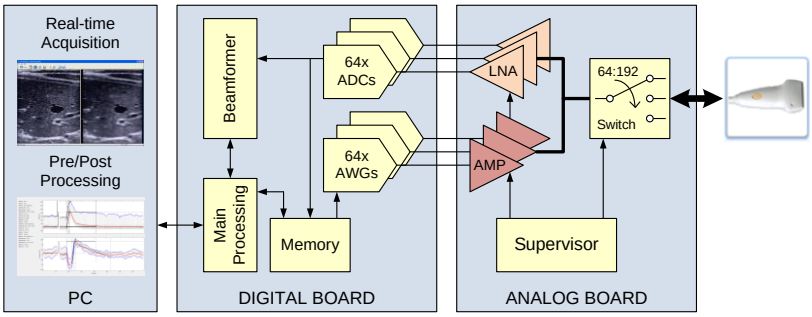

Figure 2:5 Functional diagram of the ULA-OP system, showing the different functions performed by the Digital and the Analog boards.

Figure 2:5 shows how the ULA-OP main functions are shared between the AB and the DB. The former includes the probe front-end with electronics for analog conditioning of the 64 channels. In each of the 64 available channels, the AB integrates a power amplifier, suitable to drive the probe element, and a Low Noise Amplifier (LNA), employed for conditioning the weak RX echoes. Moreover, the AB includes the programmable matrix switch necessary to dynamically map each channel to one of the 192 probe elements.

According to its nature of research platform, ULA-OP includes features and capabilities usually not found in commercial equipment. The transmission (TX) section is fully programmable, and it contains 64 independent arbitrary waveform generators (AWGs) capable of synthesizing an equal number of independent wideband TX signals. Each waveform is recovered by low-pass filtering a 600 Mb/s bitstream produced according to the Sigma-Delta technique; using this approach, the AWGs are capable of generating truly arbitrary waveforms in the 0.5 – 15 MHz frequency range. The 64 synthesized TX signals are transferred to the AB where they are amplified and routed, through a matrix switch, to the selected probe elements.

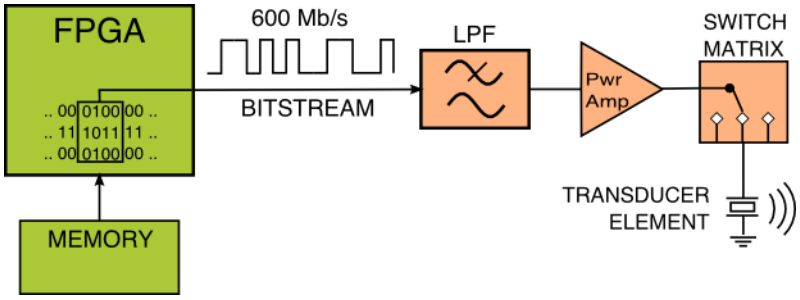

Figure 2:6 Block diagram of the TX structure of the ULA-OP for a single channel. Waveform samples are provided by the host PC and kept in local memory, as a Sigma-Delta Bitstream. The FPGA extracts the bitstream, demultiplexes the data pertaining to the desired channel, then streams the data to the analog part of the chain (Low Pass Filter, Power Amplifier, Matrix Switch and, finally, the single transducer element).

The receiving (RX) section conditions the echo-signals arriving to the active probe elements, in particular by means of low noise amplifiers (LNAs) followed by the so called time gain controlled (TGC) amplifiers, whose gain is programmable in the range 6-46 dB. Each amplified signal is sampled at 50 Msps by an Analog-to-Digital Converter (ADC) with 12-bit resolution, producing a 38.4Gb/s data flow which feeds the DB.

The four Front-End (FE) Field Programmable Gate Arrays (FPGAs) contained in the DB are in charge of operating the "dynamic receive beamforming" of the 64 echo-signals in real time. During RX, for each depth a specific phase delay is applied to each signal, to correct for the different paths they travel. A programmable weight can be applied to each delayed echo signal (Apodization) before all of them are summed together;. This beamforming algorithm, termed "delay-and-sum", effectively mimics the effect of an acoustical lens focusing at a specific depth; since the process is repeated for each depth, this virtual focus is dynamically moved across all the acquired depths.

This beamformed Radiofrequency (RF) signal can be sent to on an embedded digital signal processor (DSP) either directly or after passing coherent quadrature demodulation performed in real-time by the master FPGA (MF). The demodulated In Phase & Quadrature (I/Q) signal components are low-pass filtered through a chain of 4-stage cascaded integrator comb (CIC) filters interleaved with decimators.

The DSP processes the RF and/or demodulated I/Q data according to the desired operation mode (e.g. B-Mode, M-Mode, Power Modulation, etc., or custom-coded). Note that at the start of each pulse transmission event, both the TX and the RX sections can be fully reprogrammed.

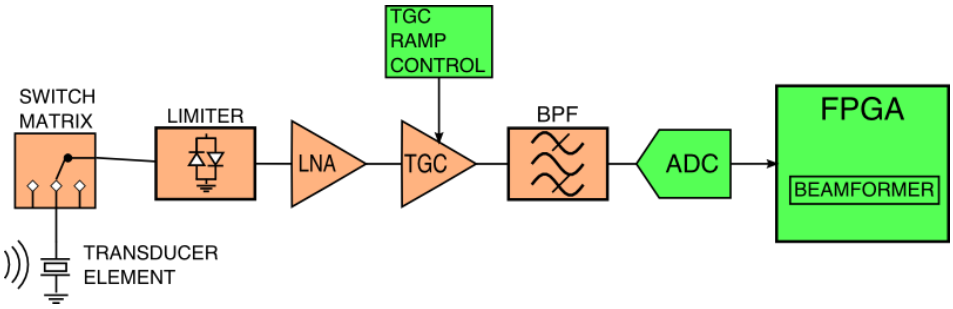

Figure 2:7 Block diagram of the ULA-OP RX structure for a single channel. The received electric signal is run through a Low-Noise preamplifier (LNA), then a variable gain amplifier effects the Time-Gain Compensation (TGC) programmed by the user; the echo waveform is then band-pass filtered, digitized and collected by the FPGA(s), where the beamforming operations are performed.

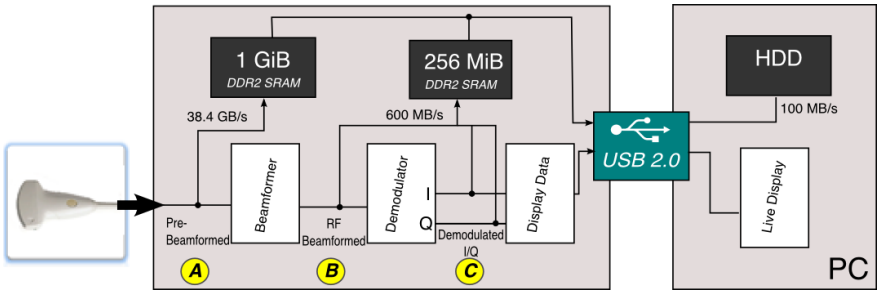

Figure 2:8 Memory configuration diagram, showing the ability to store echo data from multiple points of the RX chain.

ULA-OP includes 1.25 GiB of memory where data can be stored from any point of the RX chain, to be subsequently downloaded to a PC. 256 MiB are typically dedicated to the acquisition of either beamformed RF data or demodulated I/Q data. In both cases, for typical PRFs and investigation depths, such an amount of memory is sufficient to store several seconds of RX data. On the other hand, up to 1 GiB of internal DDR memory can be dedicated to the acquisition of pre-beamforming data. If, at PRF=10 kHz, 2048 12-bit samples are saved in each pulse repetition interval (PRI) from each active probe element, the total acquisition covers an interval of only 0.5 s.

For applications needing more memory (e.g. in plane wave imaging, when the raw RF echo data arriving to each element have to be stored), it is possible using an additional memory board, having 36 GiB storage capability. [42]

ULA-OP communicates through a USB 2.0 channel with a host PC, where a custom software runs. This software displays the results of real-time processing and presents a friendly user-interface suitable to control the system. Different panels show the operating parameters and the graphical output. Whenever a parameter changes, the software dispatches the variation to the DSP, which accordingly updates the appropriate memories, devices and processing modalities.

PROGRAMMING THE ULA-OP THROUGH THE CONFIGURATION FILE

The real-time software of ULA-OP, relies on several text files in order to setup the system and its parameters. Upon initialization, the software loads the probe file (*.wks), the configuration file (*.cfg) and one or more tx-rx strategy files (*.ula), and according to them, programs the hardware and prepares the graphical layout. These files describe not only how the system should work, but also which are the main features of the used probe, and which controls are available to the user. They also enable the user to define what to display in the windows of the application.

PROBE CONFIGURATION FILE

The Probe configuration file is a text file with "wks" extension containing extensive information about a specific ultrasound probe. This file is used by the ULA-OP software to identify the probe, so that the system can manage probes with different characteristics, provided that they comply with the ULA-OP specifications for probe compatibility. Data contained in the probe configuration file mainly concern the disposition of elements on the connector and the pitch of the probe array. They may also include an element sensitivity distribution, so that a gain equalization over the array is possible.

CONFIGURATION FILE

The configuration file is a text file with "cfg" extension; in it, most of the parameters contributing to the mode are defined, and the full path to other additional mode files is specified, where applicable. In particular, the configuration file defines: the windows layout in the main display of the real-time software, acquisition slices, real-time elaboration modules, and the list of employed Tx/Rx strategy files and how to manage them in consecutive PRIs.

TX/RX STRATEGY FILE

The Tx/Rx strategy file is a text file with "ula" extension that specifies the transmission and receive patterns contributing to a specific strategy. It defines: the number of beams/lines that the pattern comprises, the scanning type (e.g. linear or phasing), the transmission settings, the receive settings, and the demodulation. In particular, the transmission settings include: the active aperture size, the focal point coordinates, the steering angle, the apodization, the burst-length and the transmission amplitude. Similarly the reception settings include: the time gain compensation, the active aperture size, the dynamic focusing direction and the dynamic apodization shape.

▶ PROGRAMMING ULA-OP BY USING MATLAB

Whenever the flexibility of the text configuration files is not sufficient to setup the ULA-OP, the user can generate BF Tx (*.bft) and BF Rx (*.bfr) files. This is the case, for example, when 1.5D or 2D array probes have to be used or excitation waveforms different from the typical tone-bursts have to be transmitted. BF Tx and BF Rx files are binary files containing the data used by ULA-OP to set the TX/RX sequence. In particular, for each active element and for each transmission event, the user can define: the transmission waveforms, the spatial apodization and the focussing delays. Similarly, in reception, the user can define the dynamic beamforming law, in terms of both delays and apodization. These binary files have almost the same structure, divided into three parts: header, waveforms data bank, and element description.

Since BF Tx and BF Rx are binary files, they can be generated by any software. Anyway, ULA-OP is provided with a graphical user interface, called BFgenerator, to help the user generating the above mentioned files. BFgenerator is a Matlab application that guarantees the highest degree of freedom in terms of probes and tx/rx strategies. The user navigates through different interfaces to setup his own arbitrary mode in terms of probe, apertures, transmission strategies, receive dynamic beamforming, and scanning sequences. The interface extends the flexibility of the text configuration files of ULA-OP, e.g. it supports 2D arrays, it enables plane wave imaging, it generates chirp signals or contrast pulse sequences. Moreover, if the extended flexibility would not be enough, BFgenerator allows directly importing signals, delays and apodization from Matlab matrices, thus enabling more advanced modes. Once the user completely setup their own mode, BFgenerator checks if it complies with ULA-OP capabilities and generates the related BF Tx and BF Rx files.

UNDERSTANDING THE FLEXIBILITY OF THE ULA-OP DSP

The DSP is in charge of many tasks, mainly correlated to real-time acquisition and elaboration. It primarily acts as a supervisor, taking care of the overall system management. The ULA-OP software running on the PC converts the user defined configuration into multiple commands which are sent to the DSP through the USB channel; the DSP then interprets the commands to generate a sequence of operations according to the current scanning modality. While real-time acquisition is in progress, the DSP dispatches toward other devices a new set of parameters every PRI. In this way it continuously set up the analog matrix switch, the LNAs gain realizing the time-gain compensation, the transmission waveforms, the beamforming and the demodulation frequency (if any). This design paradigm translates to a high degree of freedom, as the transmission and receive chains can be independently reprogrammed on every PRI:

At the beginning of every PRI, the DSP copies a packet of fresh RF and/or I/Q demodulated samples from the MF into its external DDR memory. This external memory is partitioned into one or more buffers, called slices, that the DSP fills according to the SM commands. Each slice can, for example, be used as an independent data buffer feeding a different processing module running on the DSP. The data received from a single PRI can be used to fill multiple slices at the same time, if so desired. Therefore, when multiple processing modes are concurrently run on the DSP, if the same transmitted waveform is required by more than one mode it is possible to feed data to all the necessary slices using only one transmission, thereby removing the need to transmit redundant pulses and enabling a higher frame rate. The size of the slices is user programmable; since the slices are managed like circular buffers, they always contain the most recent samples of the current acquisition; once

the acquisition is stopped, the slices hold fresh data ready to be downloaded to the PC on user request.

The DSP firmware is structured to facilitate the insertion of multiple processing modules. During real-time system operation, one or more modules are concurrently run on the DSP, behaving like independent threads. Each module reads a new beamformed RF or IQ line from its assigned slice, then performs the necessary operations to reconstruct the ultrasound image. Several modules, and/or modules of the same type, can co-exist and work on the same or different slices. The reconstructed images are then streamed to the PC; when multiple modules are running, multiple independent live images can then be visualized on the screen, allowing to easily compare the different processing results. A module may also be programmed to extract parameters of interest, such as blood flow velocity in Doppler investigations, either in addition to, or in place of, reconstructing an US image. The DSP firmware features 16 concurrent processing modules, which embed computational intensive algorithms such as FIR and IIR filtering, logarithmic compression, spectral evaluation through Fast Fourier Transform (FFT), 2D cross correlation and bilateral filtering. The feasibility of combining modules together, provides the user with a broad range of suitable tools for testing new US methods. Additional specialized processing modules can be added to the system where necessary.

2.2.2. Verasonics Vantage 256 Research System

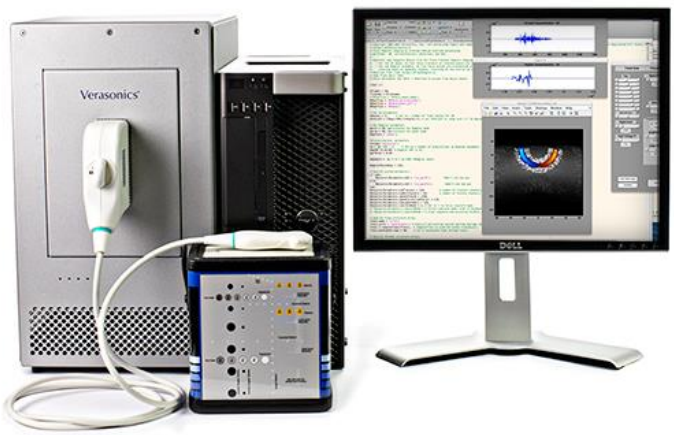

Figure 2:9 Verasonics Vantage System (source: Verasonics.com). This image shows a single-connector system, while the system used in this study had a double connector to facilitate 256 channels

The Verasonics Vantage 256 (Verasonics inc., Redmond, WA, USA) is a commercial programmable research ultrasound scanner built around the concept of providing maximum flexibility and programmability to the user by resorting to software processing of the RF data samples (before beamforming occurs).

The system contains 256 individual transmit/receive channels connected to two Cannon HDI-format ZIF connectors. The transmit part consists of bipolar pulse generators at a clock frequency of 250 MHz, with voltage limits of 3 Vpp on the lower side, and 190 Vpp at the higher side. The operating frequency range is 1 MHz to 15 MHz. Combined with fast image reconstruction algorithms and data processing on the host PC, a high data transfer rate enables real time imaging based on channel data. This is opposite to most regular ultrasound machines, in which the image reconstruction is performed on FPGAs in the front-end of the machine, which provides much lower flexibility in testing and applying new imaging algorithms.

The system is fully configurable by software running on the host PC, interfaced through a Matlab shell. This interface provides script-based programming of the machine, with many examples provided by the manufacturer. The script provides a list of events, in which events are subdivided into hardware configuration, data acquisition, image reconstruction, and further image processing (such as envelope detection, log-compression, and Doppler processing). The image reconstruction and further processing is performed on the multi-core CPU of the host PC, which runs in a loop that is a-synchronous to the hardware data-acquisition sequence loop. Yet, if needed, the data-acquisition sequence can be synchronized to the software reconstruction and display loop, if needed.

A crucial factor for the amplitude modulation as described in chapters 6 and 7 is the stability of the output signals. In amplitude modulation, a sequence of pulses with full and half amplitude are transmitted. The Verasonics machine contains bi-polar pulse generators which do not allow simple half-amplitude transmission. Therefore, the half amplitude transmission was achieved by transmitting on every other element only. Yet, because of the different load on the internal power supply for the transmit channels, such difference in load could induce an additional nonlinearity to the signals. For example, on an Ultrasonix machine (SonixTOUCH, Ultrasonix medical corporation, Richmond BC, Canada), the full-amplitude pulses had about 25 ns delay compared to the half ampltitude pulses. On the Verasonics machine, this delay was 2.5 ns. Since any additional time delay in the transmitted pulses reduce the linear echo cancellation (which in turn reduces contrast-to-tissue ratio), this stability yielded an important argument to use the Verasonics machine instead of the Ultrasonix machine.

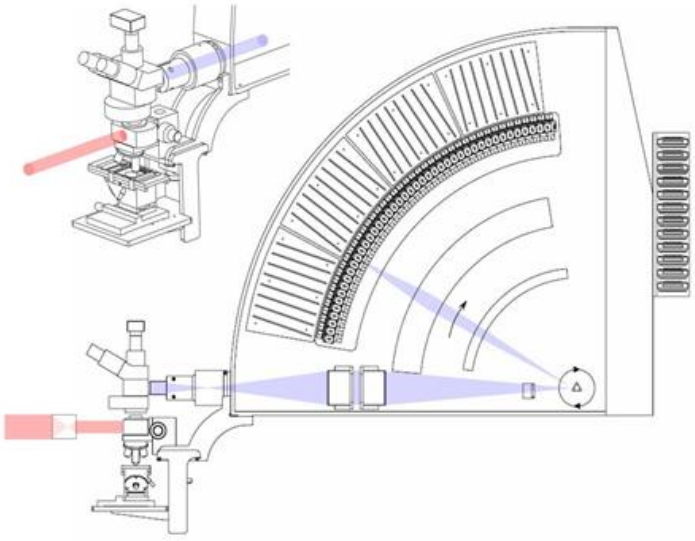

Figure 2:10 The Brandaris 128 Ultrafast framing camera

2.2.3. BRANDARIS 128 Ultrafast Framing Camera

Optical verification of the bubble behavior is a wonderful tool to directly assess the bubble size, conditions, isolation and, more in general, its reactions to ultrasound insonation. Information obtained in this way is invaluable to test and verify specific hypothesis, and is especially useful when working with a very low concentration of (or even single) microbubbles.

Contrast agent microbubbles have a radius typically in the 1-10 um range, and oscillate in response to an ultrasound imaging pulse; typically a sinusoid in the 2-10 MHz range is used to transmit a burst a few microseconds long. To capture the full bubble oscillation, a camera must thus possess a big enough memory buffer to store a number of frames sufficient to capture the entirety of the oscillation phenomena. Furthermore, it must be capable of capturing the 2D images at a rate of several million frames per second.

The BRANDARIS 128 camera (Erasmus MC, Rotterdam, The Netherlands) is a fully digital camera that was designed to provide a high speed framing using a rotating mirror. The working principle of the rotating mirror camera is based on the Miller principle for high-speed cinematograph.

The system employs a rotating three-faced mirror prism deflecting the incoming light to 128 high sensitivity CCD chips arranged in a quarter arc (see Figure 2:10). A set

of relay lenses relays the image from the primary image plane of the camera to the secondary image plane, located at the mirror surface. Because of the limited pitch available in the framing camera, the CCDs are mounted in groups of three where for each group two channels are deflected either upward or downward by small surface mirrors. The image recorded on each CCD is transferred to a specialized CCD control board (C3). The C3 drives the CCD electronics, reads out and digitizes the raw CCD signals, stores the images in RAM memory and handles the data transfer to the PC. A single C3 controls four CCD's; thus a total of 32 C3s are housed inside the system frame. CCDs are multiplexed through a set of USB hubs, to reduce the number of required USB connections and allow the whole system to be connected to and controlled by a single PC or laptop. In front of the camera a microscope is mounted with an optical magnification between 20 to 240 times.

A specialized turbine driven by high-pressure helium or air spins the prism at a maximum rotation speed of 20 000 revolutions per second (rps). The gas flow is controlled by a mass flow controller (MFC), which in turn is controlled by a PC. A small infrared laser-photodiode pair mounted near the mirror prism generates three mirror pulses per turbine revolution. Since a rotating mirror camera cannot be triggered externally, the mirror pulses are used as master timing triggers for the target event and light source. Additionally, a total of 8 trigger signals and 2 analog signals are derived from this master timing pulse and routed externally to synchronize additional equipment, if needed. The rotation speed of the mirror determines the framing rate of the recording; the flow system can maintain a preset frame rate by adjusting the mass flow according to the measured frequency of the mirror pulses.

A commercially available CCD was chosen for its combination of price, availability, resolution and light sensitivity,. This inter-line video chip produces 500x292 pixels with an approximate dynamic range of 48 dB, and was rated with a sensitivity of 0.03 lux.

The C3 architecture controls each CCD individually, allowing for operation in the normal mode capturing 128 images in a sequence or in a segmented mode in which multiple sequences can be captured at very high repetition rate. In normal mode, a repetition time as short as 16.7 μs is possible when the turbine is ran at maximum speed, corresponding to a framerate of 25 Mfps. Even shorter repetition times are achievable by dividing the 128 CCDs into different subgroups when the camera is run in segmented mode. The on-board RAM buffer allows six images per detector to be stored before RAM dump; for example, six experiments totaling 768 image frames can be acquired within a fraction of a second. This makes it convenient to run multiple recordings in a short time frame, preventing undesired effects such as bubble aging

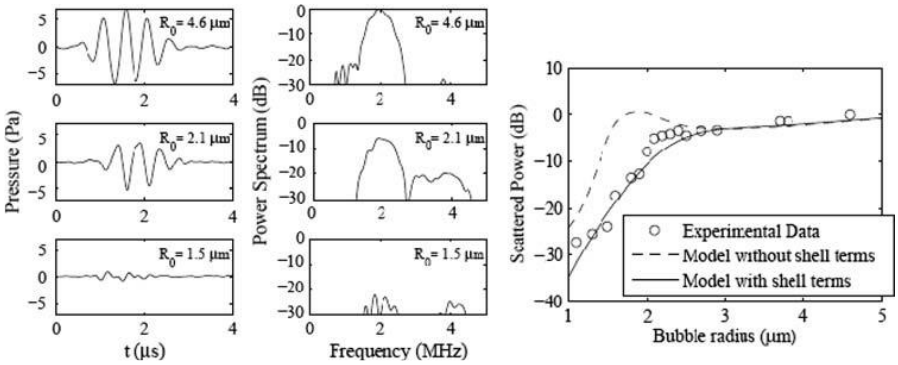

Figure 2:11 Measured responses of three single bubbles of three different sizes (4.6, 2.1 and 1.5 µm) excited with a driving pressure of 100 kPa. Left panel Measured pressure in Pa. Right Panel frequency response (reproduced with permission of JASA 2008)

or motion from affecting the outcome of the measurement and allowing for a better use of both the helium source and the turbine's limited lifetime.

2.3. SINGLE BUBBLE STUDIES

As reported in [21], a suspension of the phospholipid-coated experimental contrast agent BR14 (Bracco Research, Geneva, Switzerland) was diluted by a ratio of 1:10,000, which corresponds to 25,000 bubbles per ml. This high dilution rate resulted in an average of one single bubble in the effective insonified volume of 0.04 µl within the capillary tube (diameter: 200 µm). This corresponds to a statistically averaged distance of 1.5 mm between two adjacent bubbles. In addition, the capillary tube was optically scanned to ensure that there was only one bubble in the acoustic focal area. To ensure that all of the bubbles present in the capillary tube were optically observable, smaller bubbles were excluded from the suspension by decantation. As a result, 80% of the bubbles in the suspension had a radius larger than 2 µm, which was verified using a Multisizer 3 counter (Beckman-Coulter, Miami, FL).

The left panel of Figure 2:11 shows typical examples of single bubble echoes measured at an acoustic pressure of 100 kPa. The time traces for bubbles with sizes of R0 = 4.6 µm, 2.1 µm, and 1.5 µm and the corresponding power spectra are displayed. The receiver was calibrated so that the results are absolute pressures [Pa]. It is observed that the acoustic response of the smallest bubble is 25 dB lower than the maximum response, measured for the largest bubble. This bubble with a resting radius of 1.5 µm is excited below its resonant frequency and hence behaves as a Rayleigh scatterer. The bubble with a radius of R0 = 2.1 µm (middle panel) is excited close to its

resonant frequency. The presence of a substantial second harmonic component in its frequency response confirms this observation.

The right panel of Figure 2:11 shows more measured scattered powers for bubbles with radii between 1 and 5 µm. The experimental results (circles) were compared with simulated bubble responses for free gas bubbles (dashed curve) and phospholipid-coated bubbles using the Marmottant model (solid curve). The experimental results nicely fit the simulated results using the Marmottant model, which shows the influence of the phospholipid coating when the bubbles are insonified below resonance. Above resonance the coated bubbles act like free gas bubbles [21].

2.3.1. Optical characterization

We can listen to the sound that the bubbles produce, but it is at least as much interesting to see the origin of these sounds, which is the bubble vibration. Watching bubbles has several advantages over listening. First of all, the wavelength of light is much shorter than that of ultrasound. While ultrasound typically has a wavelength of 500 µm, light has a typical wavelength of only 0.5 µm. As a consequence, although it is possible to measure individual bubbles acoustically, optical measurements are easier. In a general acoustical experiment, even with a high dilution, there are still hundreds of bubbles per wavelength. With light, you can easily observe individual bubbles since the size of the bubbles is larger than the wavelength of light.

An optical measurement system to observe bubble vibration is shown in Figure 2:10. It consists of a water tank containing the bubbles, a microscope and fast framing camera. The bubbles are magnified to a size that can be detected by the camera. In our system, the microscope magnifies by a factor of 240. Subsequently, one must have a camera that is able to record images at an extremely high frame rate. An average video camera does not suffice because it records at most 25 images per second, while the bubbles vibrate at a frequencies in the order of few MHz. Experience has shown that in order to evaluate periodic phenomena accurately, the sampling rate should exceed the frequency of the phenomenon by at least a factor 8-10. We therefore developed a fast framing camera system, which is able to record at a frame rate of 25 million frames per second. The camera system is based on a fast rotating mirror (max. 20,000 rps), which sweeps images of the bubbles along 128 charge coupled devices (CCD's). In one experiment, the camera system records six movies of 128 frames with an interval time of 80 ms between the movies. The camera system was called "Brandaris 128" after a famous lighthouse in the Netherlands [23].

Figure 2:12 presents an example of a recording with the Brandaris fast framing

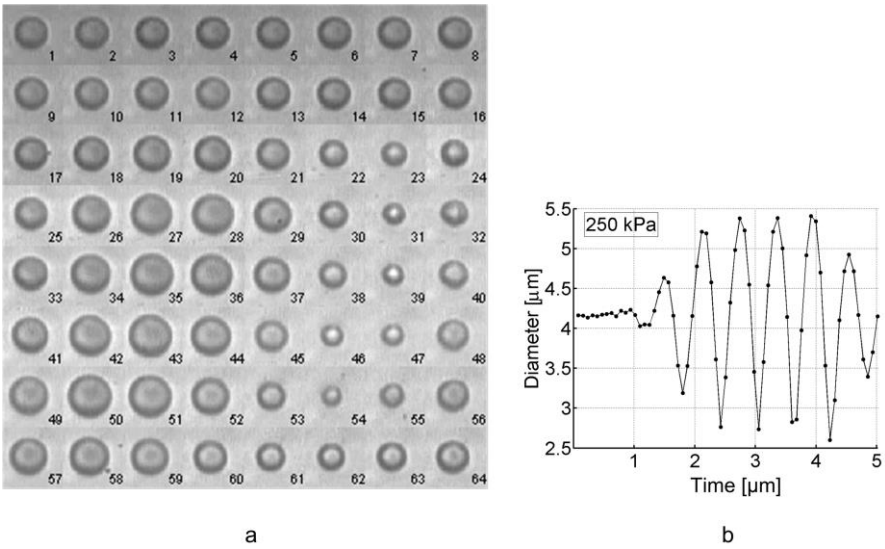

Figure 2:12 a Sequence of 64 image frames of a 4.2 lm diameter microbubble, driven by a 6-cycle US burst with a peak negative pressure of 250 kPa. b Diameter–time response.

camera. The figure shows an isolated bubble with a size of 4.2 µm in diameter that was insonified with an acoustic pressure of 250 kPa at a frequency of 1.7 MHz. In 64 frames we observe the bubble before, during and after the ultrasound pulse. In the first 13 frames, the microbubble is at rest. Starting at frame 14, the microbubble is first compressed, and then reaches within six cycles a maximum diameter of 5.4 µm and a minimum diameter of 2.6 µm. We can establish in each image frame the bubble diameter. The resulting diameter-time (D-T) curve is shown in the panel in the middle and the corresponding power spectrum in the right panel. The advantage of an optical recording is that we can compare this D-T curve with the outcome of a simulation directly. In order to compare simulations with the outcome of an acoustical experiment, we first have to translate the simulated radial responses into scattered pressures.

With the fast framing camera several interesting studies on individual bubbles can be performed. An example is the determination of the bubble's resonant frequency [16]. This was achieved by repeatedly insonifying the bubbles, whereby the transmit frequency is varied over the different recordings. Because the Brandaris is able to record six movies of 128 frames, or 12 movies of 64 frames etc., such an experiment was done within one run in 2 s. From the recorded images a resonance curve are constructed showing the resonance peak and width.

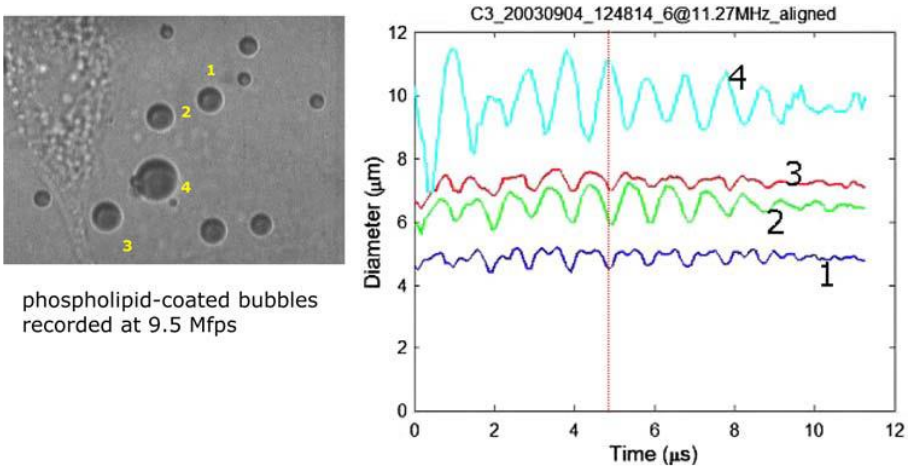

Figure 2:13 Bubbles images at 1 MHz and 200 kPa with the Brandaris fast framing camera. Right panel the corresponding D–T curves

Figure 2:13 shows another example of the strength of optical measurements. The left panel displays an image frame containing several bubbles that are quite close together (< 20 µm). The bubbles have been insonified with an ultrasound pulse of 1 MHz and 200 kPa. The ultrasound field has a wavelength of 1.5 mm, which is much larger than the size of the bubbles. The bubbles therefore all experience the same ultrasound field. This however did not result in identical responses for all bubbles. This is most clear when we compare the bubble with a size of 6 µm in diameter (No 2) with the bubble with the largest size of 10 µm in diameter (No 4). At t = 5 µs, we observe a 180° phase difference between both bubble responses. Such behavior is typical for harmonic oscillators. When the oscillator is insonified below resonance, it responds in phase with the driving force. Above resonance, inertia dominates and the response will be out of phase with the driving force. A bubble that is insonified at its resonant frequency will respond with a 90° phase difference compared to the phase of the driving force. Based on our observations we conclude that the resonant size for a transmit frequency of 1 MHz must be between 6 and 10 µm in diameter.

2.3.2. Experimental limitations

It should be noted that many in vitro optical experiments are performed with microbubbles nearby a relatively stiff membrane, enough for acoustic interaction [45]. The stiff membrane will lead to microbubble nonspherical shape deformation, eventually leading to a jet pointing towards the wall [44]. Such deformations become present at relative radial excursions of about 20% and higher [44].

A wall can also influence the radial oscillation dynamics of microbubbles, see e.g. [44] for direct experimental proof. In literature several extensions to the bubble

dynamics equations have been made to account for a vessel wall near an oscillating microbubble. Doinikov and coworkers have theoretically studied the influence of a solid wall, a fluid interface, and a fluid thin layer near an oscillating microbubble although experimental data lacks clear validation of the theoretical predictions near a fluid layer or half-sphere.

One rudimentary and traditional method to model the influence of the wall is called the method of images (see, e.g., [17]). In this method, the rigid wall is replaced by an identical image bubble oscillating in-phase with the real bubble and positioned at a mirrored image point. The bubble is assumed to remain spherical, and slip can occur at the boundary. As a result, both the resonance frequency and the damping are found to decrease by order 20% compared to the bubble in free space [37]. Experiments showed 30% of resonance frequency decrease, indicating that the method of images produces reasonable results despite its rudimentary approach. Moreover, it has been shown experimentally that adherence of functionalized microbubbles to a wall significantly decreases the oscillation amplitude.

Various studies have addressed the confinement caused by capillaries and arterioles. The confinement leads to significant oscillation amplitude reduction, as verified in vivo in a chicken embryo model and ex-vivo in the ilecolic vein of a rat. In some cases, the authors suggest that the increased viscosity of blood, compared to water, resulted in this reduction of amplitude. Nevertheless retrospectively, the confinement effect may equally have played a role. Moreover, it has been often shown that non-spherical oscillations occur frequently in vessels, which strengthens the hypothesis for confinement effects.

Most in vitro experiments for studying the behaviour of microbubbles are performed at room temperature. However, temperature plays an important role in the rheological behaviour of phospholipids and, consequently, in the behaviour of phospholipid-coated microbubbles. Therefore, great care should be taken when translating microbubble behaviour at room temperature in vitro directly to results from in vivo applications. Occasionally, in vitro drug delivery experiments with living cells demand a temperature-regulated environment, thus intrinsically matching the temperature of the experiment to in vivo application.

REFERENCES:

[1] Gramiak, R. and P.M. Shah *"Echocardiography of the aortic root."* Investigative radiology 3.5 (1968): 356-366.

[2] van Liew, H.D. and M.E. Burkard, *Behavior of bubbles of slowly permeating gas used for ultrasonic imaging contrast.* Invest Radiol, 1995. **30**(5): p. 315-21.

[3] Epstein, P.S. and M.S. Plesset, *On the stability of gas bubbles in liquid-gas solutions.* The Journal of Chemical Physics, 1950. **18**(11): p. 1505-1509.

[4] Kabalnov, A., et al., *Dissolution of multicomponent microbubbles in the bloodstream: 1. Theory.* Ultrasound Med Biol, 1998. **24**(5): p. 739-49.

[5] Medwin, H., *Counting bubbles acoustically: A review.* Ultrasonics, 1977: p. 7-13.

[6] de Jong, N., A. Bouakaz, and P. Frinking, *Basic acoustic properties of microbubbles.* Echocardiography, 2002. **19**(3): p. 229-40.

[7] Brenner, M.P., S. Hilgenfeldt, and D. Lohse, *Single-bubble sonoluminescence.* Rev. Mod. Phys., 2002. **74**: p. 425-484.

[8] de Jong, N., et al., *Absorption and scatter of encapsulated gas filled microspheres: Theoretical considerations and some measurements.* Ultrasonics, 1992. **30**(2): p. 95-103.

[9] de Jong, N. and L. Hoff, *Ultrasound scattering properties of Albunex microspheres.* Ultrasonics, 1993. **31**(3): p. 175-181.

[10] Church, C.C., *The effect of an elastic solid surface layer on the radial pulsations of gas bubbles.* J Acoust Soc Am, 1995. **97**(3): p. 1510 - 1521.

[11] Allen, J.S. and M.M. Rashid, *Dynamics of a hyperelastic gas-filled spherical shell in a viscous fluid.* J Appl Mech, 2004. **71**: p. 195-200.

[12] Hoff, L., P. Sontum, and J. Hovem, *Oscillations of polymeric microbubbles: Effect of the encapsulating shell.* J Acoust Soc Am, 2000. **107**(4): p. 2272-2280.

[13] Morgan, K.E., et al., *Experimental and theoretical evaluation of microbubble behavior: effect of transmitted phase and bubble size.* IEEE Trans Ultrason Ferroelectr Freq Control, 2000. **47**(6): p. 1494-1509.

[14] Sarkar, K., et al., *Characterization of ultrasound contrast microbubbles using in vitro experiments and viscous and viscoelastic interface models for encapsulation.* J Acoust Soc Am, 2005. **118**(1): p. 539-50.

[15] Marmottant, P., et al., *A model for large amplitude oscillations of coated bubbles accountin g for buckling and rupture.* J Acoust Soc Am, 2005. **118**: p. 3499-3505.

[16] de Jong, N., R. Cornet, and C.T. Lancee, *Higher harmonics of vibrating gas filled microspheres. Part two: Measurements.* Ultrasonics, 1994. **32**: p. 455-459.

[17] J. Sijl, H. J. Vos, T. Rozendal, N. de Jong, D. Lohse, and M. Versluis, "Combined optical and acoustical detection of single microbubble dynamics," *The Journal of the Acoustical Society of America*, vol. 130, no. 5, pp. 3271–3281, Nov. 2011.

[18] van der Meer, S.M., et al., *Microbubble spectroscopy of ultrasound contrast agents.* J Acoust Soc Am, 2007. **121**(1): p. 648-56.

[19] Apfel, R.E., and Christy K. Holland. "*Gauging the likelihood of cavitation from short-pulse, low-duty cycle diagnostic ultrasound.*" Ultrasound in medicine & biology 17.2 (1991): 179-185.

[20] Emmer, M., et al., *Pressure-dependent attenuation and scattering of phospholipid-coated microbubbles at low acoustic pressures.* Ultrasound Med Biol, 2009. **35**(1): p. 102-111.

[21] Lotsberg, O., J.M. Hovem, and B. Aksum, *Experimental observation of subharmonic oscillations in Infoson bubbles.* 1996, ASA. p. 1366-1369.

[22] Frinking, P., E. Gaud, and M. Arditi, *Compression-only behavior and subharmonic scattering of phospholipid-shell microbubbles.* Abstr. 14th Eur Symp Ultrasound Contrast Imaging, 2009: p. 80-87.

[23] Shi, W.T., et al., *Image enhancement by acoustic conditioning of ultrasound contrast agents.* Ultrasound Med Biol, 2004. **30**(2): p. 191-8.

[24] Sijl, J., et al., *Acoustic characterization of single ultrasound contrast agent microbubbles.* J Acoust Soc Am, 2008. **124**(6): p. 4091-4097.

[25] Chin, C.T., et al., *Brandaris 128: a 25 million frames per second digital camera with 128 highly sensitive frames.* Rev. Sci. Instru., 2003. **74**(12): p. 5026-5034.

[26] Wei, K., et al., *Quantification of myocardial blood flow with ultrasound-induced destruction of microbubbles administered as a constant venous infusion.* Circulation, 1998. **97**(5): p. 473-483.

[27] Dijkmans, P.A., et al., *Microbubbles and ultrasound: from diagnosis to therapy.* Eur J Echocardiogr, 2004. **5**(4): p. 245-56.

[28] Unger, E.C., et al., *Therapeutic applications of lipid-coated microbubbles.* Adv Drug Deliv Rev,

2004. **56**(9): p. 1291-314.
[29] Bouakaz, A., et al., *Noninvasive measurement of the hydrostatic pressure in a fluid-filled cavity based on the disappearance time of micrometer-sized free gas bubbles.* Ultrasound Medicine Biology, 1999. **25**(9): p. 1407-1415.
[30] Bouakaz, A., M. Versluis, and N. de Jong, *High-speed optical observations of contrast agent destruction.* Ultrasound Med Biol, 2005. **31**(3): p. 391-399.
[31] Frinking, P.J.A., et al., *Ultrasound contrast imaging: current and new potential methods.* Ultrasound Medicine Biology, 2000. **26**(6): p. 965-975.
[32] de Jong, N., et al., *"Compression-only" behavior of phospholipid-coated contrast bubbles.* Ultrasound Med Biol, 2007. **33**(4): p. 653-6.
[33] Burns, P.N., T. Wilson, and H.S. D., *Pulse inversion imaging of liver blood flow: An improved methode for characterization of focal masses with microbubble contrast.* Invest. Radiol., 2000. **35**(1): p. 58-71.
[34] Emmer, M., et al., *The onset of microbubble vibration.* Ultrasound Med Biol, 2007. **33**(6): p. 941-9.
[35] Tang, M.-X., R.J. Eckersley, and J.A. Noble, *Pressure-dependent attenuation with microbubbles at low mechanical index.* Ultrasound Med Biol, 2005. **31**(3): p. 377-384.
[36] Emmer, M., et al., *Clinical relevance of pressure-dependent scattering at low acoustic pressures.* Ultrasonics, 2007. **47**(1-4): p. 74-77.
[37] Overvelde, M., et al., *Nonlinear shell dynamics near the resonance frequency of ultrasound contrast agents.* IEEE Ultrasonics Symposium, 2008.
[38] Vos, H.J., et al., *Nonspherical vibrations of microbubbles in contact with a wall - a pilot study at low mechanical index.* Ultrasound Med Biol, 2008. **34**(4): p. 685-688.
[39] Garbin, V., et al., *Changes in microbubble dynamics near a boundary revealed by combined optical micromanipulation and high-speed imaging.* Applied Physics Letters, 2007. **90**(11): p. 114103-3.
[40] J. Sijl, E. Gaud, P. J. A. Frinking, M. Arditi, N. de Jong, D. Lohse, and M. Versluis, "Acoustic characterization of single ultrasound contrast agent microbubbles," *The Journal of the Acoustical Society of America*, vol. 124, no. 6, pp. 4091–4097, Dec. 2008.
[41] F. Guidi, H. J. Vos, R. Mori, N. de Jong, and P. Tortoli, "*Microbubble characterization through acoustically induced deflation,*" *I*EEE Transactions on Ultrasonics, Ferroelectrics, and Frequency Control, vol. 57, no. 1, pp. 193–202, Jan. 2010.
[42] E. Boni, A. Cellai, A. Ramalli, and P. Tortoli, "*A high performance board for acquisition of 64-channel ultrasound RF data,*" in Ultrasonics Symposium (IUS), 2012 IEEE International, 2012, pp. 2067–2070.
[43] P. Tortoli, M. Pratesi, and V. Michelassi, "Doppler spectra from contrast agents crossing an ultrasound field," *IEEE Transactions on Ultrasonics, Ferroelectrics, and Frequency Control*, vol. 47, no. 3, pp. 716–726, May 2000.
[44] H. J. Vos, B. Dollet, M. Versluis, and N. de Jong, "*Nonspherical Shape Oscillations of Coated Microbubbles in Contact With a Wall,*" Ultrasound in Medicine & Biology, vol. 37, no. 6, pp. 935–948, Jun. 2011.
[45] Brujan, E. A., Nahen, K., Schmidt, P., and Vogel, A. "Dynamics of laser-induced cavitation bubbles near an elastic boundary". *Journal of Fluid Mechanics*, 2001, *433*, pp. 251-281.

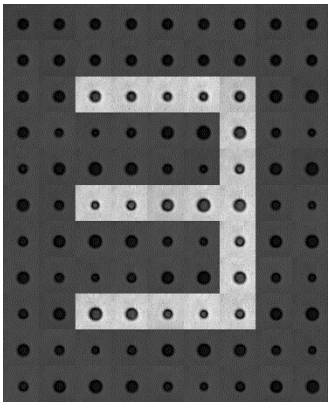

3. Nonlinear oscillations of deflating bubbles

Abstract **- Phospholipid-coated ultrasound contrast agents may deflate or even collapse because of stress resulting from ultrasound-induced oscillations. In this work we investigate the behavior of isolated contrast agent microbubbles during prolonged ultrasound excitation. Isolated microbubbles placed in a thin capillary tube were excited with hundreds of ultrasound pulses at a low mechanical index, and their oscillations were recorded using the Brandaris-128 ultra high-speed camera. Results show that microbubbles undergo an irreversible, non-destructive deflation process. Such deflation seems to occur in discrete steps rather than as a continuous process; furthermore, the dynamics of the bubble changes during deflation: radial oscillations, both symmetric and asymmetric around the resting radius of the bubble, occur at various stages of the deflation process. Strongly asymmetric oscillations, such as compression-only and expansion-only behavior, were also observed: notably, expansion-only behavior is associated with a rapid size reduction, whereas compression-only behavior mostly occurs without a noticeable change of the bubble radius. We hypothesize that bubble deflation results from at least two distinct phenomena, namely diffusive gas loss and lipid material shedding from the encapsulating shell.**

Appeared as a correspondence paper on *IEEE Transactions on Ultrasonics, Ferroelectrics and Frequency Control*, vol. 59, no. 12, 2012, by J. Viti, R. Mori, F. Guidi, M. Versluis, N. de Jong, and P. Tortoli.

3.1. INTRODUCTION

Ultrasound contrast agents (UCAs) are made of a suspension of micrometer-sized gas bubbles, which are coated by a thin flexible shell. The microbubbles oscillate when hit by an ultrasound (US) pressure pulse, thereby generating an echo that can be detected in the far-field. In medical US imaging, UCAs are used to increase the contrast between the echoes backscattered from the blood pool and those backscattered from tissue [1-4].

The optimal strategy for contrast detection should take into account both the specific application scenario and the UCA physical characteristics; for example, when imaging regions with a very low blood velocity, such as in the capillary bed of organs, microbubbles might be exposed to several hundreds of US pulses. Such prolonged excitation is expected to drive the microbubbles toward dissolution [5][6]. Dissolution of the bubbles may result from different physical phenomena. In phospholipid-coated bubbles it occurs mostly as direct gas loss from the bubble through the release of smaller bubbles [7], or through gas diffusion from the bubble core into the surrounding fluid [8][9]. The former process is a fast phenomenon, often occurring after violent oscillations, whereas the latter process is relatively slow, as it is driven by capillary pressure and gas concentration. Since these dissolution phenomena are expected to alter the bubble response in a significant way, accurate characterization of UCAs should also aim at tracking bubble transformations in time during multiple exposures to ultrasound, as changes in the bubble response may alter the performance of the imaging strategy.

In this work we investigated experimentally how single phospholipid-coated microbubbles respond to prolonged US excitation. A custom setup was built to position a single, isolated bubble in the optical focus of an immersion microscope and in the acoustical focus of an US transducer. The latter repeatedly excited the bubble with low-pressure pulses, to stress the bubble while avoiding its rapid destruction. Bubble oscillations were recorded at different stages of the deflation process using ultrafast optical imaging. This approach offered insight into the physical process leading to deflation, and two different phenomena are highlighted from the recorded dynamics.

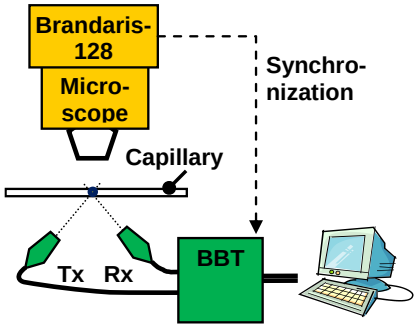

Figure 3:1 Schematic drawing of the setup. The Brandaris camera acts as master, triggering the BBT system to start US transmission and recording. Although the RX capability is not exploited in this work, this setup is suitable for acoustical recordings of single bubbles using separate TX and RX transducers.

3.2. MATERIALS AND METHODS

SETUP

A schematic representation of the setup is shown in Figure 3:1. The Brandaris-128 camera [10] was connected to an immersion microscope focused on a thin cellulose capillary (outer diameter 200 μm; wall thickness 20 μm) stretched across a cylindrical water tank. Flow inside the capillary was controlled manually using a syringe connected to a fine-pitch micrometer screw. Definity® (Lantheus Medical Imaging, N. Billerica, MA) contrast agent bubbles were used. The bubble oscillations were recorded near 13 million frames per second, with an optical 70× magnification factor, yielding a final image resolution of 0.135 μm per pixel. US pulses were transmitted by a wideband transducer (PA076 PVDF, Precision Acoustics, Dorchester, UK) driven by the Bubble Behavior Testing (BBT) board, a two-channel custom programmable ultrasound system developed in-house [11].

EXPERIMENTS

A highly diluted suspension of Definity® was injected in the capillary, then flushed until a single, isolated bubble was in the optical focus of the microscope objective, which was co-aligned with the acoustical focus of the US transducer. At the end of each experiment, the capillary was thoroughly flushed, to replace all the bubbles contained within the capillary with fresh ones.

The high-speed imaging equipment poses some limitations in terms of timing. The Brandaris camera refresh time, i.e. the minimum time interval between two consecutive movie recordings is 100 ms. Moreover, the movies are stored into an internal memory, which can hold a maximum of 6 movies, each 128 frames long. Downloading the 6 movies to a pc and cooling down the camera turbine takes about

2 minutes; during this interval the camera cannot be operated. During the resting intervals US was always off to avoid US exposure to the bubble; the absence of flow within the capillary limited the motion of the bubble to random Brownian motion and consequently the bubble was always kept in position. Then, as soon as the camera was ready for operation, the experiment was resumed using the very same bubble; this routine effectively overcomes the Brandaris memory limitations, and made it possible to monitor the time-resolved dynamics of a single, isolated bubble over hundreds of US pulses.

Two different excitation schemes were used for the experimental sessions: single frequency and step frequency modulation (step-FM). In the single frequency experiments, 2 MHz, 15-cycles long tone bursts were transmitted, each yielding 60 kPa peak-negative pressure in the focus of the transducer. The pulse repetition interval (PRI) was set to 20 ms: considering the Brandaris camera refresh time of 100 ms, this PRI yields one recording of the bubble oscillations every 5-th transmitted pulse. In step-FM experiments, tone bursts were transmitted sequentially at 2.0 MHz, 2.5 MHz, 3.0 MHz, 3.5 MHz and 4.0 MHz; the sequence then repeats continuously. The pulse length and pressure in the focus of the transducer were the same as in the single frequency experiments. The PRI was set to 4 ms so that five complete sequences (25 pulses) were transmitted between two consecutive Brandaris recordings.

OSCILLATION ANALYSIS

In each experiment, both symmetrical and asymmetrical oscillations were observed. Asymmetrical oscillations, in which the amplitude of expansion and compression phases are not equal, included the two extreme cases where the expansion phase ("compression-only") and the compression phase ("expansion-only"), respectively, have nearly zero amplitude.

To allow a quantitative description and comparison of the different observed radial oscillations, we use an approximated analysis of the bubble dynamics, following Sijl *et al.* [12]. The radius oscillation is expressed as a perturbation, x, of the resting radius, R_0:

$$R(t) = R_0(1 + x(t)) \tag{3.1}$$

and we assume that, for a bubble oscillating in a steady state, the radial perturbation is of the form

$$x(t) = A_0(t) + A_1 \sin(\omega t + \phi_1) \tag{3.2}$$

In this equation, A_0 describes the offset of the radius-time curve and A_1 expresses the amplitude of the oscillation at the driving frequency The maximum of the offset, A_0, normalized to the oscillation amplitude A_1, expresses the nonlinear characteristics of the radius oscillation. The contributions of subharmonics and higher harmonics are neglected in this analysis, as we simply look for an unbiased measure of the asymmetric oscillation: a positive A_0/A_1 ratio indicates that amplitude of the expansion phase is greater than the amplitude of the compression phase; conversely, a negative ratio expresses an oscillation dominated by a compression phase. Higher absolute values of A_0/A_1 indicate a greater asymmetry in the radius-time curve, with 1, -1 and 0 indicating perfect expansion-only behavior, perfect compression-only behavior and perfectly symmetrical oscillation, respectively.

In Figure 3:2, two experimental examples of strongly asymmetrical oscillations are presented; the left panel shows an example of compression-only behavior (negative A_0/A_1) and the right panel corresponds to an expansion-only behavior (positive A_0/A_1). A 3rd order Chebychev low-pass filter with 150 kHz cut-off is applied to extract the offset curve (red line) from which A_0 is determined. Similarly, a Chebychev 1.2 MHz-wide bandpass filter, centered on the transmitted frequency, is used to get the linear oscillation with amplitude A_1. Residual contribution from undesired harmonics prevents both examples from achieving a perfect -1 and 1 A_0/A_1 ratio, respectively.

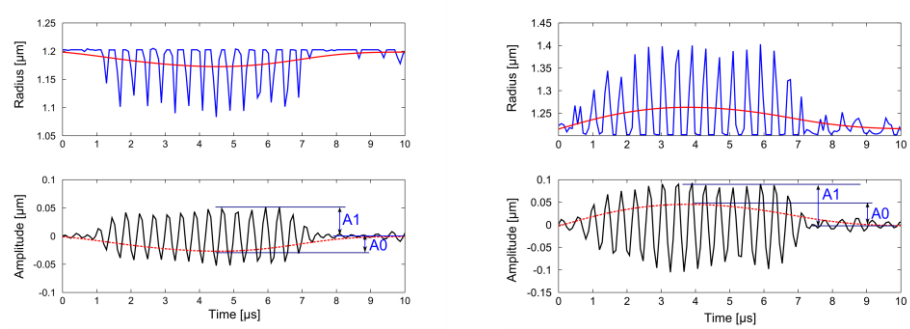

Figure 3:2 Examples of compression-only behavior and expansion-only behavior of an isolated bubble excited with a 2.5MHz pulse. A (left), top: radius-time curve of bubble displaying compression-only behavior; the solid red line shows the radius mean value during the oscillation. A (left), bottom: A1: first-order term of the compression-only time curve (solid black) and A0: deviation of the radius mean value from the resting radius value during the oscillation (dashed red). B (right), top: radius-time curve of bubble displaying expansion-only (solid blue) and radius mean value during oscillation (solid red). B (right), bottom: A1: first-order term of the expansion-only time curve (solid black) and A0: deviation of the radius mean value from the resting radius value during the oscillation (dashed red). Note that for expansion-only behavior A0 is positive, while for a compression-only oscillation A0 is negative.

3.3. RESULTS

The described experimental protocol was successfully applied to a total of 8 bubbles (4 single frequency and 4 step-FM experiments). For each bubble, the total time of observation was between 8 and 12 minutes; all bubbles exhibited a monotonic decrease of bubble size with time. In Fig. 3 the typical recordings from a deflating bubble are shown as an example; in this experiment, 2 MHz (single frequency) pulses were transmitted and the radius changed from 2 μm to 1.4 μm radius in about 100 pulses. Figure 3:3 shows that the oscillation characteristics change several times during the deflation process. It is possible to distinguish two different phases, which are alternating: in one phase (phase A), the oscillation slowly progresses towards compression-only behavior while almost no change in the resting size is noticeable. In the other phase (phase B), the bubble oscillations progress from a compression-prevalent behavior to a more symmetric one, while a significant reduction in the resting size is simultaneously observed. At the end of the experiment, the bubble has reached a stable size, and it shows compression-only behavior.

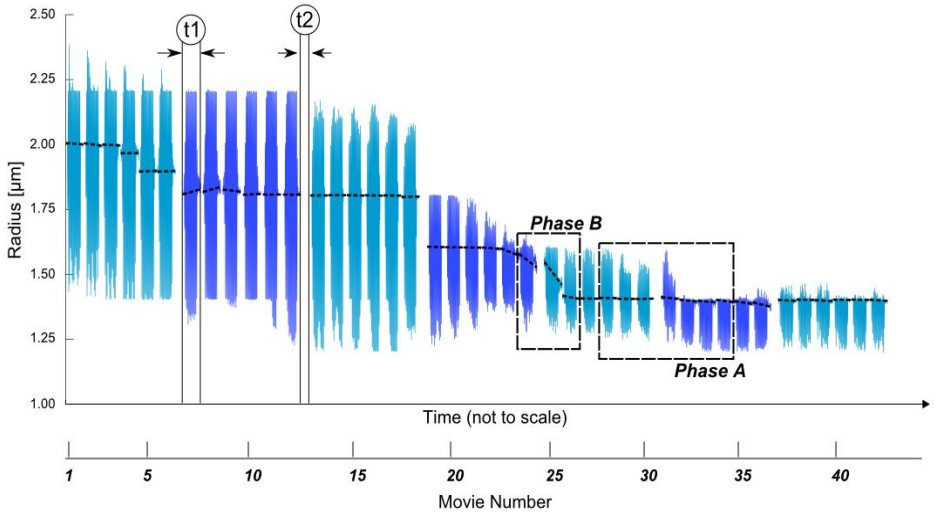

Figure 3:3 Bubble oscillations recorded using single-frequency excitation (2 MHz pulses, 20 ms PRI). One bubble oscillation (see, e.g., interval t1 in the above figure) is recorded for 7.5 μs every 100 ms (corresponding to 5 TX pulses). After 6 consecutive recordings (here highlighted by the same shade) the experiment is paused for 2 minutes (interval t2). The bubble resting radius during the recordings is represented by black dashed lines. Examples of phase A and phase B, respectively, are highlighted by the rectangular boxes. At the end of the experiment, the bubble shows compression-only behavior with a resting radius of about 1.4 μm.

In Figure 3:4, the typical evolution of a bubble deflating using a step-FM excitation sequence is shown. The bubble here deflated from a size of 2.2 μm to 1.1 μm in radius following a series of 800 pulses. At the end of the experiment, compression-prevalent oscillations are observed. Phase A and phase B are distinguishable here as well. Notably, phase B can, in some cases, lead to a complete reversal of the oscillation characteristics, with the bubble going instantly from a compression-only behavior to an expansion-only behavior.

A similar progression of oscillation shapes was observed in all other experiments as well. All bubbles had a starting size in the 2.2 μm – 1.6 μm radius range and the final observed radius was about 1.4 μm in the 4 single frequency experiments, usually reached in 50-150 pulses, and about 1.1 – 1.2 μm in the 4 step-FM experiments, usually reached in 300-500 pulses. As discussed in the next section, both the number of pulses and the higher frequencies used in step-FM accounts for the difference in the final stable size.

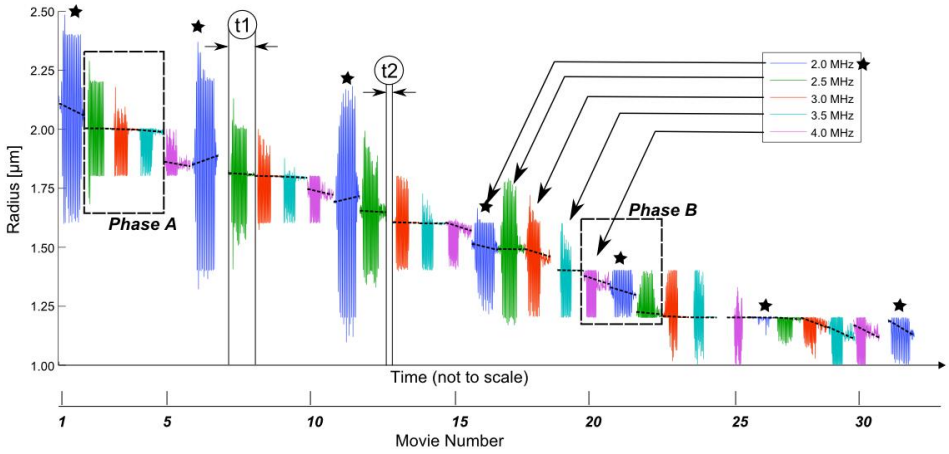

Figure 3:4 Bubble oscillations recorded from a single bubble using step-FM excitation at 4 ms PRI. One bubble oscillation (see, e.g., interval t1 in the above figure) is recorded for 7.5 µs every 104 ms (corresponding to 26 TX pulses); every 6th recording, the experiment is paused for 2 minutes (interval t2). The bubble resting radius during the recordings is represented by black dashed lines. 2 MHz oscillations are marked with a star. Examples of phase A and phase B, respectively, are highlighted by the rectangular boxes. At the end of the experiment, the bubble radius is approximately 1.1 µm and the bubble oscillations show a strong prevalence of compression-only behavior. The examples shown in Fig. 2 correspond to movies 22 and 27 in this figure.

3.4. DISCUSSION

Direct optical tracking of the bubble is a convenient method to characterize the bubble behavior, as it allows for a direct quantification of both the bubble size and its US-driven oscillations. Given our specific interest in the long-time behavior changes, we recorded the bubble oscillations multiple times during the deflation process: this strategy offered a reasonable sampling of the deflation process while reducing the total duration of the experiment to less than 12 minutes, thus limiting the possible influence of spontaneous bubble dissolution.

It is observed that US-induced bubble deflation occurs even at the low acoustic pressure we used. Bubbles having a starting radius around 2 µm shrink down to a metastable radius of about 1.4 µm after receiving 50-150 pulses at 2 MHz. Once the bubbles reach a radius of about 1.4 µm, they exhibit a quasi-static response to the 2 MHz pulses and display compression-only behavior. Many additional pulses, up to about a thousand, are needed to induce further bubble shrinkage. The achievement of a metastable size in bubbles deflated using single-frequency US pulses was observed also in other studies [5][6][13].

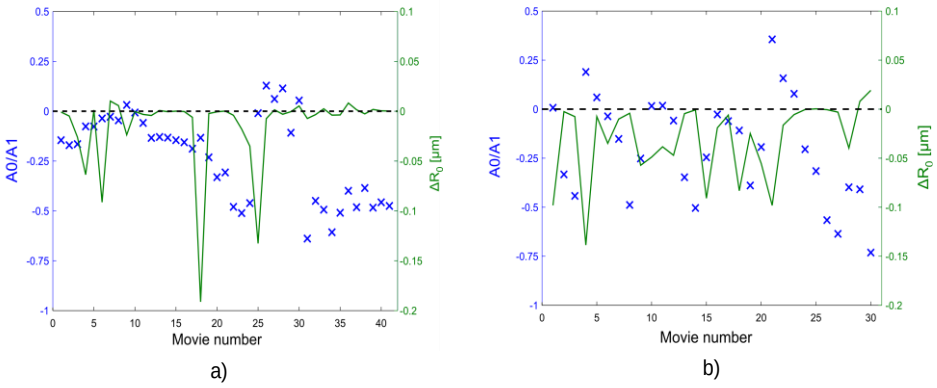

Figure 3:5 A_0/A_1 ratio versus record number (blue crosses) and changes in the resting radius (ΔR_0) versus record number (green solid line). A. (left) refers to the bubble recordings shown in Fig. 3 (single frequency). B (right) refers to the bubble recordings shown in Fig. 4 (Step-FM). In both examples it can be noted that near a discrete radius decrease, the A_0/A_1 ratio increases, eventually leading to a predominantly expansion-only behavior.

The step-FM experiments have shown that: 1) bubbles starting in the 2 μm radius range can shrink down to a radius of 1.1 μm; 2) the total number of pulses required to shrink the bubble from 2 μm to 1.4 μm radius is roughly five times greater than the number of pulses required in the single frequency experiments.

These observations suggest that the bubbles are more rapidly deflated when the excitation frequency is closer to resonance. According to previous studies, in fact, the resonant frequency for a lipid-shelled microbubble about 2 μm in radius, is close to 2 MHz [14]. As the bubble shrinks, its resonance frequency increases [15], until the 2 MHz excitation does not solicit anymore a visible bubble deflation. In this case, a metastable size is reached. On the other hand, in the step-FM experiments frequencies higher than 2 MHz were used as well: while the bubble deflates from 2 μm down to 1.4 μm, pulses with a frequency higher than 2 MHz offer a negligible contribution. Accordingly, we found that in step-FM roughly five times as many pulses as in single frequency experiments are required to deflate the bubble down to 1.4 μm. The deflation process in this case continues below 1.4 μm, because higher frequencies are used. The process stops at 1.1 μm, when the bubble resonant frequency is higher than the highest frequency used in the step-FM sequence.

In Figure 3:5, the A_0/A_1 ratio obtained from the oscillations shown in Fig.3 and Fig.4 (Figs. 5A and 5B, respectively), are correlated with the change in the resting radius (ΔR_0). Both A_0/A_1 and ΔR_0 are plotted as a function of the record number. Here, the occurrences of the so-called phase A are visible as a decrease in the A_0/A_1 ratio over consecutive pulses, while the ΔR_0 stays repeatedly near zero, indicating little or no

change in resting radius; as an example of this, see Fig. 5A, between movies 14-17 and Fig. 5B, between movies 21-26. On the other hand, the so-called phase B occurs when negative peaks in ΔR_0, indicating a rapid bubble shrinkage, are correlated with an instant increase of A_0/A_1 ratio; as an example, see Figure 3:5-a, at the pulse number 25 and Figure 3:5-b, at pulses 4 and 21. It should be noted that even though during phase B A_0/A_1 increases, it may end up with a negative value, indicating that the bubble oscillation is still biased towards compression.

The alternating phases A and B suggest that two different phenomena contribute to the bubble deflation in a predominant way. We compare these observations against the bubble oscillation model proposed by Marmottant *et al.* [16]. This model suggests that compression-only and expansion-only behaviors occur when the bubble is in a "buckled" and "ruptured" state, respectively. A bubble in a "buckled" state has a shell with a zero effective surface tension and zero elasticity, and can be easily compressed because of its shell buckling and reversibly changing between a spherical and a buckled, non-spherical shape. Conversely, a bubble in a "ruptured" state has a shell that can reversibly break into separate domains. Consequently, the gas core is exposed to the surrounding liquid and adopts its effective surface tension. The ruptured shell allows the bubble to easily expand. Therefore, the elastic contribution here is zero.

In between the "ruptured" and the "buckled" state, the Marmottant model identifies an elastic regime, where the shell effective surface tension σ changes linearly with the bubble surface area, or with the square of the radius; this relation is described as

$$\sigma(R) = \chi\left(\frac{R^2}{{R_b}^2} - 1\right) \tag{3.3}$$

where R is the instantaneous bubble radius, R_b is the bubble resting radius when the bubble is in a buckled state, and χ is the shell elastic modulus.

In phase A we observe a progressive shift towards compression-only. This suggests that the bubble is progressively losing surface tension, possibly because of diffusive gas loss. From Eq. (1), we expect the resting radius to decrease as well. For a bubble going from the ruptured state ($\sigma = \sigma_w = 0.0728$ N/m) to the buckled ($\sigma = 0$ N/m) state, the predicted radius shrink can be calculated following Overvelde *et al.*[17]:

$$\mathrm{R}_r - \mathrm{R}_b = \mathrm{R}_b\left[\left(\sqrt{\frac{\sigma_w}{\chi} + 1}\right) - 1\right] \tag{3.4}$$

In Fig. 4, between movies 22 and 28, the bubble goes from expansion-only to compression-only, reaching a final resting radius of about R_b = 1.2 μm; unfortunately, to the best of the authors' knowledge, no direct measurement of the elastic modulus (χ) of Definity™ contrast agent bubbles 2-4 μm in diameter exists. Nevertheless, Overvelde *et al.* [17] have shown that, at very low acoustic pressures, BR-14 contrast agents in the "elastic" regime of Marmottant model typically have $\chi = 2.5$ N/m.

Substituting R_b = 1.2 μm and $\chi = 2.5$ N/m in (2) the expected overall bubble shrinkage results in a value of about 14 nm. This value falls about 50% below the final resolution of our optical setup, and it is thus compatible with the observed bubble dynamics during phase A. Although, given the limited data and associated statistics, the physical phenomena driving phase A cannot be fully described, it seems reasonable to argue that, as previously stated: a) the bubble is mainly losing effective surface tension in this phase A, hence progressing towards compression-only behavior; b) diffusive gas loss is most likely responsible for this phenomenon.

Phase B can be explained through another physical mechanism. Borden [9] showed that, during bubble dissolution, the bubble shell can turn from a buckled state to a fully elastic monolayer through expulsion or detachment of excess shell material, termed budding. This process causes the remaining lipids to rearrange back into a monolayer, resealing the gaps left by the expelled material. The shedding of excess lipid material results in an increase of the effective surface tension, resulting in an immediate decrease of the buckling radius of the bubble R_b, see Eq. 1. From these principles and those of the model of Marmottant *et al.*, it follows that the behavior observed in phase B can be explained by material shedding from the shell, which may then be immediately followed by gas loss through the increased capillary forces.

As a final remark, although the Marmottant model is a valuable reference when discussing bubble oscillations, it does not address the bubble dissolution phenomenon. Comparison with existing models on bubble dissolution is therefore crucial for a complete understanding of the phenomena here reported. Referring to the extensive bubble modeling by Sarkar and Katiyar [18], and Kwan and Borden [8], micron-sized encapsulated bubbles in an air-saturated liquid grow in radius because of air intake from the surrounding liquid, before starting to shrink in a spontaneous process eventually leading to complete bubble dissolution. Although we did not observe any growing in our experiments, this may be due to the fact that this is expected to only last about 100 s, while the preparation of bubbles in our setup easily takes several minutes.

Furthermore, the model predicts that spontaneous bubble shrink from 100% to 70% (corresponding to the shrink radius from 2 μm to 1.4 μm observed in our single

frequency experiments) takes about 600 seconds. In our case, the shrinking process is dictated by the number of pulses, more than by time, and shrinking by 30% typically needs 50-150 pulses. These may cover less than 2 minutes, depending on the sampling frequency. It is therefore reasonable to assume that in our experiments the contribution to the deflation process coming from spontaneous gas diffusion is negligible in comparison to the US-induced phenomena contribution.

Katiyar, Sarkar *et al.* outline that the bubble gets more stable as the surface tension of the shell decreases [18][19]; this would suggest that, as the bubble approaches a buckled state ($\sigma = 0$ according to the Marmottant model), the spontaneous diffusive process slows to a halt, thereby leaving US-induced phenomena as the only observable phenomena. However, it was also found that $\sigma = 0$ only gives neutral stability [20], and therefore perturbations (either US-induced or randomly occurring) would still cause the bubble to further lose gas, eventually leading to total bubble dissolution. This seems to clash with our finding of a metastable radius at the end of the experiment, a phenomena also reported in different works [8][13]. It is shown [20] that a shell capable of sustaining a net compressive stress ($\sigma < 0$) would result in the bubble achieving actual stability, possibly indicating that the $\sigma = 0$ condition for a buckling shell in the Marmottant model could be revised; however, no certain conclusions can be drawn at present time, and the issue remains as an open question.

3.5. CONCLUSIONS

Although US-induced bubble deflation is a well-known and often described phenomenon, the related mechanisms of deflation are currently poorly understood. The findings presented in this work, as well as in prior work by other researchers cited here, suggest that the bubble deflation most likely occurs as a combination of lipids shedding and gas loss. Here, we have indicated that during the process of deflation, the bubble can vibrate symmetrically or very asymmetrically (expansion-only and compression-only behaviors). In addition to that, the deflation process does not completely dissolve the bubble, but rather drives the bubble towards a final stable or metastable size; such final size was found to be linked to the US frequency used, but not to the bubble size prior to deflation.

The observed phenomena could be exploited to optimize the contrast imaging techniques. For example, pushing the microbubbles towards a metastable compression-only behavior, such as that typically observed after prolonged excitation, could also be advantageous for subharmonic imaging, as the conditions for a strongly non-symmetrical oscillation [12] directly coincide with the generation of a subharmonic response of the bubbles [21].

REFERENCES

[1] Calliada, F.; Campani, R.; Bottinelli, O.; Bozzini, A.; and Sommaruga, M.G.; "Ultrasound contrast agents. Basic principles", *European Journal of Radiology*, 27 (1998), pp. S157-S160, 1998.

[2] De Jong, N.; Frinking, P.J.A.; Bouakaz, A.; and Ten Cate, F.J.; "Detection procedures of ultrasound contrast agents", *Ultrasonics* 38 (2000), pp. 87-92, 2000.

[3] Phillips, P.J.; "Contrast pulse sequences (CPS): imaging nonlinear microbubbles," *Ultrasonics Symposium, 2001 IEEE* , vol.2, no., pp.1739-1745 vol.2, 2001.

[4] Quaia, E.; "Contrast-specific ultrasound techniques", *Radiol. Med.* (2007) 112:473–490.

[5] Guidi, F.; Vos, H.J.; Mori, R.; De Jong, N.; Tortoli, P.; "Microbubble characterization through acoustically induced deflation", *Ultrasonics, Ferroelectrics and Frequency Control, IEEE Transactions on* , vol.57, no.1, pp.193-202, Jan. 2010.

[6] Borden, M.A.; and Longo, M.L.; "Dissolution behavior of lipid monolayer-coated, air-filled microbubbles: effect of lipid hydrophobic chain length", *Langmuir* **2002**, 18, 9225-9233.

[7] Chomas, J.E.; Dayton, P.A.; Allen, J.; Morgan, K.; and Ferrara, K.W.; "Mechanisms of contrast agent destruction", *Ultrasonics, Ferroelectrics and Frequency Control, IEEE Transactions on* , vol.48, no.1, pp.232-248, Jan. 2001.

[8] Kwan, J.J.; and Borden, M.A.; "Microbubble dissolution in a multigas environment", American Chemical Society, *Langmuir* 2010, 26(9), 6542-6548.

[9] Borden, M.A.; Kruse, D.E.; Caskey, C.F.; Zhao, S.; Dayton, P.A.; and Ferrara, K.W.; "Influence of lipid shell physicochemical properties on ultrasound-induced microbubble destruction", *Ultrasonics, Ferroelectrics and Frequency Control, IEEE Transactions on* , vol.52, no.11, pp.1992-2002, Nov. 2005.

[10] Chin, C.T.; Lancée, C.; Borsboom, J.;Mastik, F.; Frijlink, M.E.; de Jong, N.; Versluis, M.; and Lohse, D.; "Brandaris 128: A digital 25 million frames per second camera with 128 highly sensitive frames", *Review of scientific instruments*, vol.74, no.12, Dec. 2003.

[11] Ricci, S.; Boni, E.; Guidi, F.; Morganti, T.; and Tortoli, P.; "A programmable real-time system for development and test of new ultrasound investigation methods", *Ultrasonics, Ferroelectrics and Frequency Control, IEEE Transactions on* , vol.53, no.10, pp.1813-1819, Oct. 2006.

[12] Sijl, J.; Overvelde, M.; Dollet, B.; Garbin, V.; de Jong, N.; Lohse, D; and Versluis, M; " "Compression-only" behavior: A second-order nonlinear response of ultrasound contrast agent microbubbles", *J. Acoust. Soc. Am.*, vol. 129, Issue 4, pp. 1729-1739 (2011).

[13] Cox, D.J.; and Thomas, J.L.; "Ultrasound-induced dissolution of lipid-coated and uncoated gas bubbles", American Chemical Society, Langmuir 2010, 26(18), 14774-14781.

[14] Overvelde, M.L.J.; "Dynamics of coated microbubbles: an introduction", in *Ultrasound Contrast Agents – Dynamics of Coated Bubbles*, Ph.D. Thesis, Universiteit Twente, 2010, pp 10-15.

[15] Leighton, T.G.; "The radiating spherical bubble", in *The Acoustic Bubble*, Ed. Academic Press, 1994, p.139.

[16] Marmottant, P.; van der Meer, S.; Emmer, M.; and Versluis, M.; "A model for large amplitude oscillations of coated bubbles accounting for buckling and rupture", *J. Acoust. Soc. Am.*, vol. 118, Issue 6, pp. 3499-3505 (2005).

[17] Overvelde, M.; Garbin, V.; Sijl, J.; Dollet, B.; de Jong, N.; Lohse, D.; and Versluis, M.; "Nonlinear shell behavior of phospholipid-coated microbubbles", *Ultrasound in Medicine and Biology* 36(12): 2080-2092 (2010).

[18] Katiyar, A.; Sarkar, K.; and Pankaj, J.; "Growth and dissolution of an encapsulated contrast microbubble " *Ultrasound in Medicine and Biology* 35(8): 1385-1396 (2009).

[19] Katiyar, A.; Sarkar, K.; and Pankaj, J.; "Effects of Encapsulation Elasticity on the stability of an Encapsulated Microbubble." *Journal of Colloid and Interface Science* 336: 519-525 (2009).

[20] Katiyar, A.; and Sarkar, K.; "Stability analysis of an encapsulated microbubble against gas diffusion." *Journal of Colloid and Interface Science* 343(1): 42-47 (2010).

[21] J. Sijl, B. Dollet, M. Overvelde, V. Garbin, T. Rozendal, N. De Jong, D. Lohse, e M. Versluis, "Subharmonic behavior of phospholipid-coated ultrasound contrast agent microbubbles.", *Journal of the Acoustical Society of America*, vol. 128, n°. 5, pp. 3239–3252, (2010).

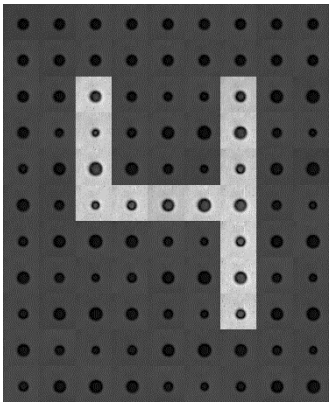

4. Multi Frequency Imaging

Abstract **– The nonlinear response to ultrasound of contrast agent microbubbles is a key feature that is commonly used in ultrasound imaging to identify and differentiate such microbubbles from the surrounding tissue. Traditionally, second harmonic imaging is employed to detect ultrasound contrast agents; however, as wave propagation through the tissue also generates nonlinear components, relying on second harmonic only can sometimes provide unsatisfactory results in terms of both specificity and sensitivity to ultrasound contrast agents (UCA). In this chapter, the advantages of imaging whilst using more than a single frequency are explored. In the first part of this chapter, it is demonstrated how multi-frequency transmission can be effectively used as a novel approach to image tissue at a higher framerate than traditional approaches, while maintaining compatibility with second harmonic imaging; this laid the foundations to eventually perform fast harmonic imaging of UCA within tissue, and can eventually lead to a high specificity imaging where the different frequency responses of UCA and tissue are tracked and separated. In the second part of this chapter, the advantages of using UCA imaging based on the third or higher harmonics, i.e. "superharmonic" imaging, were explored using a custom built dual-frequency probe for cardiac imaging. In both investigations multi frequency imaging modes are shown to be advantageous compared to a traditional B-mode imaging approach.**

4a. appeared as a full paper on IEEE Transactions on Ultrasonics, Ferroelectrics and Frequency Control, vol. 60, no. 11, pp. 2310–2320, 2013; by L. Demi, J. Viti, L. Kusters, F. Guidi, P. Tortoli, and M. Mischi, © IEEE 2013.

4b appeared as a proceedings paper for the 20th International Symposium on Nonlinear Acoustics, Lyon, France, June 29 - July 3 2015; by D. Peruzzini, J. Viti, P. Tortoli, M.D. Verweij, N. de Jong and H.J. Vos.

4a. Implementation of Parallel Transmit Beamforming Using Orthogonal Frequency Division Multiplexing – Achievable Resolution and Interbeam Interference

The speed of sound in the human body limits the achievable data acquisition rate of pulsed ultrasound scanners. To overcome this limitation, parallel beamforming techniques are used in ultrasound 2-D and 3-D imaging systems. Different parallel beamforming approaches have been proposed. They may be grouped into two major categories: parallel beamforming in reception and parallel beamforming in transmission. The first category is not optimal for harmonic imaging; the second category may be more easily applied to harmonic imaging. However, inter-beam interference represents an issue. To overcome these shortcomings and exploit the benefit of combining harmonic imaging and high data acquisition rate, a new approach has been recently presented which relies on orthogonal frequency division multiplexing (OFDM) to perform parallel beamforming in transmission. In this paper, parallel transmit beamforming using OFDM is implemented for the first time on an ultrasound scanner. An advanced open platform for ultrasound research is used to investigate the axial resolution and interbeam interference achievable with parallel transmit beamforming using OFDM. Both fundamental and second-harmonic imaging modalities have been considered. Results show that, for fundamental imaging, axial resolution in the order of 2 mm can be achieved in combination with interbeam interference in the order of -30 dB. For second-harmonic imaging, axial resolution in the order of 1 mm can be achieved in combination with interbeam interference in the order of -35 dB.

4a.1. INTRODUCTION

Nowadays a wide range of parallel beamforming techniques exist which have been developed to generate ultrasound images at a high data acquisition rate. A high data acquisition rate can be spent to increase the frame rate, to increase the field of view, to produce independent images that can be afterwards averaged in order to reduce noise, or to reduce the scanning time. Three-dimensional ultrasound imaging is an application which requires the high data acquisition rate enabled by parallel

beamforming techniques [1], [2]. Different parallel beamforming approaches are proposed and reported in the literature. They may be grouped in two major categories: 1) parallel beamforming in reception and 2) parallel beamforming in transmission.

The techniques which belong to the first category [3], [4], [5], [6], [7] employ a wide beam or a plane wave in transmission to insonify a large volume and, when receiving, multiple parallel lines are acquired by means of narrow receiver beams. As a consequence, they are not optimal to perform harmonic imaging. In fact, the utilization of a wide beam or plane wave in transmission results in the generation of lower absolute pressure values, when compared to focused ultrasound beams, and conflicts with the demand for high-amplitude pressure wave fields, which are necessary to generate the harmonic components.

On the other hand, the techniques which belong to the second category are more suitable for harmonic imaging, since narrow parallel beams may be used in transmission and focusing may be employed to increase the amplitude of the generated pressure wave fields. Hence, the benefit of combining harmonic imaging and a high data acquisition rate may be exploited for imaging. Harmonic imaging is becoming the standard in pulse-echo applications as it both improves the image resolution and reduces the effect of clutter and side and grating lobes [8], [9], [10], [11], [12] with respect to fundamental imaging. Nevertheless, in case parallel beamforming is performed in transmission, interbeam interference represents an issue. A possible solution to this problem may come from different combinations of transmit and receive apodizations [13] or beam transformation techniques [14]. Recently, an alternative solution has been presented. This novel approach relies on orthogonal frequency division multiplexing (OFDM) [15], [16] to perform parallel beamforming in transmission. Frequency division multiplexing is not new to ultrasound applications [17]. With this technique multiple beams may be generated by allocating to each beam a portion of the available bandwidth in transmission. Furthermore, each beam may be independently steered in a specific direction. The pressure wave fields generated in this fashion propagate in each specific steered direction and next, appropriate coherent demodulation and application of low-pass filters in reception is used to discriminate between echoes coming from the different directions of observation. Other than OFDM, alternative methods exist which can be used as simultaneous transmit methods, i.e. methods taking advantage of coded excitation and chirp signals [18], [19], [20], [21].

When parallel transmit beamforming using OFDM is applied to second harmonic imaging, numerical studies shows the ability of this method to reduce the presence of unwanted side lobes and to increase the amplitude of the main beam as compared to parallel beamforming in reception [22]. As a drawback, utilization of narrow bandwidth

pulses results in a reduction of the axial resolution. Moreover, axial resolution and interbeam interference are interlinked. In this paper, parallel transmit beamforming using OFDM is for the first time implemented on a real pulse-echo ultrasound imaging system. In particular, an advanced open platform for ultrasound research (ULA-OP) [23], [24] is used in combination with a linear array probe. The aim of this study is to characterize the performance of parallel transmit beamforming using OFDM, and in particular to investigate the achievable axial resolution and interbeam interference. Both fundamental and second harmonic imaging modalities have been considered.

Theoretical guidelines for the application of the described method on a real pulse-echo ultrasound imaging system are given in Section 3.2. The methodology and the parameters used for the experimental validation are described in Section 3.3. The results obtained are shown in Section 3.4. Discussion and final conclusion are reported in Section 3.5 and 3.6, respectively.

4a.2. THEORETICAL GUIDELINES

In this Section, the theoretical guidelines for the proposed technique are given. The symbols F0 and 2H are used to describe fundamental and second harmonic related quantities, respectively, e.g. f_i^{F0} i and f_i^{2H} denote the modulation frequency of the fundamental and second harmonic component relative to the ith beam.

4a.2.1. Basic principles

Figure 1 illustrates, both in transmission and reception, the basic principles of parallel transmit beamforming using OFDM. With this technique, multiple beams may be generated in transmission by allocating to each beam a portion of the transducer bandwidth. Hence, pulses having a different modulation frequency, e.g. f_1^{F0}, f_2^{F0} and f_3^{F0} , are required in transmission. The beams generated in this manner may be independently steered in different directions and multiple lines may be consequently acquired in parallel. The larger the spatial overlap amongst the generated beams the stronger the interbeam interference.

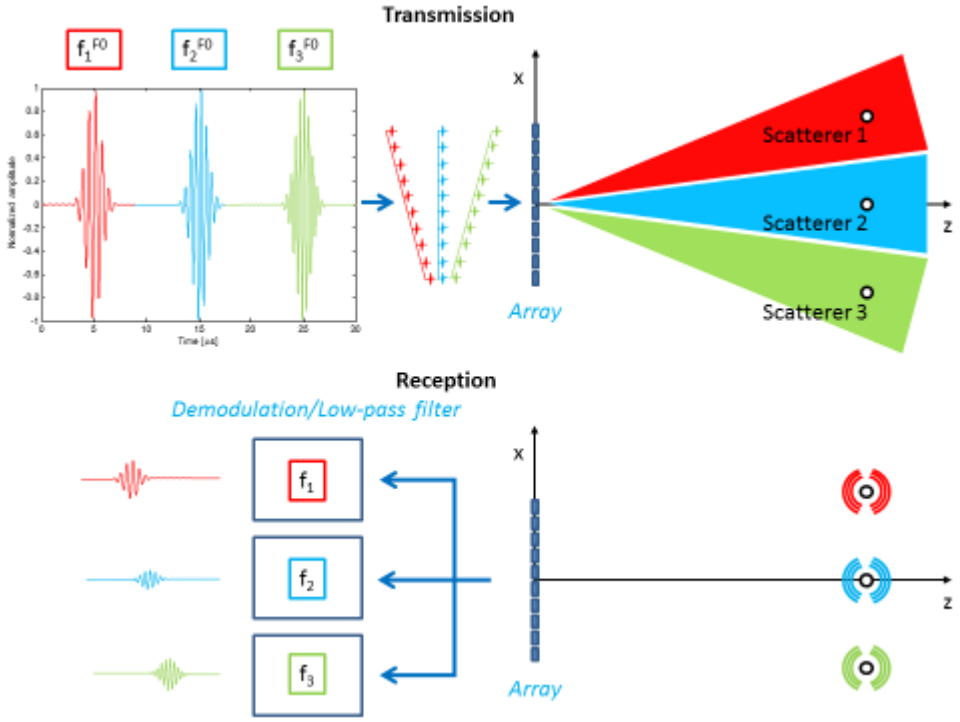

Figure 4:1 Transmission and reception phase for parallel transmit beamforming using orthogonal frequency division multiplexing.

Further, when applying parallel transmit beamforming by means of OFDM, appropriate time delay between the different beams is necessary to avoid both the time overlap of the pulses during transmission, in order to be able to employ per each pulse the maximum applicable signal strength, and the formation of unwanted mixing frequencies components [22].

The pressure wave fields generated in this fashion propagate through the insonified volume, and related second harmonic components, respectively centered at twice the transmitted frequencies, i.e. f_1^{2H} , f_2^{2H} and f_3^{2H} , are formed. Hence, scattering waves, modulated at the fundamental and second harmonic frequencies, are generated.

In reception, the scattered waves are acquired, demodulated accordingly to the desired center frequency, i.e. f_1, f_2 and f_3, and filtered using appropriate low-pass filters. The demodulation frequencies may be tuned at the fundamental or second harmonic frequencies, depending whether fundamental or second harmonic imaging is performed. The low-pass filters determine, in combination with the time duration of the pulses used, the axial resolution, and are essential to discriminate between echoes coming from the different beams and to suppress the interbeam interference. Because

of the time delay which is required between the transmitted pulses the interbeam interference manifests itself with the appearance, along each line, of ghost echoes of a scatterer which are displaced from the position of the actual scatterer according to the delay applied between the beams.

4a.2.2. Transmission

When implementing the described parallel transmit beamforming technique on a real pulse-echo ultrasound imaging system, the bandwidth of the system (B_{system}) is the most limiting factor. Given the pulse bandwidth (B_{pulse}), B_{system} limits the number of beams which can be transmitted in parallel by means of OFDM. In particular, overlap between the fundamental and the second harmonic components must be avoided to guarantee the capability of discriminating between the different beams. This implies a maximum exploitable bandwidth condition.

In case N parallel beams are transmitted over a certain bandwidth (B_{trans}), the minimum and maximum modulation frequency used in transmission are

$$f_1^{F0} = f_{center} - \frac{1}{2}\left(B_{trans} - B_{pulse}\right), \tag{4.1}$$

$$f_N^{F0} = f_{center} + \frac{1}{2}(B_{trans} - B_{pulse}) \tag{4.2}$$

respectively, with f_{center} the center frequency used in transmission. Consequently, the maximum exploitable bandwidth condition, in case of Gaussian modulated pulses, equals [22]

$$B_{trans} < \frac{2}{3}\left(f_{center} + \frac{2-\sqrt{2}}{2}B_{pulse}\right). \tag{4.3}$$

The number of pulses which may be transmitted in parallel is thus

$$N = \frac{B_{trans}}{B_{pulse}} < \frac{2}{3}\left(\frac{f_{center}}{B_{pulse}} + \frac{2-\sqrt{2}}{2}\right). \tag{4.4}$$

Hence, for a given system, the only parameter which may be used to increase N while respecting the constraint of Equation (4.4), is B_{pulse}. In particular, N increases for decreasing B_{pulse}. The side effect of decreasing B_{pulse} is a reduction of the axial resolution of the system [22], as the latter is proportional to the pulse length p_l. For a given pulse shape, the relation between B_{pulse} and p_l is defined by the time bandwidth product TBWP, which can be written as [25]

$$TBWP = B_{pulse}p_l \tag{4.5}$$

In particular, for Gaussian pulses the -6 dB, -9 dB, and -12 dB TBWP equals 0.44, 0.67, and 0.89, respectively. Therefore, from Equations. (4.4) and (4.5), the axial resolution as a function of N can be defined as

$$A_r = c_0 p_l = c_0 \frac{TBWP}{B_{pulse}} > c_0 \frac{TBWP(3N - 2 + \sqrt{2})}{2f_{center}} \tag{4.6}$$

with A_r being the axial resolution and c_0 the speed of sound.

Another important transmission parameter is f_s, which defines the frequency separation between consecutive modulation frequencies used in transmission and is expressed as

$$f_s = f_i^{F0} - f_{i-1}^{F0}, \quad \text{with} \quad i \in [2, N] \tag{4.7}$$

In theory f_s equals B_{pulse}. In practice this parameter may be larger as to improve beam separation. As a result, N reduces and Equation (4.4) becomes

$$N = \frac{B_{trans}}{f_s} < \frac{2}{3}\left(\frac{f_{center}}{f_s} + \frac{2 - \sqrt{2}}{2}\frac{B_{pulse}}{f_s}\right) \tag{4.8}$$

Note that, given a fixed center frequency, f_s does not influence the axial resolution.

In addition to influencing the axial resolution, a consequence of utilizing OFDM, and hence different modulation frequencies, to transmit multiple distinguishable beams, is the variation, from beam to beam, of the achievable lateral resolution. For a rectangular aperture, the lateral resolution may in fact be approximated with [25].

$$L_r = FW \frac{\lambda_i z}{L} \tag{4.9}$$

FW represents the full width coefficient, which for a -6 dB, -9 dB and -12 dB width equals 1.2, 1.4 and 1.6, respectively. $\lambda_i = c_0/f_i^{F0}$ is the wavelength, z is the depth, and L is the lateral size of the rectangular aperture.

4a.2.3. Receiving Phase

When receiving, after having demodulated according to each specific modulation frequency, a low-pass filter is needed to extract the pressure wave field related to each beam. The cutoff frequency (f_{cutoff}) of the applied filter determines, in combination with f_s and p_l, the level of interbeam interference and may influence the axial resolution. In order to set an upper limit to the interbeam interference, the cutoff frequency is kept smaller than f_s.

When the cutoff frequency is set as to extract the entire pulse band, filtering does not affect the axial resolution. However, in case some frequency overlap between the spectra of different beams is tolerated, e.g. in order to increase the number of beams,

N, beyond the limit given by Equation (4.8), the cutoff frequency can be reduced in order to diminish the interbeam interference. If this circumstance applies, the cutoff frequency deteriorates the axial resolution [22]. In conclusion, from Equation (4.5) the following constraints can be adopted to set the cutoff frequency:

$$\frac{0.44}{p_l} < f_{cutoff} < f_s \tag{4.10}$$

Here a TBWP equal to 0.44 is used to set the lower limit of f_{cutoff}.

4a.2.4. Considerations for second harmonic imaging

Once the transmission parameters are defined, N does not vary for a given system, independently of the fact that fundamental or second harmonic imaging is performed. However, the frequency separation f_s doubles for the second harmonic components. Assuming a system with a flat frequency response, this implies that, when compared to fundamental imaging, a doubled cutoff frequency can be used in reception, while maintaining approximately the same interbeam interference. Hence, second harmonic imaging results in a more advantageous tradeoff between interbeam interference and cutoff frequency, and thus axial resolution, when compared to fundamental imaging. However, it is important to notice that the interbeam interference for second harmonic imaging, as compared to fundamental imaging, varies more significantly with the modulation frequency, as the amplitude of the second harmonic components rises linearly with frequency [26]. Finally, the achievable axial and lateral resolution improves for second harmonic imaging when compared to fundamental imaging [8], [9], [22].

4a.3. METHODOLOGY

Measurements are performed utilizing a LA533 linear array Esaote (Firenze, Italy) probe. The array consists of 192 elements,each having a size equal to 0.215 mm by 6 mm. The pitch equals 0.245 mm. The probe is connected to the ULA-OP system. This system is a flexible, powerful and portable ultrasound system, specifically developed for research purposes. The system design is based on high-level commercial integrated circuits and allows for a wide data access, which makes it optimal to investigate novel ultrasound modalities. An active aperture of 64 elements, focused at 40 mm depth, is used both in transmit and receive. Hanning apodization is utilized. No steering is applied. The active aperture is linearly shifted over the array to create a 129 line image. All measurements are performed in a water tank and nylon wires with a diameter of 0.1 mm are positioned at focus to act as targets. Fundamental and second harmonic imaging performance have been investigated for different combinations of modulation frequency, pulse length and cutoff frequency of the low-pass filters used in reception. Interbeam interference is evaluated as the ratio between the mean value of the intensity of the ultrasound image of the ghost wire and the mean value of the intensity of the ultrasound image of the actual wire. The mean values of the intensity are calculated over the -9 dB area around the relative maximum. To investigate the worst case scenario, interbeam interference is maximized by steering each beam is the same direction. The axial and lateral resolution are evaluated as the size of the target wire image along the direction parallel and perpendicular to

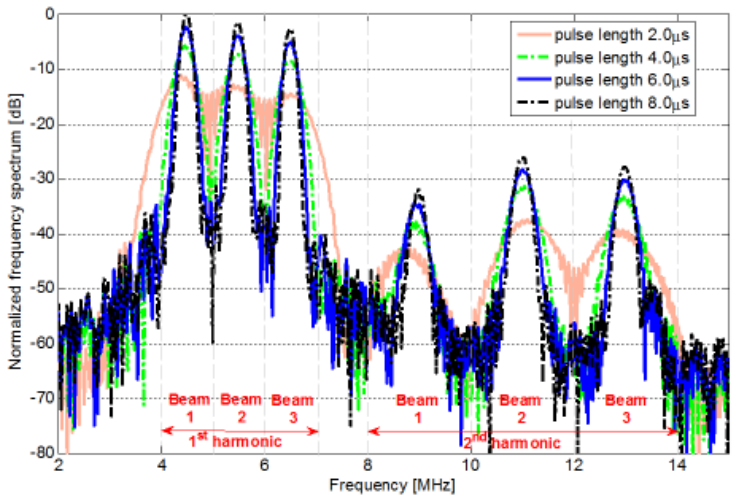

Figure 4:2 Normalized frequency spectrum of the received signal before demodulation and filtering, as obtained with four different pulse lengths and a frequency separation fs equal to 1 MHz

the beam axis, i.e. the z-axis and the x-axis, respectively. In particular, the -9 dB width is taken.

4a.3.1. Transmission

To obtain two clearly distinguishable bandwidths for the fundamental and second harmonic components within the bandwidth of the system, the f_{center} used equals 5.5 MHz. The maximum separation frequency and the shorter pulse length considered equal respectively 1.2 MHz and 2 μs. Consequently from Equation (4.8), three parallel beams are generated in transmission. Each beam is generated with a specific pulse. Gaussian pulses are used. The pulse modulation frequency equals $f_1^{F0} = 5.5\,MHz - f_s$, $f_2^{F0} = 5.5\,MHz$ and $f_3^{F0} = 5.5\,MHz + fs$ for beam 1, 2 and 3 respectively. The frequency separation fs is varied from 0.6 MHz to 1.2 MHz in steps of 0.2 MHz. The pulse length is kept the same amongst all three pulses and is varied from 2 μs to 8 μs in steps of 1 μs. Even though these pulses are relatively long for imaging applications, their use is discussed in detail in Section 4.4. Furthermore, a time delay of 10 μs is introduced between the transmitted beams.

4a.3.2. Reception

In both fundamental and second harmonic mode, after coherent demodulation (in second harmonic mode the demodulation frequency equals $f_1^{2H} = 11\,MHz - 2f_s$, $f_2^{2H} = 11\,MHz$ and $f_3^{2H} = 11\,MHz + 2f_s$ for beam 1, 2 and 3 respectively) a 3rd order Butterworth low-pass filter is used. The cutoff frequency is varied from 0.05 MHz $[min(0.44/p_l) = 0.44/8\,\mu s]$ to 1.2 MHz $[max(fs)]$, in steps of 0.05 MHz.

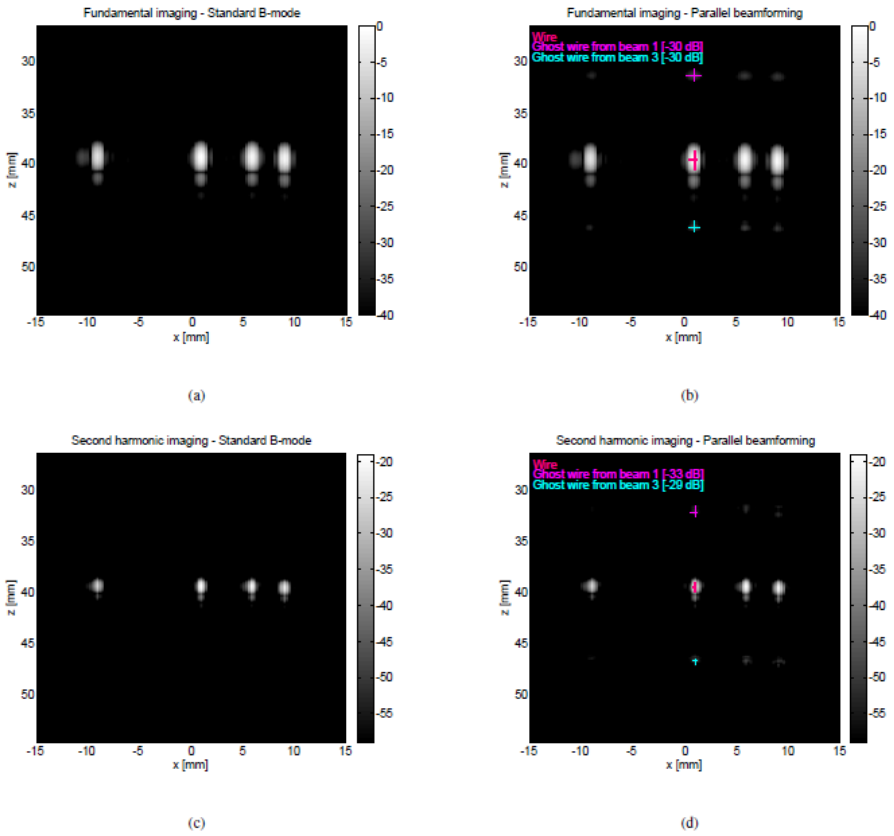

Figure 4:3 Standard B-mode and parallel beamformed, fundamental (a,b) and second harmonic (c,d), images as obtained with beam 2. The pulse length equals 3 μs, the frequency separation fs equals 1 MHz and the cutoff frequency equals 0.25 MHz in case of fundamental imaging and 0.5 MHz in case of second harmonic imaging

4a.4. RESULTS

Figure 4:2 shows the normalized frequency spectrum of the received signal before demodulation and filtering, as obtained with four different pulse lengths and a frequency separation fs equal to 1 MHz. Three distinct fundamental components, respectively centered at f_1^{F0} = 4:5 MHz, f_2^{F0} = 5:5 MHz and f_3^{F0} = 6:5 MHz, are visible together with three distinct second harmonic components, respectively centered at f_1^{2H} = 9 MHz, f_2^{2H} = 11 MHz and f_3^{2H} = 13 MHz. From this plot it emerges how using a shorter pulse, hence a better axial resolution, results in an increased interbeam interference. In fact, the shorter the pulse the broader its bandwidth, which translates to a larger interference between neighboring beams, as a greater portion of their frequency spectra overlaps. Conversely, the larger the frequency separation fs the smaller the interbeam interference.

Figure 4:3 shows an example of fundamental (a,b) and second harmonic (c,d) images as obtained with the described setup. In particular, the pulse length is 3 μs, the frequency separation fs is 1 MHz and the cutoff frequency is 0.25 MHz in case of fundamental imaging and 0.5 MHz in case of second harmonic imaging. The standard B-mode fundamental (a) and second harmonic (c) images, as obtained with beam 2 alone, are respectively compared with the parallel beamformed fundamental (b) and second harmonic (d) images obtained with beam 2, i.e. all three beams are transmitted but this image displays the result after filtering out beam 2 only. Normalized intensity values are in dB and colorbars display a 40 dB range. The normalization is performed with respect to the fundamental image obtained with the corresponding modality, i.e. standard B-mode or parallel beamforming respectively. The colored crosses indicate the dimensions of the -9 dB areas. When all three beams are transmitted, ghost wires appear in both fundamental and second harmonic images, as a consequence of the interbeam interference. In fundamental mode, the maxima of the intensity value of the ghost wire caused by the interference from beam 1 and 3 are both at -30 dB when compared to the maximum of the intensity value of the actual wire. In second harmonic mode, the maxima of the intensity value of the ghost wire caused by the interference from beam 1 and 3 are, respectively, at -33 dB and -29 dB when compared to the maximum of the intensity value of the actual wire. Note that a doubled cutoff frequency could be used for second harmonic imaging while maintaining approximately the same interbeam interference level. As introduced in Section II, this is explained by the increased frequency separation between the second harmonic components when compared to fundamental components. Furthermore, for the second harmonic image, a higher interbeam interference from beam 3, as compared to beam 1, is observable. This can be explained with the linear rise of the amplitude of the second harmonic component with frequency. Moreover, when compared to fundamental images, second harmonic images show, as expected, a general reduction of the intensity values, i.e. -20 dB, and an improved resolution [8], [9]. Note that interbeam interference may be further reduced by using a longer pulse or narrower low-pass filters, i.e. reducing the axial resolution, or employing larger frequency separation fs, i.e. reducing the number of beams which may be transmitted in parallel on a given band, B_{trans}. Moreover, a big frequency separation may result in a significant variation of the lateral resolution amongst the transmitted beams [25].

Figure 4:4 shows the fundamental (a) and second harmonic (b) lateral resolution versus the modulation frequency used, as obtained with a pulse length of 3 μs and a cutoff frequency of 0.5 MHz. As expected, a higher modulation frequency results in a better lateral resolution. Moreover, second harmonic imaging exhibits a better lateral resolution than fundamental imaging [8].

Figure 4:5 shows the fundamental (a) and second harmonic (b) axial resolution versus the cutoff frequency used, as obtained with beam 2 for different pulse lengths. As expected, a shorter pulse length, combined with a larger cutoff frequency, provides a better axial resolution. Moreover, second harmonic imaging results in a better axial resolution when compared to fundamental imaging [9]. For increasing cutoff frequency, the axial resolution improves, up to the point in which a plateau is reached. This occurs when the cutoff frequency is set as to extract the entire pulse bandwidth. In fact, the cutoff frequency at which the limit is reached increases for reduced pulse length.

Figure 4:6 and Figure 4:7 show, respectively, the fundamental and second harmonic interbeam interference (from beam 1) versus the axial resolution, as obtained with beam 2. Different combinations of pulse length, frequency separation and cutoff frequency are considered.

Only cutoff frequencies ranging from 0.2 MHz $[max(0.44/p_l) = 0.44/2\ \mu s]$ to 0.6 MHz $[min(f_s)]$ have been considered as to analyze the results in an interval in which not a too low axial resolution, nor a too high interbeam interference, would be achieved. Note that the curves obtained for the shortest pulse length (2 μs) show a significantly different trend. This is because the selected cutoff frequencies are not optimal to separate such wide-band pulses. Interbeam interference reduces for increasing pulse length and frequency separation, and reducing cutoff frequency. Axial resolution improves for reducing pulse length and increasing cutoff frequency. Second harmonic imaging results in a more advantageous tradeoff between interbeam interference and axial resolution when compared to fundamental imaging; given the combination of cutoff frequency, frequency separation and pulse length, second harmonic imaging results in fact in a reduced interbeam interference and improved axial resolution. This may be explained by the natural increase, by factor 2, in frequency separation combined with the intrinsic improvement in axial resolution. In view of the obtained figures, this technique shows optimal performance when applied to second harmonic imaging.

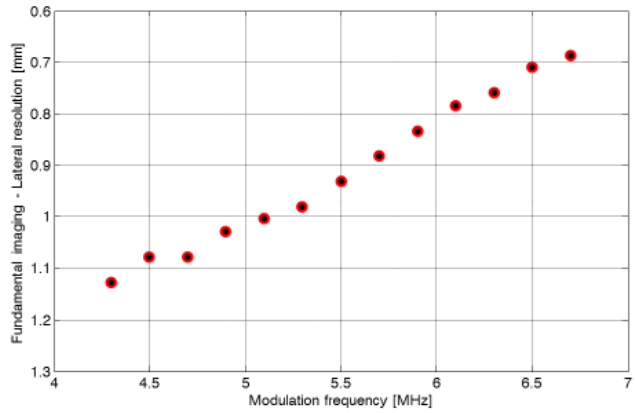

a)

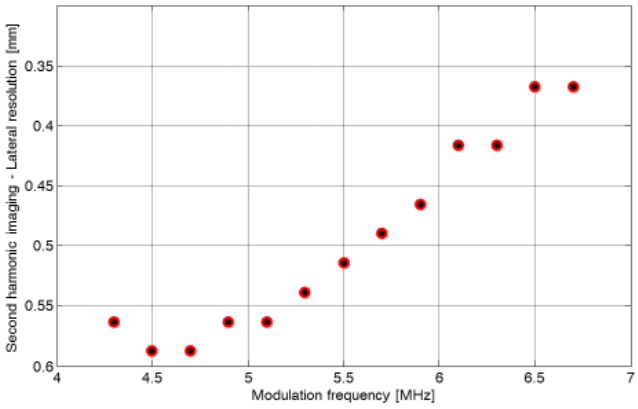

b)

Figure 4:4 Fundamental (a) and second harmonic (b) lateral resolution versus the modulation frequency used, as obtained with a pulse length of 3 μs and a cutoff frequency of 0.5 MHz

As a final example, in order to show what an ultrasound image formed with the proposed OFDM technique would look like, Fig. 8 shows a standard B-mode and a parallel beamformed second harmonic image of a single nylon wire. To obtain the best result in terms of axial resolution, while keeping the interbeam interference below -30 dB, the pulse length and cutoff frequency used equal 3 μs and 0.5 MHz, respectively. The B-mode second harmonic image is acquired linearly shifting the active aperture over the entire array, obtaining one line at a time transmitting a single driving signal at 5.5 MHz. On the other hand, to obtain the parallel beamformed image, the active aperture is linearly shifted over the array acquiring three adjacent lines at a time using

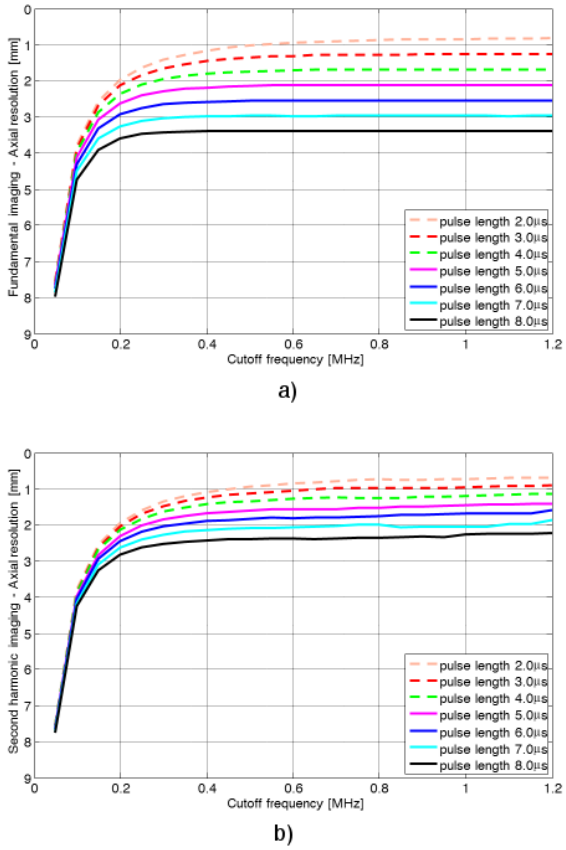

Figure 4:5 Fundamental (a) and second harmonic (b) axial resolution versus the cutoff frequency used, as obtained with beam 2.

a 4.5 MHz, 5.5 MHz, and 6.5 MHz pulse for the first, second and third parallel line so acquired, respectively. No steering is applied and the three beams are not transmitted simultaneously, a time delay of 10 μs is used between the transmitted beams. Intensity values are in dB. As expected, interbeam interference is below -30 dB. Moreover, a gain of the frame rate by a factor three is achieved for the parallel beamformed second harmonic image. As a drawback, the use of multiple frequencies to form three lines in parallel results, as compared to the standard single-frequency B-mode image, in a small degradation of symmetry in the obtained image.

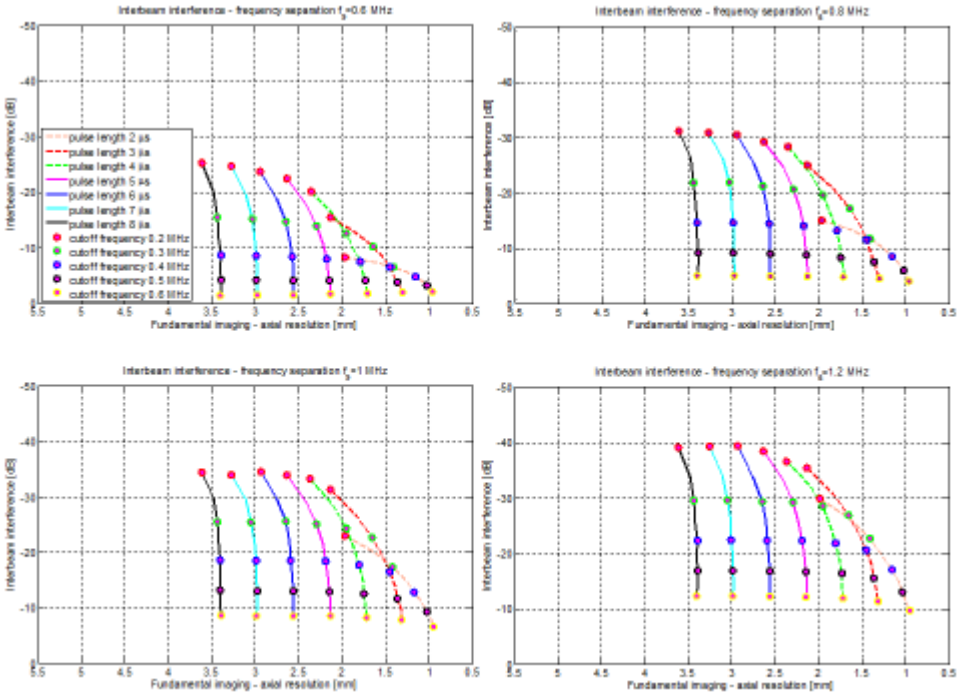

Figure 4:6 Fundamental imaging interbeam interference (from beam 1) versus the axial resolution as obtained for beam 2. Different combinations of frequency separation, pulse length and cutoff frequency are analyzed.

4a.5. DISCUSSION

In this paper, an experimental analysis on the achievable axial resolution and interbeam interference for parallel transmit beamforming using OFDM is presented for the first time. Both fundamental and second harmonic imaging modalities are investigated. Four general aspects must be taken into account when implementing this method:

1) The utilization of narrow bandwidth pulses, needed to enable the transmission of multiple parallel beams, reduces the axial resolution. Moreover, the achievable axial resolution is limited by the interbeam interference. These two quantities are in fact inversely related. The interbeam interference reduces for increasing pulse length and frequency separation, and for increasingly narrower low-pass filters. On the other hand, the axial resolution improves for decreasing pulse length and increasingly broader low-pass filters.

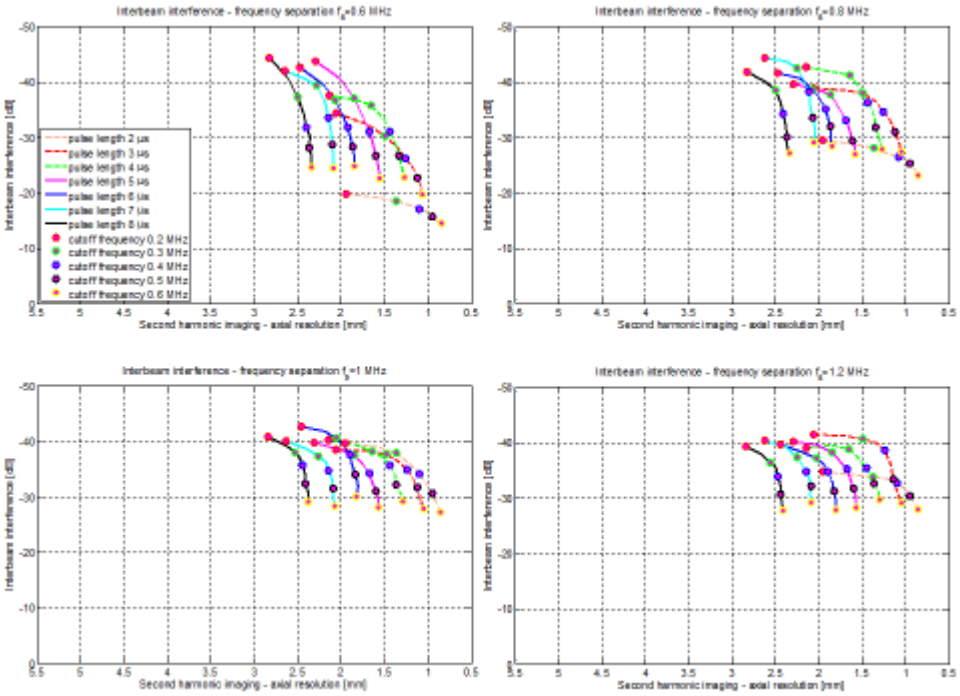

Figure 4:7 Second harmonic imaging interbeam interference (from beam 1) versus the axial resolution as obtained for beam 2. Different combinations of frequency separation, pulse length and cutoff frequency are analyzed

2) The frequency separation, f_s, determines, given a specific bandwidth, B_{trans}, the number of beams, N, which may be transmitted in parallel. Hence, a wide band transducer is required to transmit a significant number of parallel beams. Furthermore, the frequency separation determines the variation between the lateral resolution obtained with different beams. For the parameters analyzed in this paper, the variation remains limited to an absolute maximum variation in the order of 0.4 mm for fundamental imaging and in the order of 0.2 mm for second harmonic imaging.

3) A large frequency separation between the modulation frequency of each beam results in beam dependent attenuation. However, once the system is calibrated and all the parameters are set, a beam dependent compensation coefficient may be used to limit this problem. Since attenuation is negligible in water, this compensation is not performed in this paper. Tissue mimicking phantoms may be used to investigate the effect of frequency dependent attenuation on the applicability of the proposed method to realistic medical applications. Moreover, in case of a large frequency separation, compensation of the frequency response of the probe may be necessary. In this study, no compensation with respect to the frequency response of the probe is

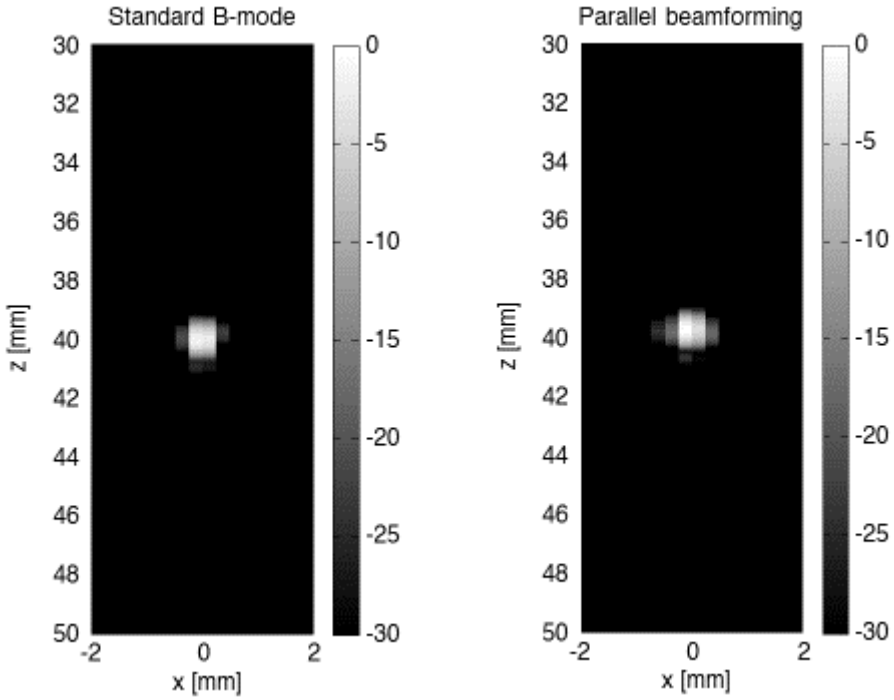

Figure 4.8 Standard B-mode and parallel beamformed second harmonic image, obtained with a single beam (beam 2) and three parallel beams, respectively. The pulse length is 3 μs, the frequency separation fs is 1 MHz and the cutoff frequency is 0.5 MHz. Intensity values are in dB.

employed. This is because the maximum relative variation of the frequency response of the probe on the bandwidth used is about 1 dB for fundamental imaging, and 2 dB for second harmonic imaging, and is therefore negligible next to the interbeam interference that was measured.

4) To avoid the formation of unwanted mixing frequencies, in case of second harmonic imaging, and in general to avoid signals overlap in time during transmission, small delays are necessary between the beams transmitted. These delays do not cumulate between consecutive scans, hence they do not affect the scanning time, and are much smaller than the time of flight normally observed in biomedical applications, e.g. in the order of a factor 10 in case of cardiac imaging. Nevertheless, these delays may cause the formation of a blind area in front of the transducer as the reception phase cannot start before the end of the transmission phase. The extent of the blind area B_a, in the *z*-direction, equals

$$B_a = \frac{c_0 T}{2} \tag{4.11}$$

with

$$T = (N-1)\Delta t + p_l \tag{4.12}$$

Here, c_0 represents the speed of sound, N the number of beams, Δt the delay between the beams and p_l the pulse length. To give a numerical example, using a pulse length of 3 μs, 3 parallel beams and an interbeam delay Δt equal to 10 μs, and assuming a speed of sound c_0 equal to 1500 m/s, the blind area B_a equals 17.25 mm. This problem may be solved using a separate set of array elements for transmission and reception, respectively.

4a.6. CONCLUSION

Orthogonal frequency division multiplexing may be used to perform parallel beamforming in transmission. With this technique each beam is allocated to a portion of the transducer bandwidth. Hence, parallel beams may be transmitted in order to increase the data acquisition rate of a given ultrasound scanning system. In this paper, an advanced open platform for ultrasound research (ULA-OP) is used to assess the axial resolution and interbeam interference achievable with parallel transmit beamforming using OFDM. Both fundamental and second harmonic imaging modalities have been investigated. Selection of the optimal parameters is essential and concerns a tradeoff between different quality measures, and thus is application dependent. However, the reduced axial resolution caused by the use of narrow-band pulses is probably the most relevant factor influencing the applicability of this technique. Moreover, the results presented in this paper have been obtained in water. The next step, to evaluate the applicability of this method to realistic medical applications, is to study its performances when applied to dispersive attenuative media. Results show that, with the described setup, an axial resolution in the order of 2 mm, in combination with an interbeam interference in the order of -30 dB, may be achieved for fundamental imaging. For second harmonic imaging, an axial resolution in the order of 1 mm, in combination with an interbeam interference in the order of -35 dB, may be achieved. However, despite the improved axial resolution and interbeam interference, signal intensity is reduced due to the lower amplitude of the second harmonic components when compared to the fundamental components. For both modalities three beams were transmitted in parallel. More beams may be transmitted in parallel at the cost of a reduced axial resolution or increased interbeam interference.

4b. Ultrasound Contrast Agent Imaging: Real-time Imaging of the Superharmonics

Currently, in medical ultrasound contrast agent (UCA) imaging the second harmonic scattering of the microbubbles is regularly used. This scattering is in competition with the signal that is caused by nonlinear wave propagation in tissue. It was reported that UCA imaging based on the third or higher harmonics, i.e. "superharmonic" imaging, shows better contrast. However, the superharmonic scattering has a lower signal level compared to e.g. second harmonic signals. This study investigates the contrast-to-tissue ratio (CTR) and signal to noise ratio (SNR) of superharmonic UCA scattering in a tissue/vessel mimicking phantom using a real-time clinical scanner. Numerical simulations were performed to estimate the level of harmonics generated by the microbubbles. Data were acquired with a custom built dual-frequency cardiac phased array probe. Fundamental real-time images were produced while beam formed radiofrequency (RF) data was stored for further offline processing. The phantom consisted of a cavity filled with UCA surrounded by tissue mimicking material. The acoustic pressure in the cavity of the phantom was 110 kPa (MI = 0.11) ensuring non-destructivity of UCA. After processing of the acquired data from the phantom, the UCA-filled cavity could be clearly observed in the images, while tissue signals were suppressed at or below the noise floor. The measured CTR values were 36 dB, >38 dB, and >32 dB, for the second, third, and fourth harmonic respectively, which were in agreement with those reported earlier for preliminary contrast superharmonic imaging. The single frame SNR values (in which 'signal' denotes the signal level from the UCA area) were 23 dB, 18 dB, and 11 dB, respectively. This indicates that noise, and not the tissue signal, is the limiting factor for the UCA detection when using the superharmonics in nondestructive mode.

4b.1. INTRODUCTION

Ultrasound is one of the most used imaging technologies in medicine. It is portable, free of radiation and relatively inexpensive, especially if compared with imaging techniques like magnetic resonance and computed tomography. Ultrasound is used in a diverse range of medical fields. Clinical echocardiography (ultrasonic imaging of the heart) has become routine in the diagnosis and management of heart diseases. Moreover the introduction of ultrasound contrast agent (UCA), consisting of microscopic bubbles of gas enclosed in a thin shell, has widely improved the visualization of vasculature, left-right ventricular shunts, tissue perfusion, and delineation of the cavity of the heart, as needed for wall motion analysis.

Originally, ultrasound systems were tuned to receive only fundamental-frequency echoes. Much improvement in the image quality was gained by exploiting the nonlinear responses, i.e. the harmonic frequencies caused by UCA. A popular technique known as power modulation [27] is based on the pressure-dependent amplitude response of microbubbles. Another technique is contrast harmonic imaging (HI), based on the selective imaging of the second harmonic frequency. Advantages of HI are the improved axial and lateral resolution, and a better suppression of image artifacts [28]. Moreover, to reduce the spectral overlap between the fundamental and the second harmonic nonlinear echo, pulse inversion was introduced and shown capable of solving the compromise between the axial resolution and the transmitted bandwidth [29]. Both pulse inversion and power modulation reduce the imaging frame rate by at least a factor two. Moreover, nonlinear ultrasound propagation occurs in tissue that also generates harmonic components, which severely reduce the contrast to tissue levels [30] in second harmonic mode.

Figure 4:9 Photograph of the setup with a block of tissue mimicking material with cavities, and the probe imaging the region.

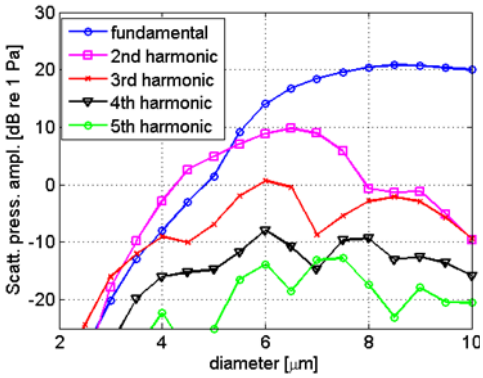

Figure 4:10 Simulated harmonic levels as a function of bubble diameter

Next to the second harmonic imaging, a modality called superharmonic imaging was proposed to use also the third, fourth, and fifth harmonic bands [31], combining them in an attempt to increase the received energy. This technique has recently gained renewed interest in the form of acoustic angiography [32]. The higher harmonics, even more than the second one, feature narrower -6 dB beam widths (increasing lateral resolution), a shorter time pulse (increasing axial resolution), increased reduction of side lobes, and higher contrast to tissue ratio. The resulting images, therefore, are supposed to show more details than those produced by the second harmonic. This was preliminary shown by Bouakaz et al. (2004), who demonstrated that the contrast between UCA and tissue increases as a function of the order of the harmonic frequency.

In order to use this new imaging modality, subsequent versions of an ultrasonic phased array transducer consisting of two interleaved piezoelectric subarrays with different frequency bands were constructed in the early 2000's [31]. The current version of the transducer [33][34] had limited application because of absence of suitable research scanners. This paper investigates the use of the probe for superharmonic detection of UCA, associated to a recent programmable ultrasound system by Ultrasonix (SonixTOUCH). Numerical simulations of the superharmonic behavior of microbubbles in an ultrasound field are also reported.

4b.2. MATERIALS AND METHODS

4b.2.1. Simulation

We used a numerical model defined by Marmottant [35][36] to describe the radial excursion of a microbubble coated with a thin membrane, in an ultrasound field. The radial dynamics were predicted by solving a nonlinear ordinary differential equation in MATLAB code. The backscattered echo of a single, stationary, isolated, spherical, shelled microbubble surrounded by water was then calculated from the radial dynamics [37]. Material parameters for the bubble coating were described in [36], giving a shear viscosity of $\kappa_s = 6\ 10^{-9}$ Pa.s and a shell elasticity of $\chi = 2.5$ N/m. An initial surface tension of $\sigma_0 = \sigma_w/2 = 0.036$ N/m was assumed. Bubbles with a diameter ranging from 2 µm to 10 µm were simulated. Each bubble was excited by a 110 kPa pulse at 1 MHz containing 2 cycles with a cosine envelope. Attenuation of the backscattered echo of 0.5 dB/cm/MHz was taken into account in the back propagation.

4b.2.2. Experiment

We used a dual-frequency phased array probe that was originally developed for cardiac tissue superharmonic imaging. It has interleaved low-frequency transmit elements (N=44, f_c=1 MHz, 50% fractional bandwidth) and high-frequency receive elements (N=44, fc = 3.5MHz, 85% fractional bandwidth). All elements were individually addressed through a custom-programmed commercial ultrasound machine (SonixTOUCH, Ultrasonix with Ultrasonix Texo library) in sector scanning mode. The transmit focus was 6 cm, the echo signals were dynamically focused in receive. Real-time images were produced during the measurements, while beam formed RF data was stored for further offline processing. A tissue mimicking phantom with a UCA-filled cavity of 1 cm diameter was designed to produce realistic tissue and contrast scattering, see Figure 4:9. BR14 (Bracco, Geneva) contrast agent was diluted in a 1:2000 ratio to mimic clinical concentration. The pressure level in the cavity of the

phantom was 110 kPa (MI = 0.11, defined by the ratio of peak negative pressure [MPa] and the square root of the frequency [MHz]) ensuring non-destructivity of UCA. Based on single frames captured with the high-frequency elements, the RF data were filtered around the second, third and fourth harmonic, respectively, with high-order 1.1-MHz wide (at -6dB) zero-phase band pass filters. To quantify the signal level, RMS levels from UCA and tissue areas were obtained from the data. The RMS of the noise was obtained with disabled transmission.

4b.3. RESULTS

4b.3.1. Simulation

Figure 4:10 shows the simulated scatter amplitude as function of the bubble size for the fundamental frequency and its harmonics. For microbubbles larger than 4 µm in diameter, significant signal levels are predicted by the model. Notably, superharmonics are predicted for bubbles larger than 6 µm in diameter, which corresponds to a bubble that is near its resonant regime, in which the oscillation amplitude is significantly large. However, the magnitude varies substantially between the various harmonics. Whereas the second harmonic pressure reaches 3 Pa, the third harmonic reaches 1 Pa at most, and the fourth and fifth harmonic are below 1 Pa. This clearly indicates that the expected superharmonic levels are low, and that only ensembles of microbubbles are expected to be detected. The level of the subsequent harmonics tends to be about 8 dB lower for every harmonic. This 8 dB is caused by about 6 dB lower response of the microbubble itself, and about 2.5 dB lower levels because of the return path attenuation of the echo (0.5 dB/cm/MHz, 5 cm travel path). Since the harmonics caused by the nonlinear propagation in *tissue* are probably even lower [28][30][34], it can be expected that the contrast harmonic signals will decrease less than the tissue harmonic signals, which is beneficial for the contrast detection.

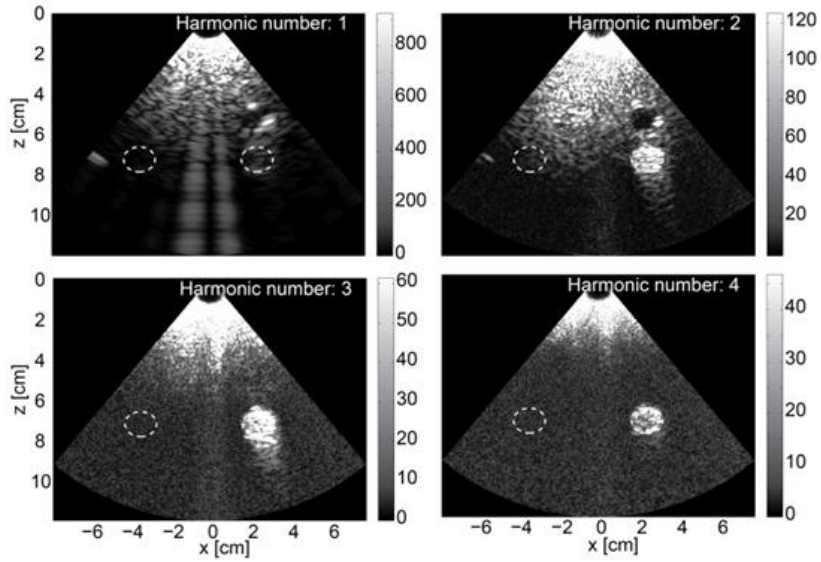

Figure 4:11 Images obtained from the experiment after spectral separation of the subsequent harmonics

4b.3.2. Experiment

Figure 4:11 shows the images of the phantom for fundamental frequency and its harmonics after averaging of 140 consecutive frames. This averaging increased the signal-to-noise ratio in the images, which better revealed the actual tissue levels. If no averaging had been applied, the tissue scattering would be fully shadowed by noise. The water-filled cavity is most clearly visible in the second harmonic image, while the UCA-filled cavity is clearly observed for the fundamental frequency, the second, third and fourth harmonics. The tissue signals were around (for the 2nd harmonic) or below (for 3rd and higher harmonics) the noise floor, indicating that tissue levels were far below the contrast signals.

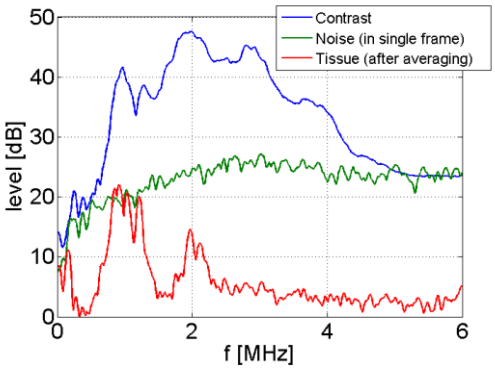

Figure 4:12 Signal spectra in the UCA and tissue regions, and noise levels. The vertical axis is uncalibrated.

This difference is signal levels is further quantified by calculating the signal spectra (Fig. 4) in the UCA-filled cavity, and in a nearby area in the tissue mimicking material. Since the third and higher harmonics of tissue are below the noise floor, only a value of lower CTR bounds could be obtained for the third and fourth harmonics.

The CTR and SNR values, as obtained from an RMS analysis of the signals leading to Figure 4:11, are shown in Table 4-A. Most clearly, the CTR increases for higher harmonic numbers, which is consistent with the qualitative results in Figure 4:11. These values are similar to those so far reported for preliminary contrast superharmonic imaging measurements [31]. The single frame SNR values (in which 'signal' denotes the signal level from the UCA area) are much lower than the CTR, and decrease by about 6 dB with every harmonic number. The trend is consistent with the numerical simulations, although there we found an 8dB decrease for every number. This minor difference may be explained by a possible difference in the real values of the shell parameters as compared to those assumed in the simulation. The lower SNR in the fundamental band (1st harmonic) is caused by a very low sensitivity of the high-frequency elements to this low-frequency component [33].

Table 4-A Measured SNR and CTR values, in dB

Harmonic number	1	2	3	4
SNR	21	23	18	11
CTR	21	36	>>38	>32

To study the destruction of the ultrasound contrast agent, we calculated the signal levels over 140 frames, which corresponds to a 18 s time span. The trend of all signals

is to decrease by about 3dB, except for the 4th harmonic, which has not decreased significantly. This result shows that the UCA can produce significant superharmonic signals over extended period of time and frames.

4b.4. CONCLUSION

The experimental values show the improved CTR achieved by superharmonic imaging compared to second harmonic imaging. However, the reduction of SNR values for the increasing harmonic numbers indicate that noise, and not the tissue signal, is the limiting factor for the UCA detection when using the superharmonics in nondestructive mode. This finding is contrary to second harmonic UCA imaging in practice. As implication, increasing the SNR should be the main focus for optimising superharmonic ultrasound contrast imaging, similar to the work recently activated by Harput et al. for tissue superharmonic imaging [38].

REFERENCES

[1] R.Mallart and M. Fink, Improved imaging rate through simultaneous transmission of several ultrasound beams, Proc. SPIE 1733, pp. 120–130 (1992).

[2] E.D. Light, R.E. Davidsen, J.O. Fiering, T.A. Hruschka, S.W. Smith *Progress in Two Dimensional Arrays for Real Time Volumetric Imaging*, Ultrason. Imag., **20**, pp. 1-15 (1998).

[3] D.P. Shattuck, M.D. Weinshenker, S.W. Smith, O.T. von Ramm *Explososcan: A parallel processing technique for high speed ultraound imaging with linear phased array*, J. Acoust. Soc. Am. 75, pp. 1273–1282 (1984).

[4] S.W. Smith, H.G. Pavy and O.T. von Ramm *High-speed ultrasound volumetric imaging system. I. Transducer design and beam steering*, IEEE Trans.Ultrason. Ferroelect. Freq. Contr., 38, pp. 100–108 (1991).

[5] O.T. von Ramm, S.W. Smith and H.G. Pavy *High-speed ultrasound volumetric imaging system. II. Parallel processing and image display*, IEEE Trans.Ultrason. Ferroelect. Freq. Contr., 38, pp. 109–115 (1991).

[6] G. Montaldo, M. Tanter, J. Bercoff, N. Benech, and M. Fink, *Coherent Plane Wave Compounding for Very High Frame Rate Ultrasonography and Transient Elastography*, IEEE Trans. Ultrason. Ferr. Freq. Control, 56 pp. 489–506 (2009).

[7] L. Tong, H. Gao, H.F. Chio and J. D'hooge *Comparison of Conventional Parallel Beamforming With Plane Wave and Diverging Wave Imaging for CArdiac Applications*: *A Simulation Study*, IEEE Trans. Ultrason. Ferr. Freq. Control, 59 pp. 1654–1663 (2012).

[8] T. Christopher, *Finite amplitude distortion-based inhomogeneous pulse echo ultrasonic imaging*, IEEE Trans. Ultrason. Ferr. Freq. Control, 44 pp. 125–130 (1997).

[9] M.A. Averkiou, D.N. Roundhill, and J.E. Powers, *A new imaging technique based on the nonlinear properties of tissues*, Proc. IEEE Ultrason. Symp.,pp. 1561–1566 (1997).

[10] B. Ward, A.C. Baker and V.F. Humprey, *Nonlinear propagation applied to the improvement of resolution in diagnostic medical ultrasound equipment*, J. Acoust. Soc. Am. 101, pp. 143–154 (1999).

[11] F. Tranquart, N. Grenier, V. Eder and L. Pourcelot, *Clinical use of ultrasound tissue harmonic imaging*, Ultras. Med. Biol. 25, pp. 889–894 (1999).

[12] P.L.M.J. van Neer, M.G. Danilouchkine, M.D. Verweij, L. Demi, M.M. Voormolen, A.F.W. van der Steen and N. de Jong, *Comparison of fundamental,second harmonic, and superharmonic imaging: a simulation study*, J. Acoust. Soc. Am. 130, pp. 3148–57 (2011).

[13] L. Tong, H. Gao, H.F. Choi, and J. Dhooge, *Multi-transmit Beam Forming for Fast Cardiac Imaging*, Proc. IEEE Ultrason. Symp., pp. 140–143 (2011).

[14] A. Drukarev, K. Konstantinides and G. Seroussi*, Beam Transformation Techniques for Ultrasonic Medical Imaging*, IEEE Trans. Ultrason. Ferr. Freq. Control, 40 pp. 717–726 (1993).

[15] M. Alard and R. Lassalle, P*rinciples of modulation and channel coding for digital broadcasting for mobile receivers*, EBU Review, pp. 47–69, August (1987).

[16] M. Russel and G. St□uber, *Terrestrial digital video broadcasting for mobile reception using OFDM*, Wireless Personal Comms, Special Issue Multi-Carrier Comms, 2, no. 1–2, pp. 45–66 (1995).

[17] F. Gran and J.A. Jensen *Frequency Division Transmission Imaging and Synthetic Aperture Reconstruction,* IEEE Trans. Ultrason. Ferr. Freq. Control, 53 pp. 900–911 (2006).

[18] D.Y. Kim, J.C. Lee, S.J. Kwon and T.K. Song, *Ultrasound Second Harmonic Imaging with a Weighted Chirp Signal*, Proc. IEEE Ultrason. Symp., pp.1477–1480 (2001).

[19] J. Song, S. Kim, H.Y. Sohn, T.K. Song, and Y. M. Yoo, *Coded excitation for ultrasound tissue harmonic imaging*, Ultrasonics, 50 pp. 613–619 (2010).

[20] P. Jinhyoung, C. Ruimin, Z. Qifa and K.K Shung, *High frequency, high frame rate pulse inversion chirp coded tissue harmonic imaging*, Proc. IEEE Ultrason. Symp., pp. 2253–2256 (2011).

[21] M. Tanabe, T. Yamamura, K. Okubo, and N. Tagawa, *A novel imaging method of coded THI using multi chirp signals*, Proc. IEEE Ultrason. Symp., pp. 389–392 (2011).

[22] L. Demi, M.D. Verweij and K.W.A. van Dongen, *Parallel Transmit Beamforming using Orthogonal Frequency Division Multiplexing Applied to Harmonic Imaging - A Feasibility Study*, IEEE Trans. Ultrason. Ferr. Freq. Control, 59 pp. 2439–2448 (2012).

[23] P. Tortoli, L. Bassi, E. Boni, A. Dallai, F. Guidi, S. Ricci, *ULA-OP: An Advanced Open Platform for Ultrasound Research,* IEEE Trans. Ultrason. Ferr. Freq. Control, 56 pp. 2207–2216 (2009).

[24] E. Boni, L. Bassi, A. Dallai, F. Guidi, A. Ramalli, S. Ricci, R. Housden, and P. Tortoli*, A Reconfigurable and Programmable FPGA based System for non-standard Ultrasound Methods*, IEEE Trans. Ultrason. Ferr. Freq. Control, 59 pp. 1378–1385 (2012).

[25] T.L. Szabo, *Diagnostic Ultrasound Imaging*, Amsterdam, The Netherlands: Elsevier, 2004, pp. 137–148.
[26] A. L. Thuras, R.T. Jenkins and H.T. O'Neil, *Extraneous frequencies generated in air carrying intense sound waves*, J. Acoust. Soc. Am. 59, pp. 173–180 (1935).
[27] A. Novell, J.-M. Escoffre and A. Bouakaz, Curr. Mol. Imag. **2** (1), 77-88 (2013).
[28] F. A. Duck, Ultras. Med. Biol. **28** (1), 1-18 (2002).
[29] D. H. Simpson, C. T. Chin and P. N. Burns, IEEE Trans. Ultras. Ferr. **46** (2), 372-382 (1999).
[30] H. J. Vos, D. E. Goertz and N. de Jong, J. Acoust. Soc. Am. **127** (3), 1208-1217 (2010).
[31] A. Bouakaz, F. ten Cate and N. de Jong, Phys. Med. Biol. **49** (16), 3515 (2004).
[32] B. D. Lindsey, J. D. Rojas, K. Heath Martin, S. E. Shelton and P. Dayton, IEEE Trans. Ultras. Ferr. **61** (10), 1668-1687 (2014).
[33] P. van Neer, PhD Thesis, Erasmus MC Rotterdam (2010).
[34] G. M. Matte, P. L. Van Neer, M. G. Danilouchkine, J. Huijssen, M. D. Verweij and N. De Jong, IEEE Trans. Ultras. Ferr. **58** (3), 533-546 (2011).
[35] P. Marmottant, S. van der Meer, M. Emmer, M. Versluis, N. De Jong, S. Hilgenfeldt and D. Lohse, J. Acoust. Soc. Am. **118** (6), 3499 - 3505 (2005).
[36] M. Overvelde, V. Garbin, J. Sijl, B. Dollet, N. De Jong, D. Lohse and M. Versluis, Ultras. Med. Biol. **36** (12), 2080-2092 (2010).
[37] J. Sijl, H. J. Vos, T. Rozendal, N. de Jong, D. Lohse and M. Versluis, J. Acoust. Soc. Am. **130** (5), 3271-3281 (2011).
[38] S. Harput, J. McLaughlan, D. M. Cowell and S. Freear, IEEE Trans. Ultras. Ferr. **61** (11), 1802-1814 (2014).

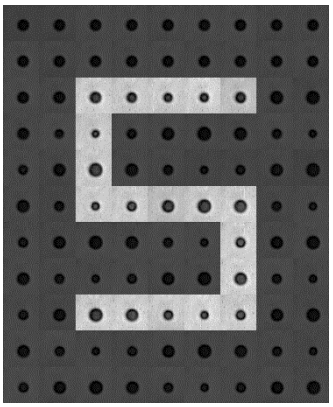

5. Implementation of Arbitrary Contrast imaging Strategies on an US Open Platform

***Abstract*—Comparing the performance of different contrast imaging techniques can be difficult and somewhat confusing, since the tests were typically made using different in vitro setups, contrast agents, ultrasound transducers and systems. In this study, we report on the implementation of arbitrary contrast-pulse-sequences (CPS) in the ULA-OP open ultrasound system. Combined with a home-made phantom, a convenient and consistent evaluation of the main parameters characterizing various techniques is obtained. Several experiments were performed exciting BR14 microbubbles at a dilution between 1/200 and 1/800, with an average MI = 0.1, through 10 different excitation schemes including power modulation, chirp reversal and their combination. Chirp Amplitude Modulation (CAM) and Chirp Reversal Amplitude Modulation (CRAM) showed the best performance with an average CTR of 34 dB.**

Appeared as a proceedings paper for the IEEE Internat. Ultras. Symposium, 2012, by F. Guidi, R. Mori, J. Viti, N. de Jong and P. Tortoli.

5.1. INTRODUCTION

Nowadays the use of Ultrasound Contrast Agents (UCAs) play an important role in clinical diagnosis. Injected UCAs cause the echogenicity of blood to surpass the surrounding tissue's one, extending the possible applications of ultrasound (US) imaging.

Contrast enhanced US imaging methods [1] have proved effective in many new areas, e.g. in the detection and characterization of intra-tumoral vessels in liver, kidney, ovary, pancreas, prostate, breast as well as in the assessment of myocardial perfusion, where slow-moving blood in microvasculature should be distinguished from the surrounding, fast-moving tissue[1]. These innovative imaging methods rely on unique UCAs' physical properties, such as the non-linear behavior and the memory effects, in order to maximize specificity and sensitivity towards UCAs.

This family includes the most commonly used multi-pulse imaging techniques (PM, PI, PMPI), the methods exploiting a coded excitation such as chirp or Golay codes, (i.e. CAM, CPI), and the approaches designed to enhance the bubble memory effects (e.g. Chirp-Reversal (CR), Pulse-Subtraction- Time-Delay (PSTD), Ring-Down (RD), Dual-Frequency (DF) or combinations between CR and PM, PI, PMPI [2][3][4].

Since each method relies on a specific aspect of the UCA response, the performance can differ significantly depending on the investigated area as well as on the set-up used in the tests. A fair comparison of different methods demands that they are implemented in the same machine and evaluated on a realistic phantom. Moreover, an accurate comparison should allow fine tuning of all operating parameters in order to optimize each method's performance.

In this work we compare 10 techniques [5] with a single set-up. We implemented all these techniques in the ULtrasound Advanced Open Platform (ULA-OP) [7] and tested them on the same home-made phantom. The performance of these methods was evaluated in terms of Contrast to Noise Ratio (CNR) and Contrast to Tissue Ratio (CTR).

5.2. EXPERIMENT

5.2.1. The ULA-OP System

ULA-OP controls 64 independent TX/RX channels to drive probes having up to 192 elements. Arbitrary waveform generators (AWGs) are used in transmission, while

each receiver channel uses a low noise, programmable amplifier and a 12-bit 50 MSPS A/D converter. The digital beamformer allows programmable apodization and delays. The system has on board data storage capabilities, with fast data streaming toward high capacity storage units.

We took advantage of the 64 AWGs to transmit the pulse sequences required by the different contrast imaging strategies; the echoes were then acquired and RF beamformed data was saved on a PC to allow further processing and quantitative measurements of the echo data. A special firmware-software combination was designed to allow the user to define arbitrary pulsing schemes and an appropriate echo processing algorithm.

The ULA-OP system was programmed to transmit the different pulse sequences using a 64-element aperture, focused at a depth of 25 mm. Given the large number of different pulses, a complete experiment was divided into 4 phases (A, B, C, D), which were carried out in sequence. In each phase, up to four contrast imaging methods are implemented; the different pulses are transmitted in subsequent pulse repetition intervals (PRI) on the same M-line, then the aperture is shifted and the process repeated. This way, an image of 81 lines is simultaneously obtained for each method. The PRI was fixed at 500 μs. In the receiver, the system uses both dynamic apodization and dynamic focusing in all cases except when chirp signals were transmitted. In this latter case, fixed apodization and focus at 25 mm were used.

Within each phase the US equipment transmits, receives, stores RF data and shows real-time images obtained with standard B-mode and pulse inversion (PI) processing methods. Each phase is concluded with the download of the RF samples of all the received echoes.

5.2.2. Set-up

The measurements were performed on a home-made phantom; a homogeneous brick of tissue mimicking material (TMM) was molded following the guidelines found in [8]. The resulting TMM offers an attenuation of about 0.5 dB/cm/MHz. Furthermore, two separated cylindrical chambers were cast 20 mm apart in the TMM. Each chamber measures about 10 mm in diameter and 80 mm in depth. Before each experiment, both chambers in the TMM were filled with pure demineralized water; a suspension of UCA (BR14, Bracco SpA, Switzerland) was added in one chamber, and continuously stirred using a magnetic stirrer. Once the solution was homogeneously distributed inside the chamber, we performed the complete experiment. Several experiments were carried out at various UCA dilution rates, ranged between 1/800 and 1/200.

A linear 128-element probe (LA332, Esaote, Italy) with a center frequency of 4.6 MHz and a -6 dB relative bandwidth of 102%, was placed against the TMM side and carefully aligned in order to place each hole center at about 25 mm distance from the transducer surface (see Figure 5:1).

The excitation signals consist of sinusoidal pulses of about 1 μs, or of 5 μs chirps between 3-7 MHz with either linearly increasing (up) or decreasing (down) frequency. Table 5-A summarizes the transmission settings used for each contrast imaging strategy. All signals are tapered with a Hanning window, unless otherwise specified. In all conditions two different voltage levels (12 V peak-peak and 6 V peak-peak) were applied. The generated pressure was measured in a water tank with an hydrophone (HGL 0400, Onda, Sunnyvale CA, USA); taking the TMM attenuation into account, the applied mechanical index (MI) was calculated to be no higher than 0.2 in all cases.

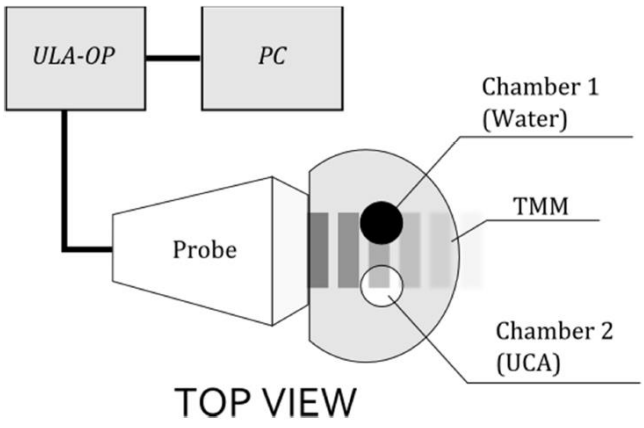

Figure 5:1 Set-up schematic representation

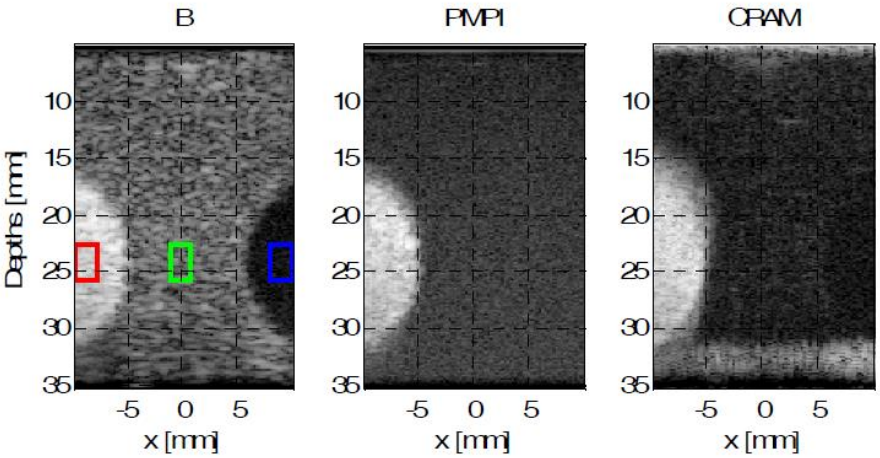

Figure 5:2 Phantom imaging of three different contrast methods, shown wthin a 50 dB dynamic range: B, PMPI, CRAM. (UCA concentration = 1:200).

5.2.3. Processing Methods

The stored RF echoes were post-processed with Matlab® (The MathWorks, Inc., Natick, MA) to implement the required processing.

All echoes were band-pass filtered with a specifically designed FIR filter (300 taps, BW = 2-8 MHz) to remove any contribution outside the transducer bandwidth, and to accurately compensate for its frequency response, thereby equalizing the system's sensitivity; they were then grouped according to the various modes and combined as requested by each mode to compute the resulting RF signals. Differences in RF gain due to the contrast-specific processing were carefully compensated, to enable an absolute comparison between methods; finally the amplitude of the analytic signals was extracted and normalized to obtain the grayscale images.

Quantitative measurements were performed on three different regions of interest (ROI) of equal dimensions. Each ROI was sized to obtain a statistically significant number of samples, and centered at 25 mm depth while laterally positioned on UCA, tissue and water, respectively. From the three ROIs of each image the average amplitudes were extracted; such values were then used to calculate the contrast-to-tissue ratio (CTR) and contrast-to-noise ratio (CNR). The amplitude corresponding to water was considered to be the noise reference level.

5.3. Results and Discussion

As an example, figure 5:2 shows 3 images corresponding to standard B-mode, PMPI and CRAM modes, respectively.

The PMPI image shows an optimal tissue rejection, highlighting the UCAs signal while displaying only background noise everywhere else. The reduced tissue amplitude brings up the near and far wall edges, that appear less sharp due to the out of focus positions combined with the chamber walls curvature and the non-right angle between the US plane and the chamber axis.

The CRAM image on the right has an even lower noise level, due to the greater transmitted energy combined with the subsequent compression. The greater available dynamics make the residual tissue contribution visible again. The chamber walls are now completely blurred; this is a consequence of the fixed receive focus adopted to maintain a good correlation between the received signal and the compression filter. At the bottom of the image, the light noise band is caused by the tail of the convolution between the signal and the compression mask.

Figure 3 reports the average spectra computed over the three ROIs highlighted in figure 2. The spectrum from the water area in the B-mode image sets the noise reference level while the spectra from tissue and UCA show the corresponding response at the selected ROIs: the UCA spectrum appears wider than the tissue spectrum due to the nonlinear response of the UCA.

Table 5-A Configurations used for transmission

Phase	Modes	Tx Pulses				
		ID	***Length [cycles]***	***Frequency [MHz]***	***Amplitude [Vpp]***	***Notes***
A	Power modulation (PM)	A1	4	3.5	6	
		A2	4	3.5	12	
		A3	4	3.5	6	
	Pulse inversion (PI)	A4	4	3.5	12	
		A5	4	3.5	-12[a]	
	Power modulation combined with pulse inversion (PMPI)	A6	4	3.5	6	
		A7	4	3.5	-12[a]	
		A8	4	3.5	6	
B	Subharmonic imaging (SH)	B1	20	6	12	Rect window
	Chirp reversal (CR)	B2	5 µs[b]	3-7 (up)	12	Linear chirps, 20% tukey window tapering.
		B3	5 µs[b]	3-7 (down)	12	
	Chirp amplitude modulation (CAM)	B4	5 µs[b]	3-7 (up)	6	Linear chirps, 20% tukey window tapering.
		B5	5 µs[b]	3-7 (up)	12	
		B6	5 µs[b]	3-7 (up)	6	
	Chirp reversal amplitude modulation (CRAM)	B7	5 µs[b]	3-7 (up)	6	Linear chirps, 20% tukey window tapering.
		B8	5 µs[b]	3-7 (down)	12	
		B9	5 µs[b]	3-7 (up)	6	
C	Pulse subtraction time delay (PSTD)	C1	4	4	12	Rectangular window. Second pulse is delayed by 1 µs.
		C2	4	4	12	
		C3	8	4	12	
	Dual-frequency (DF)	C4	4	3	6	Pulse C6 corresponds to the sum of C4 and C5 pulses.
		C5	8	6	6	
		C6	1.33 µs[b]	3+6	12	
D	Ring-down (RD)	D1	***s1:*** 2.5 µs[b] ***s2:*** 0.5 µs[b]	***s1:*** 3 ***s2:*** 6.5	***s1:*** 12 ***s2:*** 12	Each D1,D2 pulse is composed of two sinusoids [s1; s2] fired one after another in the same PRI.
		D2	***s1:*** 2.5 µs[b] ***s2:*** 0.5 µs[b]	***s1:*** 3 ***s2:*** 6.5	***s1:*** -12[a] ***s2:*** 12	
	Standard B-mode (B)	--	Derived from A2			
	Chirp based B-mode (CB)	--	Derived from B2			
	Loss-of-correlation (LOC)	--	Derived from A1 and A3			

a Negative amplitude indicates a 180 degrees phase-shift in the transmitted pulse.
b An exact number of cycles cannot be measured in this case, time duration is reported instead.

The PMPI spectrum of the tissue is indistinguishable from the water spectrum, remarking an effective tissue cancellation. The UCA spectrum is attenuated around the first harmonic and a small peak on the second harmonic is barely seen.

The CRAM spectra show a strong attenuation of the white noise and a good tissue attenuation except for a residual contribute at the highest frequencies, that justifies the low-level tissue still visible in the image. All CRAM spectra cover, as expected, the full transmitted chirp bandwidth and vanishes elsewhere due to the compression filter.

Table 5-B reports the average amplitudes computed inside each ROI. To simplify the comparison between short and long TX pulses processing, an appropriate

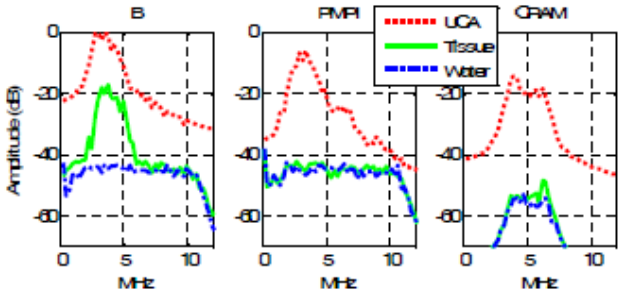

Figure 5:3 Average spectra computed over the 3 ROI for the contrast methods shown in figure 2, normalized to the absolute maximum amplitude. In these graph the transducer frequency compensation has been switched off.

normalization factor has been adopted. From these values, the contrast-to-tissue ratio (CTR) and contrast-to-noise ratio (SNR) parameters are derived allowing a comparison between methods.

The amplitude computed in water is about the same for all methods based on the transmission of short pulses; only SH and RD show values slightly smaller due to the filter bandwidth used to remove unwanted components. Instead all methods based on long chirp TX show amplitudes at least 15 dB lower than other cases. This confirms the characteristics of the chirp pulse that, transmitting more energy than standard short pulses, is able to enhance the SNR, as reported in the table.

Three modes (PM, PI, PMPI) behave in a similar way, expressing a similar CTR, always limited by noise level. With this specific home-made phantom and the adopted TX frequencies, PI shows the poorest performance, due to the second harmonic strong attenuation in the TMM.

Chirp contrast methods CR, CAM and their combination, CRAM, show the same noise level as well as about the same tissue amplitude. The UCA's amplitude rises about 4 dB in CAM and CRAM, causing a corresponding CTR enhancement (up to 34 dB), mainly due to the double amplitude pulse in the TX sequences producing higher nonlinear components from microbubbles.

SH, PSTD, DF and RD show an effective tissue cancellation but poor residual UCA amplitudes. These methods are still not optimized in terms of pulse length, windowing and temporal and frequency distance between pulses.

The last row in the table reports the loss-of-correlation (LOC) image parameter, computed subtracting the echoes produced by 2 identical TX pulses, 3 PRI apart (equal

to the worst case spacing that occurs in the 3 pulses length methods). Both CTR and CNR computed for this image demonstrate that subsequent echoes are substantially identical, hence the UCAs are not destroyed in a significant amount (i.e. the pressure is sufficiently low) nor an excessive stirring speed was used.

All results in table 5-B show a standard deviation below 2 dB. By using different UCA concentrations in the 1/200-1/800 range, such values were confirmed within 3 dB; the most evident difference is the higher attenuation in the lower part of chamber 2 when a higher concentration is used.

Table 5-B ROIs average amplitude values and performance parameters

Modes	UCA	Tissue	Water	CTR	CNR
B	70.8	51.5	36.7	19.3	34.1
CB	65.9	53.8	20.5	12.1	45.4
PM	63.8	36.3	36.0	27.5	27.7
PI	57.6	37.2	36.9	20.4	20.7
PMPI	64.3	37.8	37.2	26.5	27.1
SH	62.1	40.1	33.2	22.0	28.9
CR	51.9	22.2	19.1	29.7	32.8
CAM	55.0	21.2	19.6	33.8	35.4
CRAM	56.5	22.5	20.0	34.0	36.5
PSTD	62.0	36.7	36.3	25.4	25.7
DF	57.8	36.2	35.8	21.6	22.0
RD	50.4	33.5	33.9	16.9	16.5
LOC	37.4	36.2	35.9	1.1	1.5

All values are in dB, UCA concentration = 1:200.

5.4. CONCLUSIONS

This work has reported a fair comparison of different contrast imaging techniques, all implemented in ULA-OP equipped with suitable software. By exploiting the flexibility of the system and the on-board arbitrary waveform generators, virtually any new transmission strategy can be implemented. Within the constraints of our set-up, the PMPI produced the best results among the standard CPS techniques; excellent performance came from chirp techniques, with a CTR improvement in the CRAM method of 22 dB over the initial chirp based image. All chirp methods were hampered by the static focalization, adopted to maintain a good matching between the used compressor and the received echo. We are currently extending the TX schemes and the post processing algorithms in order to increase the performance. We are also

translating some of the tested methods in real-time in order to enable the in-vivo validations.

REFERENCES

[1] E. Quaia, *Contrast-specific ultrasound techniques*, Radiol med 2007,DOI: 10.1007/s11547-007-0157-1

[2] Crocco, M.; Pellegretti, P.; Sciallero, C.; Trucco, A.; *Combining multi-pulse excitation and chirp coding in contrast enhanced echographic imaging*, Imaging Systems and Techniques, 2008. IST 2008. IEEE International Workshop on , vol., no., pp.45-49, 10-12 Sept. 2008. doi: 10.1109/IST.2008.4659938.

[3] Novell, A.; Der Meer, S.; Versluis, M.; Jong, N.; Bouakaz, A.; *Contrast agent response to chirp reversal: simulations, optical observations, and acoustical verification*, Ultrasonics, Ferroelectrics and Frequency Control, IEEE Transactions on , vol.56, no.6, pp.1199-1206, June 2009; doi: 10.1109/TUFFC.2009.1161

[4] Novell, Anthony; Bouakaz, Ayache; *Chirp reversal power modulation contrast imaging,* Ultrasonics Symposium (IUS), 2011 IEEE International , vol., no., pp.632-635, 18-21 Oct. 2011, doi: 10.1109/ULTSYM.2011.0153

[5] Wilson SR, Greenbaum LD, Goldberg BB., *Contrast-enhanced ultrasound: what is the evidence and what are the obstacles?*, AJR Am J Roentgenol. 2009 Jul;193(1):55-60.

[6] Renaud et al., *In vitro comparative study of the performance of pulse sequences for ultrasound contrast imaging of the carotid artery*, IEEE International Ultrasonic Symposium 2011

[7] E Boni, L Bassi, A Dallai, F Guidi, A Ramalli, S Ricci, J Housden, P Tortoli, *A reconfigurable and programmable FPGA-based system for nonstandard ultrasound methods*, IEEE Trans Ultrason Ferroelectr Freq Control, 2012, V. 59(7), pp. 1378 – 1385, doi: 10.1109/TUFFC.2012.2338.

[8] Teirlink, C.J.P.M., Bezemer, R.A., Kollmann, C., Lubbers, J., Hoskins, P.R., Fish, P. Fredfeldt, K.E., Schaarschmidt, U.G. (1998) *Development of an Example Flow Test Object and Comparison of Five of these Test Objects, Constructed in Various Laboratories*, Ultrasonics, v. 36, p. 653-660.

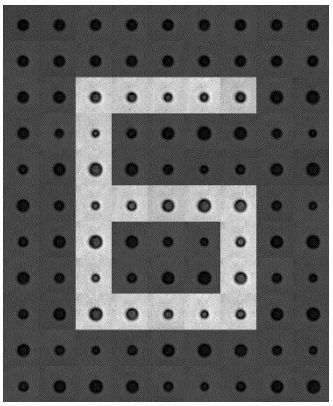

6. Detection of Contrast Agents: Plane Wave vs Focused Transmission

***Abstract*— Ultrasound contrast agent (UCA) imaging provides a cost-effective diagnostic tool to assess tissue perfusion and vascular pathologies. However, excessive transmission levels may negatively impact both uniform diffusion and survival rates of contrast agents, limiting their density and thus their echogenicity. Contrast detection methods with both high sensitivity and low contrast destruction rate are thus essential to maintain diagnostic capabilities. Plane wave transmission with high number of compounding angles has been suggested to produce good quality images at pressure levels that do not destroy UCA. In this paper, we performed a quantitative evaluation of detection efficacy of flowing UCA with either traditional focused scanning or ultrafast plane wave imaging. Amplitude modulation at nondestructive pressure levels was implemented in the ULA-OP ultrasound research platform. The influence of the number of compounding angles, peak-negative pressure and flow speed on the final image quality was investigated. Results show that the images obtained by compounding multiple angled plane waves offer a greater contrast (up to 12 dB increase) with respect to Focused amplitude modulation. This increase is attributed mainly to noise reduction caused by the coherent summation in the compounding step. Additionally, we show that highly sensitive detection is already achieved with a limited compounding number (N<16), thus suggesting the feasibility of continuous contrast monitoring at high frame rate. This capability is essential to properly detect contrast agents flowing at high speed, as an excessive angle compounding is shown to be destructive for the contrast signal, as the UCA motion quickly causes loss of correlation between consecutive echoes.**

Accepted for publication in IEEE Trans. On Ultras. Ferroelec. And Freq. Control, by J.Viti, F. Guidi, H.J. Vos, N. de Jong and P. Tortoli; © IEEE 2015.

6.1. INTRODUCTION

In the eighties, it was believed that ultrasound contrast agents (UCA) could be sufficiently detected and imaged with the conventional imaging methods nowadays referred to as fundamental imaging. Later it was acknowledged that newer imaging techniques based on specific properties of the UCA proved to be more sensitive. In general, these new characteristics involve non-linear and transient characteristics of contrast agents that appear at the high end of the diagnostic acoustic intensity [1]. Imaging modalities used today for UCA detection are, besides fundamental imaging, harmonic imaging, most notably second harmonic imaging, and subharmonic imaging; multi-pulse imaging, such as pulse-inversion; and Doppler-based methods, such as power Doppler. Some advanced modalities may combine two or more strategies to improve the performance, as is the case in harmonic power Doppler and pulse inversion Doppler. The methods are either destructive (high Mechanical Index-MI) or non-destructive (low MI). The destructive method results in a very good contrast to tissue ratio, but requires triggered imaging and is therefore not often used. So, imaging of ultrasound contrast agents (UCA) is currently performed at a low mechanical index (MI) [2].

Measuring the perfusion of organs with UCA sensitive detection methods is crucial since the blood volume relative to the tissue volume can be very small. For, e.g., healthy myocardium the blood volume is 6-8% and for ischemic tissue it can be as low as 1% or less. Besides being present in the microcirculation in small quantities, these microbubbles are also moving slowly. Therefore, low MI is essential to prevent the destruction of the limited amount of UCA flowing in such small vessels. On the other end, limiting the MI begets a situation where the microbubble echoes might be hard to identify against the background noise. Although the second harmonic responses of both UCA and tissue are quadratic related to the applied acoustic pressure [2], the magnitude of the MI still plays a role in the discrimination of the UCA and tissue For example, in [3] differences in image contrast at different MIs were reported. Various detection strategies were proposed to discriminate between the UCA and the surrounding tissue. A largely used technique, commonly referred to as either power or amplitude modulation (AM) [4],[5], consists of transmitting into the medium at least two consecutive pulses using different acoustic levels; then rescaling and adding the echoes together to enhance the nonlinear response of UCA while suppressing the linear echoes coming from tissue. Another technique is called Pulse inversion [6]. In pulse inversion imaging, a sequence of two ultrasound waves is transmitted into tissue. The second wave is transmitted after a suitable delay and is an inverted replica of the

first wave. For a linear medium the response of the second wave is an inverted copy of the response from the first wave, and the sum of the two responses is zero. For a non-linear system, e.g. gas bubbles, the response will not be an inverted copy. Both methods result in a reduced frame rate because of the requirement of transmitting an ensemble of pulses along each scan line. The combination of amplitude modulation and pulse inversion is nowadays considered as the most sensitive method for contrast detection [7] and is implemented in many commercial echo-machines having contrast package on board.

In more recent years, plane wave transmission was proposed as a method to combine high frame rate capabilities and non-destructive UCA detection [8]. Ultrafast imaging methods, such as plane wave, allow for a dense time sampling of the whole scan plane, thus preserving flow and motion information. Although plane wave imaging is typically plagued by a low lateral resolution, the coherent summation of multiple angled plane waves was shown as a viable method to simultaneously improve lateral resolution and SNR in the final image [9], whilst partially sacrificing the frame rate improvement with respect to traditional focused transmission. Additionally, the benefit of combining ultrafast imaging together with UCA is actively being investigated, with recent work showing the potential of super resolution imaging [10] and the advantage of having simultaneous Doppler and contrast imaging [11][12]. However, the benefits of using plane wave for regular contrast imaging remain not completely explored, nor is the influence of flow velocity on the compounding.

In this paper, we compare two methods for UCA detection with amplitude modulation; 1) Line by line scanning (Focused) and 2) Plane-wave scanning (Planewave). The influence of peak negative pressure (PNP), flow speed and number of coherently compounded angles on the final UCA signal intensity, image noise, and contrast-to-background ratio (CBR) is investigated.

6.2. METHODS

The study was performed with the peripheral vascular flow phantom model 524 (ATS Laboratories Inc, Bridgeport, CT). The phantom included a 6 mm diameter wall-less vessel surrounded by a tissue mimicking material (TMM). The attenuation was 0.5 dB/cm/MHz at 3.5 MHz, similar to the attenuation usually assumed for biological soft tissue. The wall-less vessel containing the flowing UCA was located at a depth of 25 mm from the surface. An upper reservoir was filled with a 1:2000 dilution of BR-14 UCA (Bracco Research S. A., Geneva, Switzerland) in demineralized water; this dilution was continuously stirred and fed via a gravity drop through the vessel. A valve, placed

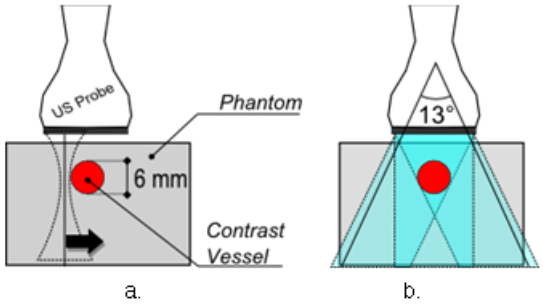

Figure 6:1 Schematic drawing of the flow phantom imaging procedure when focused ultrasound (a), or angled plane wave ultrasound (b) is applied.

immediately after the output of the phantom, was used to regulate the flow velocity while a peristaltic pump pushed the fluid back into the upper reservoir. The average flow speed in the tubing was estimated by measuring the time necessary for a predetermined volume of fluid to flow through the system. In our experiments we tested two mean flow velocities of 20 mm/s and 55 mm/s and three transmit pressures (70 kPa, 110 kPa or 140 kPa).

The ultrasound data acquisition was performed with the ULA-OP system [13]. This system is a 64-channel research platform connected to a PC for control, real-time feedback, and data storage. User-programmed complex sequences are supported, enabling extreme flexibility in both transmit and receive strategies. Access to raw RF data is provided, with the system being able to natively store up to 1 GiB of radiofrequency (RF) raw channel data without the need for additional equipment. ULA-OP was used to drive an LA332 linear array probe (Esaote S.p.A., Genoa, Italy) with 4.6 MHz central frequency and 104% fractional bandwidth (full width at -6 dB).

All data were recorded in a cross-sectional view (Figure 6:1). In Focused mode, the phantom was scanned line by line having 64 lines per frame (Figure 6:1(a)). In Planewave, a programmable odd number N of angled plane waves was used, N ranging from 1 to 63. For any N>1, plane waves were transmitted to cover a 13 degrees sector angle, corresponding to an electronic steering from -6.5° to +6.5° (see Figure 6:1(b)). In both Focused and Planewave cases, a 3-pulse AM packet consisted of half-amplitude (**H**) and full amplitude (**F**) pulses in **H-F-H** sequence. Notably, as the ULA-OP system contains per-channel arbitrary waveform generators, we were able to perform true AM by accurately changing the output waveform amplitude, as typically done in single-element transducer studies [5], rather than using a subset of the active aperture to modulate the output acoustic power, as is commonly implemented in clinical US scanners [4]. The echo signals of each AM packet were processed into a

single contrast-enhanced AM line (Focused) or an entire angled frame (Planewave) by subtracting the RF echoes of the two **H** pulses from the echo of the single **F** pulse.

The transmit pulses contained 4 cycles at 3.5 MHz with a Gaussian envelope. The pulse repetition frequency (PRF) was fixed at 6 kHz. Considering the 3-pulse AM packets, the final frame rate for a 64-line Focused image was thus 31 frames/s. For Planewave, the frame rate was inversely related to N, with a maximum of 2000 frames/s for N=1 and a minimum of 31 frames/s for N=63. For each possible combination of transmission (TX) pressure (**F:** 70 kPa, 110 kPa or 140 kPa, peak-negative) and flow velocity (20 mm/s or 55 mm/s), a full measurement set was carried out. One measurement set contained transmission of Focused and Planewave with N = 1, 3, 9, 15, 31, 63, and was completed in about 5 minutes. Each measurement set was replicated over different days to test the reproducibility of the measurements.

In Focused mode, the transmission wave was focused at the center of the vessel, at a depth of 25 mm. The peak-negative pressure for both focused and plane wave TX was kept equal at the contrast agent's location. This was carefully checked by hydrophone measurements in water at 25 mm depth. The PNP generated by the full-amplitude pulses ranged between 70 kPa and 140 kPa, which is within reasonable limits to avoid UCA destruction [14][15].

The raw RF channel data were processed offline to reconstruct 64-line images. First, raw channel data was beamformed by a classic delay and sum algorithm; a bandpass filter with -6 dB cutoff at 1 and 13 MHz was then applied to the beamformed echo signals to remove the DC component and to limit the wideband noise. For angled plane waves, the beamformed RF images for each TX angle were coherently averaged. AM processing was performed by adding the two RF **H** traces and a sign-inverted **F** trace. Finally, baseband demodulation and lowpass filtering (cutoff: 6 MHz) was performed to produce the final contrast image frames.

The frames were analyzed to obtain the contrast-to-background ratio (CBR), defined by the ratio of the root mean square (RMS) values in a location inside and outside the vessel region, respectively. Two square regions of interest (ROIs), each covering a 9 mm^2 area, were thus selected in each B-Mode image, using careful positioning to ensure that one ROI was located entirely within the UCA-carrying vessel and the other was located entirely on the TMM, as shown in Figure 6:2(a). Note that the two ROIs were not set at the same depth just to avoid any interference from the UCA signal when estimating the background intensity; such interference can clearly be seen e.g. in Figure 6:2(b), where no plane wave compounding leads to low lateral resolution and visible artifacts. After AM processing, a residual background signal persists, which is a combination of electronic noise and residual echoes from the TMM.

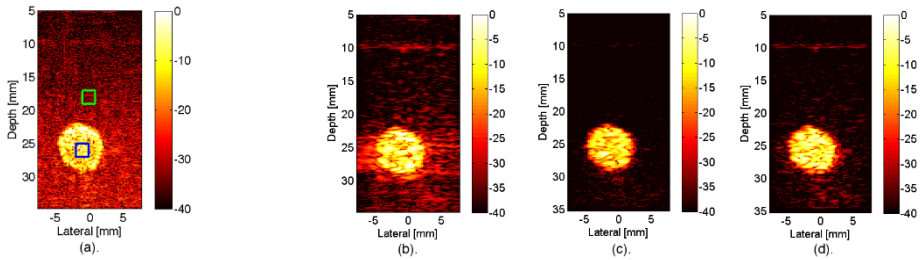

Figure 6:2 Left to right: Focused AM (a) ; Compounded Planewave AM with increasing number of angles (N = 1; 15; 63, respectively). Fig. (a) also shows the ROIs for evaluation of UCA (blue) and background (green) signal intensity.

For this reason, we made no explicit distinction between contrast-to-tissue ratio (CTR) and contrast-to-noise ratio (CNR); if the residual tissue signal (after AM) is significantly higher than the background noise, the CBR becomes effectively equivalent to the CTR; vice versa, if the background noise is dominant, the CBR is ideally equal to the CNR.

6.3. RESULTS

Figure 6:2 shows, as an example, the B-Mode AM images obtained at 140 kPa PNP and 20 mm/s flow speed. The leftmost image is a Focused-AM frame. The other frames, from left to right, are Planewave frames obtained with N=1 (no compounding), N=15 and N=63 compounding angles, respectively. Each frame has a dynamic range of 40 dB, normalized to the maximum signal amplitude in the UCA region. The Focused image shows, as expected, good lateral resolution in the focal area, resulting in sharp and well-defined borders of the UCA-filled vessel; however, the image is affected by a noticeable background signal. In the Planewave image at N=1, the UCA area is clearly detected, but the signal leaks to the surrounding tissue. This is caused by the poorer lateral resolution and larger sidelobe levels in plane wave imaging [9]. The background signal levels are similar to those in the Focused AM frame. As expected from frame compounding theory [9], using multi-angle (N>1) Planewave simultaneously restores an acceptable lateral resolution while yielding an improved image contrast against the background. However, the background suppression in Figure 6:2(c) (N=15) is better than in Figure 6:2(d) (N=63). The reason for this is hypothesized to be an increased de-correlation of UCA signals caused by the flow for an increasing number of compounding frames. This hypothesis is further discussed in Section 6.4.

The calculated CBR values for all of the measurement configurations are reported in Figure 6:3. The highest CBR values are in the range 30 – 36 dB, depending on the experimental conditions. It is worth observing that single plane wave (N=1) and Focused transmissions present similar CBRs, consistently matched within 1 dB. This can be explained by the observation that, for both images, every pixel in the image is

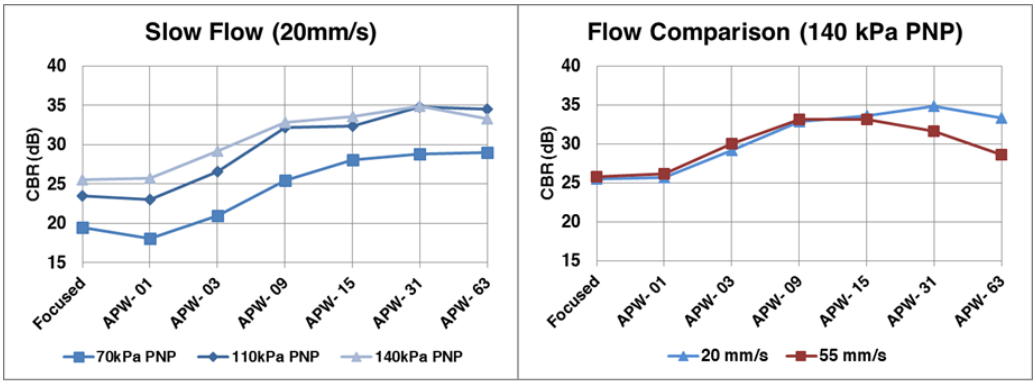

Figure 6:3 Contrast-to-background ratio trends for different N: (a) 70, 112 and 140 kPa PNPs were applied, and an average flow speed of 20mm/s was maintained; (b) 140 kPa PNP was maintained and either 20 mm/s or 55 mm/s average flow speed were enforced.

reconstructed from a single AM packet. Therefore, the SNR can be expected similar. Using multi-angle compounding in Planewave-AM the CBR values become higher. At 20 mm/s mean velocity, also referred to as slow-flow in the present work, the CBR increases significantly with N up to 9 and 15 and less markedly at higher N values (31 and 63). The peak CBR is reached for N=63 at 70 kPa and 110 kPa PNP (with about 12 dB improvement compared to Focused) and at N=31 when 140 kPa PNP pulses are employed (with about 10 dB improvement compared to Focused). This is consistent with a previous study [16], which reports an improvement of up to 11 dB when using plane waves rather than focused transmission for PNP below 200 kPa.

Conversely, when a higher (55 mm/s) mean flow speed is imposed (fast-flow), the best CBR is reached for a limited number of angles, typically between 9 and 15; using larger numbers of angles results in a progressive reduction of CBR, albeit, even at N=63, Planewave was still found to perform better than Focused-AM in terms of CBR. Typically, in fast-flow conditions, Planewave surpasses Focused performance by 6 dB for N=9 and by 3 dB for N=63.

Repeated measures over three days using the same phantom confirmed these results, with the final CBR varied within ±1dB between different measurements sets.

Figure 6:4 shows the signal power spectral densities (PSDs) calculated for the UCA (Figure 6:4(a)) and the background (Figure 6:4(b)) ROIs for Focused and Planewave measurements, at slow flow. In all UCA spectra (top), the 3.5 MHz component is clearly dominant. No separate peak is visible at 7 MHz, indicating no significant second harmonic content after AM processing at these pressure levels. The background PSD for Focused is flat within the bandwidth of interest, indicating that white noise

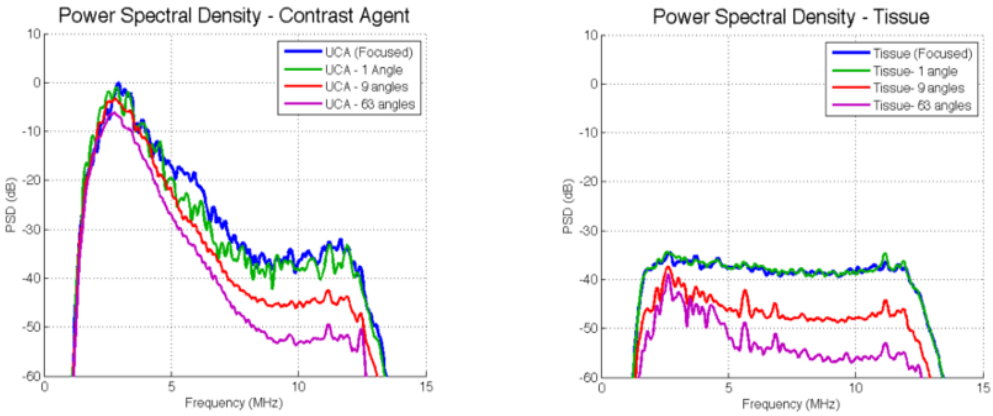

(a). (b).

Figure 6:4 Power spectral densities of signals from UCA (left) and tissue (right) after AM processing, at 20 mm/s mean flow speed. Focused and Planewave N=1 PSD are well-matched. Increasing N in Planewave reduces the broadband noise contribution at high frequencies.

dominates the background signals over residual tissue signal. The peak-UCA signals are an order of 30 to 40 dB above the noise levels, consistent with the values in Figure 6:3, which are based on the time-domain RMS values estimated after IQ demodulation and bandpass filtering. The UCA signal for N=1 matches well with the Focused (see Figure 6:4(a)), which is again explained by the fact that every pixel is reconstructed from a single AM packet only. The intensity of the UCA signal at 3.5 MHz, as well the noise level above 7 MHz, decrease with increasing N, although the overall shape of the PSD is preserved; when the maximum N=63 is used, the UCA loss is about 6 dB at 3.5 MHz compared to that of N=1.

Figure 6:4(b) shows the influence of N on the background signal: the background intensity decreases with increasing N; furthermore, the shape of the PSD changes: a background component located around the fundamental frequency becomes apparent for large N at a level of -40 dB. This is a residual tissue signal after AM processing which cannot be removed by compounding. Again, the background PSDs for Focused and Planewave with N=1 (Figure 6:4(b)) match consistently within 1 dB.

6.4. DISCUSSION

Figures 6:2 to 6:4 show that the contrast-to-background ratio (CBR) increases by compounding angled Planewave AM frames, and that compounding leads to higher CBR than Focused transmission. Furthermore, coherent compounding suppresses the incoherent system noise while maintaining the coherent tissue and UCA scattering. Following this interpretation, the CBR improvement is mainly due to an improved SNR.

Although time averages or angle compounding can have a beneficial effect on the noise component of the background signal, they do not affect the residual tissue component after AM processing. The AM processing originates from the echoes of stationary scatterers and is therefore highly coherent. This explains the residual signal at 3.5 MHz in Figure 6:4(b).

The UCA motion leads to loss of signal correlation between compounding sub-frames that are distant in time. The assumption of stationary scatterers (which permits coherent compounding) is increasingly violated for larger number of compounding frames, and for higher flow velocities. This effect is seen in Figure 6:3(b) in which the CBR for a fast flow is lower than for a slow flow when N>15; in fact, the CBR for N>15 and fast flow actually decreases with N. In such a case, the fast flow UCA signal becomes highly de-correlated before all the angles are acquired, resulting in a lower UCA intensity in the final frame compared to the slow flow situation, while the background signal remains the same.

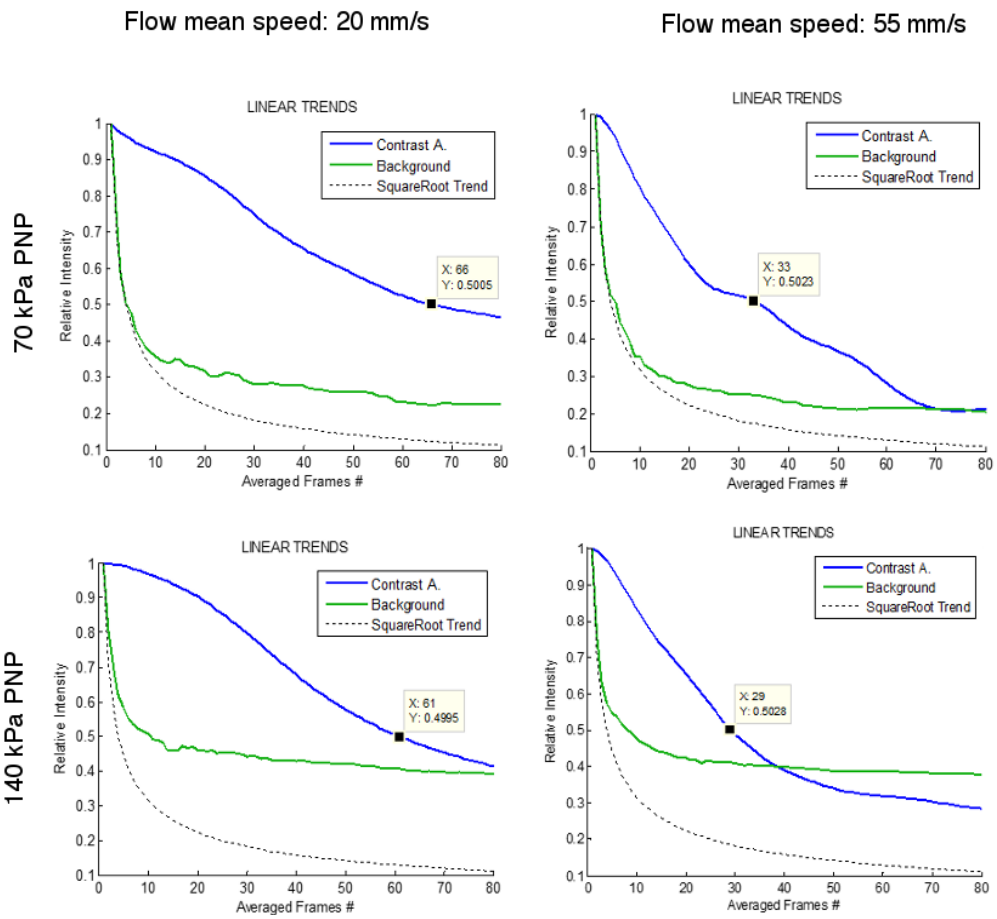

Figure 6:5 Relative intensity of UCA and background when multiple planewave (N=1) frames are averaged. The number of averaged frames at which the contrast relative intensity is halved is highlighted. The 2x2 cartesian product set is shown here for two different P

The chosen number of angles depends heavily on the clinical application. E.g. for bubble tracking in the left ventricle, where high velocities are present (up to 1 m/s) the number of angles should be very low, or even 1. For slow flow and low velocities, e.g. in the capillaries (< 1 mm/s), the number of angles can be even as high as 63. For intermediate velocities like in the veins (1-10 cm/s), the number of angles could be around 10-20 without getting significant de-correlation of the received signals during the acquisition.

The noise reduction, and UCA de-correlation effect in flowing UCA is further confirmed by a separate experiment, in which we only used single Planewave (N=1) packets at 6 kHz PRF (0.5 ms AM frame interval). The AM frames were here cumulatively averaged. Figure 6:5 shows the relative amplitudes of the UCA signal and

the background signal as function of the cumulative average. In all cases, the background signal initially follows a square root trend as a function of the number of averaged frames, which is consistent with averaging incoherent noise. This again indicates that generally, in a single AM frame, random noise dominates the background signal. With increasing averaging number, the background signal plateaus and is dominated by the residual tissue component. Notably, when a higher PNP is used, the residual tissue signal is also larger, and starts to be a dominant factor in the background signal after about 10 averaged frames.

UCA motion leads to loss of coherence of the UCA signal over time, and the flow speed becomes a critical parameter. This is shown in Figure 6:5. When a slow flow was used, about 60 frames could be averaged before the relative UCA intensity decreases to 0.5; when a fast flow was used, about 30 frames only could be averaged. This confirms that the UCA signal coherence across consecutive frames is inversely proportional to the flow speed, and confirms that excessive compounding with a fast flow can be detrimental to performance. The order of magnitude of the time constant (30 ms for slow flow, 15 ms for fast flow) can be checked by geometrical considerations. The -6 dB beam width in the elevation direction is on the order of 1.4 mm (f= 3.5 MHz, depth = 25 mm, element elevation width = 8 mm). For slow flow, the peak velocity is 40 mm/s (20 mm/s average velocity, parabolic flow profile). Thus, it takes approximately 35 ms for the UCA to cross the beam in slow flow, and approximately 13 ms in the fast flow case. This would correspond to 70 frames and 26 frames, respectively, at the AM frame rate of 2000 frames/s. These values are within reasonable agreement, showing that the de-correlation of the UCA signal observed in Figure 6:5 can at least be partly explained by the flow itself.

Looking at the connection between flow and microbubble de-correlation in Figure 6:5 it is also possible to infer the influence of destruction/ultrasound-induced deflation of the UCA microbubbles itself [16][18]. If microbubble destruction were the main cause of signal loss in Figure 6:5, then the signal loss would be independent of flow velocity, or would even produce the opposite behavior than that observed in Figure 6:5. The latter can be hypothesized since a faster flow would provide more inflow of non-destroyed UCA, and thus the signal would persist longer. The observed behavior may instead indicate that destruction/deterioration has a negligible influence. Nonetheless, an experiment in which the flow is fully halted should be conducted to actually investigate destruction rates at the current transmit conditions.

The presence of AM signal is in itself an indication of nonlinear behavior. The PSDs shown in Figure 6:4(a) indicate that the largest contribution to the UCA signal comes from the frequency components located in the fundamental frequency band, while the second harmonic content is negligible after AM processing. This is contrary to the

pulse inversion detection scheme which relies on nonlinear UCA scattering in the second harmonic band. A non-linear response in the fundamental frequency band was previously attributed to a thresholding effect [19][20][21]. The theory [20][21] and experimental measurements [19][21] showed that for specific combinations of size and driving pressure, microbubbles can have a pressure threshold below which they do not respond to the excitation, while above this threshold they do respond. We carried out numerical simulations to investigate the microbubble response to the experimental ultrasound conditions, see Appendix A in this chapter. These simulations indicated that above a diameter of 2 μm the microbubbles do show a response in the fundamental frequency band after AM processing. The second harmonic components are predicted to be small for these size ranges and driving pressures, which is consistent with the measurements. This all implies that the receive frequency band can be kept equal to the transmit band, which relaxes the bandwidth requirements compared to detection schemes that rely on second harmonic frequency detection.

Flow can also result in de-correlation of UCA signals within the AM packet leading to a residual signal after AM processing [22]. To test the relative contribution of nonlinear UCA responses and de-correlation within the AM packet we further analyzed the fast flow, 140 kPa Planewave data for N=1, described above. Figure 6:6 compares the PSDs obtained by different processing of the **H-F-H** packet data. Figure 6:6(a) shows the spectra of a full-amplitude frame (**F**), which act as reference. Figure 6:6(b) shows the spectra after AM processing (**2H – F**) in a single frame. Figure 6:6(c) shows the spectra obtained by taking the difference of two consecutive **F** frames ($\mathbf{F_{i+1} - F_i}$), recorded at 0.5 ms time interval. In all three cases, a significant fraction of the UCA signal power is located around the TX frequency of 3.5 MHz. In Figure 6:6(a), the regular pulse-echo PSDs present a similar shape for UCA and tissue echoes. The tissue echo signal drops below the noise level (at -40 dB) for frequencies above 5 MHz, whereas the UCA spectral peak is wider, since it originates from the contributions of a population of bubbles. As bubbles typically exhibit a resonant behavior in response to ultrasound 0, the collective contribution of the investigated population results in a spectral broadening for the UCA signal, as multiple differently-sized bubbles are driven to resonance.

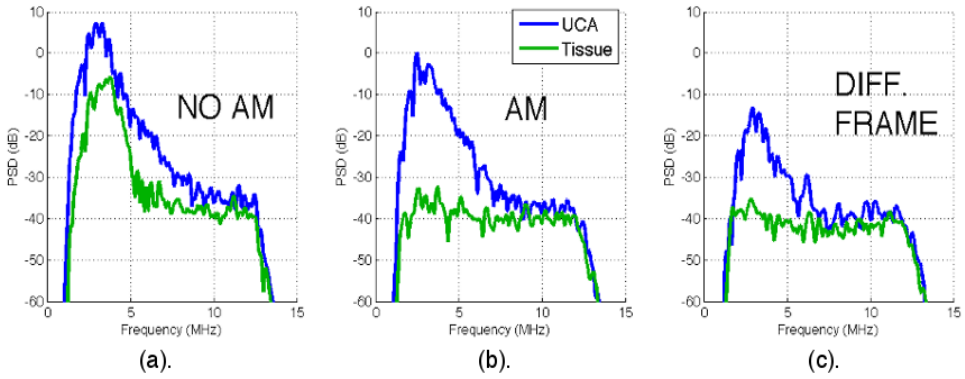

*Figure 6:6 PSD of a single RF **F** frame (a), of an RF frame after AM processing (**2H-F**) (b), and of the RF difference of two consecutive **F** frames ($F_{i+1} - F_i$) (c). The 3.5 MHz peak after AM processing (b) is chosen as the 0 dB level for all of the three plots. In all cases, a strong UCA signal is visible, with the main peak being located at the fundamental frequency. The mean flow speed was 55 mm/s.*

When AM processing is applied (Figure 6:6(b)), the tissue signal is suppressed by at least 30 dB, and it is lost amidst the noise background. The UCA signal only experiences a 5-8 dB reduction around the fundamental frequency, while preserving a bandwidth very similar to the pulse-echo (Figure 6:6(a)) case. At this stage, both contributions from bubble motion and nonlinear response will result in a signal that is not suppressed by the AM processing, and no distinction can be made yet. The ambiguity is partially resolved when the echoes from two identical pulses are subtracted (Figure 6:6(c)). In this case, all time-invariant contributions are suppressed, including those originating from the nonlinear behavior of the UCA. Changes by motion and/or destruction/deflation are not suppressed and become visible in the final difference frame. The UCA PSD peak level in Figure 6:6(c) is lower by about 12 dB than in the AM case (Figure 6:6(b)) and by about 20 dB compared to the standard pulse-echo PSD (Figure 6:6(a)). Considering these different UCA signal levels, we can conclude that AM processing determines a better CBR than the bubbles movement alone, although both nonlinearity and motion contribute to the final CBR.

The relation between signal loss by de-correlation and the flow velocity could be turned into a detection technique that discriminates slow from fast flow. Two separate frames could be distilled from an acquisition of a large ensemble (N>63) of angled plane wave sub-frames. By compounding all sub-frames, signals from fast flowing UCA will be reduced considerably, and only slow moving contrast will become visible. By compounding only a sub-set of the large ensemble, both slow moving and fast moving contrast will become visible. Such a capability generally is not possible when using a traditional focused contrast imaging approach.

6.5. CONCLUSIONS

In this work, Focused and Planewave were implemented and tested in a tissue mimicking phantom with flowing contrast. A fair comparison between the two methods was made, using the same UCA excitation pressure. Peak-negative pressures between 70 and 140 kPa were used, to ensure non-destructive detection of UCA. This allows use of high frame rate methods, such as compounded plane wave imaging, in which the same sample volume of UCA is illuminated with multiple US transmissions to form a single image. The results show that amplitude modulation multi-angle compounding yields higher contrast-to-background ratio (CBR) levels, typically 8 – 10 dB, and higher frame rates, typically at least by a factor 4, than conventional line-scanning (focussed) amplitude modulation scanning. The increase in CBR is attributed to the system noise reduction caused by coherently adding the frames in the angle plane wave compounding. A reasonable tradeoff between SNR, CBR, frame rate and image resolution is provided for Planewave with about 15-angle compounding. When using this number, the contrast is about 8 dB better than that obtained with conventional focused ultrasound in amplitude modulation mode. The influence of the flow speed appears to be substantial in determining the optimal number of plane wave transmission, since too long frame acquisition times can result in de-correlation of the signals of the flowing UCA. In our measurements, 63 sub-frames produced worse CBR than 31 sub-frames at mean flow speeds of 55 mm/s, caused by this de-correlation effect.

6.6. APPENDIX A

A parametric simulator was written in MATLAB® (The Mathworks, Natick, MA, USA) to simulate the backscattered echo of single, stationary, isolated, shelled microbubbles surrounded by a water-like fluid. The Marmottant model (Marmottant *et al.*, *JASA*, Dec.2005) was used to represent the bubble dynamic behavior. Results published by Overvelde *et al.* (Overvelde *et al.*, *Ultras.Med.Biol.*, Dec.2010) were used for realistic parameters for the bubble shell model, giving a shear viscosity of $\kappa_s = 6\ 10^{-9}$ and a shell elasticity of $\chi = 2.5$ N/m. An initial surface tension of $\sigma_0 = \sigma_w/2 = 0.036$ N/m was assumed. Bubbles with a diameter ranging from 1.5 µm to 6 µm were simulated. Each bubble was excited twice, respectively by a 70 kPa and a 140 kPa PNP, 3.5 MHz, 4-cycles tone burst with a Gaussian envelope. The 70 kPa echo time trace was then doubled and subtracted from the 140kPa echo time trace, in a manner similar to a 2-pulse AM processing.

Figure 6:7 shows the frequency spectra of the simulated bubble AM responses. For microbubbles larger than 2 µm diameter, a significant fundamental contribution is predicted by the model, even after AM processing. Notably, a significant subharmonic

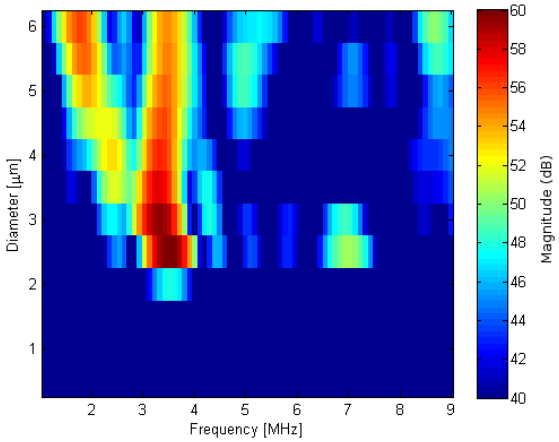

Figure 6:7 Simulation results for a single, isolated bubble, of parametric radius, after AM was applied. For this simulation, a full Marmottant model was used, with $\kappa_s = 6*10^{-9}$; $\chi = 2.5$ *N/m,* $\sigma_0 = 0.5$ *N/m ;* $\sigma_w = 0.036$ *N/m*

is also predicted for bubbles larger than 3 µm in diameter. However, it was not possible to observe this component in the experiments due to the subharmonic peak being outside of the bandwidth of the probe. The simulation data agrees with the experimental data as the fundamental component is the main contributor to the total UCA signal energy, and the second harmonic component is significantly lower at this pressure range.

REFERENCES

[1] N. de Jong, A. Bouakaz, and F. J. Ten Cate, "Contrast harmonic imaging," *Ultrasonics*, vol. 40, no. 1–8, pp. 567–573, May 2002.

[2] T. Faez, M. Emmer, K. Kooiman, M. Versluis, A. F. W. van der Steen, and N. de Jong, "20 years of ultrasound contrast agent modeling," *IEEE Trans. Ultrason., Ferroelect., Freq. Control*, vol. 60, no. 1, p. -, Jan. 2013.

[3] M.-X. Tang, N. Kamiyama, and R. J. Eckersley, "Effects of Nonlinear Propagation in Ultrasound Contrast Agent Imaging," *Ultrasound Med. Biol.*, vol. 36, no. 3, pp. 459–466, Mar. 2010.

[4] G. A. Brock-Fisher, M. D. Poland, and P. G. Rafter, "Means for increasing sensitivity in non-linear ultrasound imaging systems," US5577505 A, 26-Nov-1996.

[5] R. J. Eckersley, C. T. Chin, and P. N. Burns, "Optimising phase and amplitude modulation schemes for imaging microbubble contrast agents at low acoustic power," *Ultrasound Med. Biol.*, vol. 31, no. 2, pp. 213–219, Feb. 2005.

[6] P. N. Burns, D. Hope Simpson, and M. A. Averkiou, "Nonlinear imaging," *Ultrasound Med. Biol.*,, vol. 26, Supplement 1, pp. S19–S22, May 2000.

[7] R. J. Eckersley, M.-X. Tang, K. Chetty, and J. V. Hajnal, "Microbubble Contrast Agent Detection Using Binary Coded Pulses," *Ultrasound Med. Biol.*, vol. 33, no. 11, pp. 1787–1795, Nov. 2007.

[8] O. Couture, S. Bannouf, G. Montaldo, J.-F. Aubry, M. Fink, and M. Tanter, "Ultrafast Imaging of Ultrasound Contrast Agents," *Ultrasound Med. Biol.*, vol. 35, no. 11, pp. 1908–1916, Nov. 2009.

[9] G. Montaldo, M. Tanter, J. Bercoff, N. Benech, and M. Fink, "Coherent plane-wave compounding for very high frame rate ultrasonography and transient elastography," *IEEE Trans. Ultrason., Ferroelect., Freq. Control*, vol. 56, no. 3, pp. 489–506, 2009.

[10] M. Tanter and M. Fink, "Ultrafast imaging in biomedical ultrasound," *IEEE Trans. Ultrason., Ferroelect., Freq. Control*, vol. 61, no. 1, pp. 102–119, Jan. 2014.

[11] C. Tremblay-Darveau, R. Williams, Z. Zhang, L. Milot, M. Bruce, and P. N. Burns, "Adapting amplitude modulation to plane-wave non-linear Doppler imaging," in Ultrasonics Symposium (IUS), 2014 IEEE International, 2014, pp. 1742–1745.

[12] C. Tremblay-Darveau, R. Williams, L. Milot, M. Bruce, and P. N. Burns, "Ultrafast Doppler imaging of micro-bubbles," in Ultrasonics Symposium (IUS), 2012 IEEE International, 2012, pp. 1315–1318.

[13] E. Boni, A. Cellai, A. Ramalli, and P. Tortoli, "A high performance board for acquisition of 64-channel ultrasound RF data," in Ultrasonics Symposium (IUS), 2012 IEEE International, 2012, pp. 2067–2070.

[14] E. Stride and N. Saffari, "On the destruction of microbubble ultrasound contrast agents," *Ultrasound Med. Biol.*, vol. 29, no. 4, pp. 563–573, Apr. 2003.

[15] P. A. Dayton, K. E. Morgan, A. L. Klibanov, G. H. Brandenburger, and K. W. Ferrara, "Optical and acoustical observations of the effects of ultrasound on contrast agents," *IEEE Trans. Ultrason., Ferroelect., Freq. Control*, vol. 46, no. 1, pp. 220–232, Jan. 1999.

[16] O. Couture, M. Fink, and M. Tanter, "Ultrasound contrast plane wave imaging," *IEEE Trans. Ultrason., Ferroelect., Freq. Control,* vol. 59, no. 12, pp. 2676–2683, 2012.

[17] F. Guidi, H. J. Vos, R. Mori, N. de Jong, and P. Tortoli, "Microbubble characterization through acoustically induced deflation," *IEEE Trans. Ultrason., Ferroelect., Freq. Control*, vol. 57, no. 1, pp. 193–202, Jan. 2010.

[18] J. Kwan and M. Borden, "Microbubble shell break-up and collapse during gas exchange," in 2010 IEEE Ultrasonics Symposium (IUS), 2010, pp. 897–899.

[19] M. Emmer, A. van Wamel, D. E. Goertz, and N. de Jong, "The Onset of Microbubble Vibration," *Ultrasound Med. Biol.*, vol. 33, no. 6, pp. 941–949, Jun. 2007.

[20] P. Marmottant, S. van der Meer, M. Emmer, M. Versluis, N. de Jong, S. Hilgenfeldt, and D. Lohse, "A model for large amplitude oscillations of coated bubbles accounting for buckling and rupture," *The Journal of the Acoustical Society of America*, vol. 118, no. 6, pp. 3499–3505, Dec. 2005.

[21] M. Overvelde, V. Garbin, J. Sijl, B. Dollet, N. de Jong, D. Lohse, and M. Versluis, "Nonlinear Shell Behavior of Phospholipid-Coated Microbubbles," *Ultrasound Med. Biol.*, vol. 36, no. 12, pp. 2080–2092, Dec. 2010.

[22] F. Lin, C. Cachard, R. Mori, F. Varray, F. Guidi, and O. Basset, "Ultrasound contrast imaging: influence of scatterer motion in multi-pulse techniques," *IEEE Transactions on Ultrasonics, Ferroelectrics, and Frequency Control*, vol. 60, no. 10, pp. 2065–2078, Oct. 2013.

T. Leighton, chapter 3.2 in *The Acoustic Bubble*, pp.136-149. Academic Press, 2012.

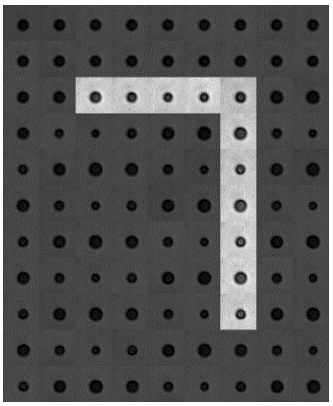

7. Detection of isolated single bubbles moving in a thin capillary using plane wave Power Modulation

***Abstract*— Detection and monitoring of ultrasound contrast agents (UCA) provide an effective diagnostic tool to assist clinicians assessing tissue perfusion and vascular pathologies in patients. Contrast detection methods with both high sensitivity and low contrast destruction rate are decisive to maintain diagnostic capabilities. A combination of plane wave transmissions with high number of compounding angles and power modulation is able to provide high-quality images at pressure levels that do not destroy UCA. Yet, it is unclear what contrast sensitivity levels can be obtained with such a combination. This study shows, by optical confirmation, that the scheme can detect single microbubbles in a realistic phantom setup. This finding is relevant for vasa vasorum imaging of the carotid artery, since a detection event can now be related to single microbubbles, which can travel through vessels with equally small diameters (order 5 µm). Additionally, using plane wave emissions in a nondestructive pressure regime, the system is suited to track the motion of single bubbles thus revealing the vascular structure.**

Printed with permission by authors: J. Viti, N. de Jong, F. Guidi, M.D. Verweij, P. Tortoli and H.J: Vos.

7.1. INTRODUCTION

Ultrasound contrast agent (UCA) imaging at a low mechanical index (MI) provides the opportunity to image microbubble UCA in real-time in both the microcirculation and in larger vessels. Specific applications in echocardiography include the assessment of atherosclerotic plaques in carotid arteries [1][2]. When imaging microcirculation, the ability to detect small amounts of slow-moving microbubbles becomes crucial. Therefore, ensuring a nondestructive MI is essential to prevent destruction of the limited amount of UCA normally present in such small vessels; however, limiting the MI begets a situation where the microbubbles echoes might be hard to identify against both the surrounding tissue echoes and the background noise.

Plane wave transmission was recently proposed as a method to combine high frame rate capabilities, sensitivity, and non-destructive UCA detection [8]. Ultrafast imaging methods, such as plane wave, allow for a dense time sampling of the whole scan plane, thus preserving flow and motion information. Although plane wave imaging is typically plagued by a low lateral resolution, coherent summation of multiple angled plane waves was shown as a viable method to simultaneously improve lateral resolution and SNR in the final image [6], still with high frame rates compared to traditional focused transmission. Additionally, the benefit of combining ultrafast imaging together with UCA is actively being investigated, with recent work showing the potential of super resolution imaging [10] and the advantage of having simultaneous Doppler and contrast imaging [8][9][10] .

To further improve detection sensitivity and specificity, various detection strategies were proposed to enhance the contrast between the UCA and the surrounding tissue. A largely used technique commonly referred to as either Power or Amplitude Modulation [5] consists of transmitting an ensemble of at least two pulses using different acoustic power, then rescaling and subtracting the echoes. This enhances nonlinear responses of UCA while suppressing the linear echoes from tissue. In case of amplitude modulation (AM), the amplitude is varied over the subsequent pulses by changing the amplitude of the transmitted pulse, which requires arbitrary waveform generators [7]. In case of power modulation (PM), the total acoustic power is regulated by transmission from either an interleaved subset or all of the elements, which requires only element-based on/off switching, and is implemented in many commercial systems. A nonlinear amplitude response of the bubbles has been experimentally shown in refs. [19][20][21] in in-vitro setups, albeit with either optical confirmation, or on bubble clouds only. A confirmation of the relation between an acoustically-observed scattering event and presence of a *single* microbubble is relevant for vasa vasorum imaging of the carotid artery, since a detection event could

then be related to vessels with equally small diameters (order 5 µm). This study combines plane wave compound imaging and power modulation in relation to single microbubble detection in a phantom setup realistic for carotid imaging applications.

7.2. MATERIALS AND METHODS

7.2.1. Setup

An experimental setup was built consisting of a custom-made flow phantom, a linear probe connected to a research scanner, and a microscope with a fast framing camera. As the phantom consisted of opaque material, no direct *simultaneous* optical confirmation of the presence of a single microbubble could be obtained. Therefore, the setup was devised which semi-simultaneously recording of the acoustic scattering of microbubbles, and down-stream optical confirmation of its singularity. Ideally, by knowing the flow speed of the liquid, the two detections can be correlated.

The flow phantom consisted of a cellulose capillary of 30 cm length and 160 µm inner diameter, held in a perspex container by two steel (syringe) needles. A section of about 5 cm of the capillary was embedded in a block of tissue mimicking agar-based material which was imaged using the ultrasound scanner. The tissue mimicking material was prepared according to the procedure proposed by Teirlinck *et al.*, for which an attenuation of 0.5 dB/ cm/ MHz was measured [11]. The capillary then ran, uninterrupted, out of the tissue mimicking block and through the optical focus of a bright-field microscope with 20x objective (UPLFLN 20x, Olympus). The microscope was connected to a fast framing camera (10k Redlake MotionPro, CA, USA) running at 250 frames per second, with a shutter time of 0.25 ms per frame, which prevented significant motion blur for traversing bubbles. About 0.5 mm of capillary length was captured in the camera frame, with an image scale of 0.61 micron/pixel.

A programmable syringe pump was used to push water into the flow phantom at a fixed volumetric flow rate of 0.4 µl/s. The imposed volumetric flow rate corresponds to a 20 mm/s mean flow speed within the capillary, which corresponds to 40 mm/s peak flow assuming a parabolic flow. Under these conditions, depending on the actual flow streamline that the microbubble is in, a single bubble traversing under the microscope was captured in 3-12 frames, allowing for easy identification.

A programmable research scanner (Vantage 256, Verasonics, WA, USA) was connected to a 128-elements linear array probe (L7-4, ATL/HDI, Philips Medical, Best, the Netherlands). The probe has an element pitch of 0.3 mm. The transmit frequency was 3.5 MHz, which corresponds to a pitch of 0.7λ which should provide very limited grating lobe effects in the transmit beam and reconstructed image. The transmit waveform was a tone burst of 4 cycles, and the voltage was set to an amplitude of 6.5

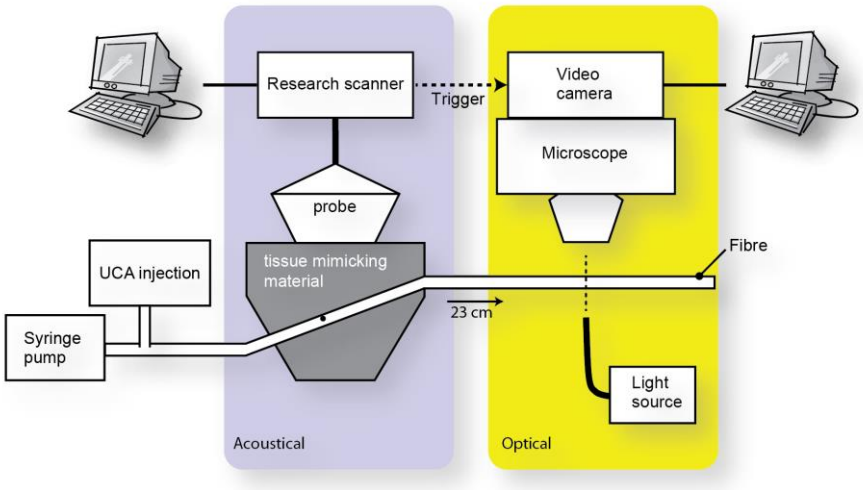

Figure 7:1 Experimental Setup

V. The receive bandwidth was set to 100% fractional bandwidth. The system was programmed to transmit a sequence of angled plane waves (-6.5 to +6.5 degrees, 15 angles) in power modulation (PM) mode. The PM mode consisted of transmission of a 3-pulse packet by subsequently firing from the odd elements (Half-odd, or $\mathbf{H_O}$), the full aperture (**F**), and the even (Half-even, or $\mathbf{H_E}$) elements. For one full ultrasound frame, 45 transmissions event are required (15x $\mathbf{H_O\text{-}F\text{-}H_E}$). At a pulse repetition interval of 160 µs, the total frame time is 7.2 ms. The dead time between two frames is 32.8 ms, yielding a frame rate of 25 frames per second (FPS). However, the dead time might be larger every 5 frames, when MATLAB interrupts the Verasonics program flow to perform user interface operations. After image reconstruction per transmit/receive event, done by the Verasonics software, intermediate PM frames were composed by processing the frames according to ($\mathbf{F} - \mathbf{H_O} - \mathbf{H_E}$). The final PM frame was then obtained by coherent summing of the 15 intermediate PM frames, each relative to a different transmission angle. This reconstruction was performed in real-time by the ultrasound scanner, so that a live PM image was visible; a circular buffer on the machine stored the RF channel data relative to the most recent 30 full PM frames.

7.2.2. Measurement protocol

At the start of each measurement session, fresh UCA (BR14, Bracco Research S.A., Geneva) was prepared and diluted in a 1:5000 ratio. Further dilution was then achieved by inserting a single drop into the water flowing into the phantom capillary. This process led to a decaying frequency of detection events over time. At a detection frequency of one microbubble every few seconds, as observed by continuous

monitoring of the acoustic images on-screen, the operator would initiate a trigger upon an acoustic detection. This trigger freezed the acoustic data acquisition on the scanner. It also triggered the fast framing camera to start recording 18 seconds of video, with a 2 s delay after the triggering. After video capture the ultrasound channel data, PM frames, and video frames were stored to disk for offline analysis.

7.2.3. Data analysis

We manually detected and located the microbubble events in the acoustical frames. Velocities were estimated by measuring the displacement of microbubbles in the subsequent frames and multiplying the resulting displacement estimate by the acoustical images frame rate (25 FPS). The optical frames were automatically processed for optimizing detection. In brief, this processing consisted of a background subtraction, pixel-by-pixel differentiation in time, and correlation of resulting image lines in the subsequent movies. The correlation function between two image lines shows the displacement of a microbubble in between two frames, and this displacement is again converted to a velocity by multiplication of the frame rate (250 FPS). This resulted in a map with velocity on the vertical axis, and frame number (or slow time) in the horizontal axis. An example is provided in the results section below. Such map easily reveals the detections of microbubbles, and their associated velocity in the optical images. The outcome was verified by manual inspection, and even weak detections of microbubbles were made visible by this automated processing, which would otherwise have been missed by regular visual inspection of the 4500 frames per recording.

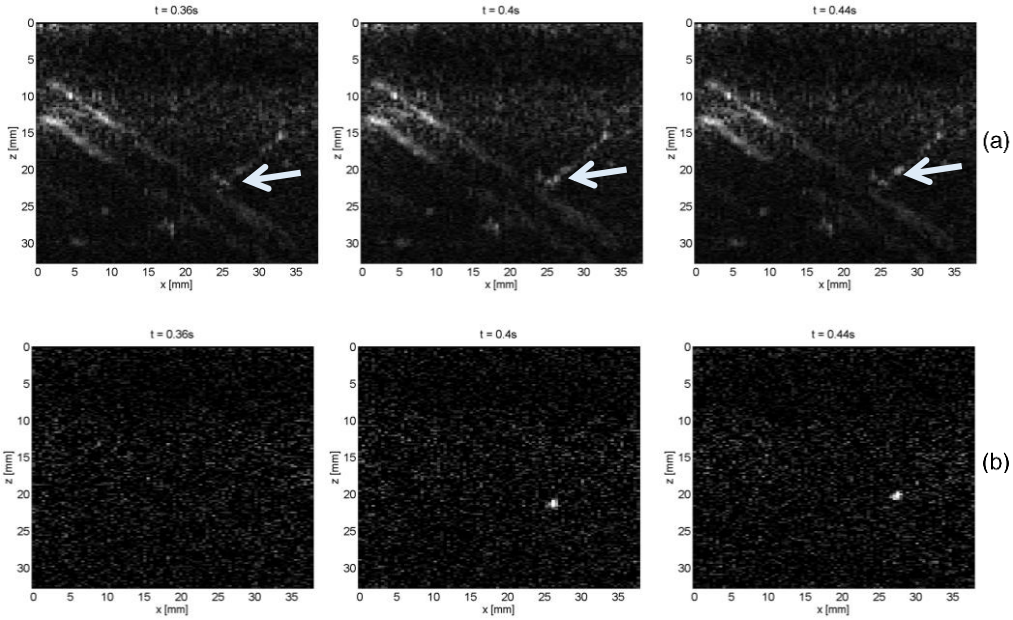

Figure 7:2 (a) Acoustical images after PM processing for the passage of a single microbubble in the capillary; (b) same acoustical images, after background subtraction

Tissue suppression and microbubble signal levels after PM processing were analysed in two different ways. Firstly, tissue suppression levels were obtained from enveloped-based images before and after PM processing of the data. The envelope-based image before PM processing was obtained by image reconstruction of the **F** frames only. Detection levels were obtained from the envelope-based images after PM processing. Secondly, signal spectra were obtained from IQ-format frames, which were reconstructed offline from the acquired RF data. The axial sampling of this data corresponded to ¼ λ sampling, which provides sufficiently large bandwidth for signal analysis. An acoustic event was manually located. A tissue region was selected at equal depth, in the center of the image which is outside of the image area containing the capillary.

7.3. RESULTS

7.3.1. Acoustic events

Eighteen events (i.e. passages of microbubbles) were recorded in which both an acoustical and optical detection was observed. See Figure 7:2 for example images of the acoustically observed events. The microbubble in the capillary is pointed to by the arrow in Figure 7:2, and the subsequent frames show the subsequent position of the microbubble from (x,z) = (25 mm,21 mm) to (26 mm, 20 mm). This corresponds to a velocity of about 35 mm/s, consistent with a mean flow of 20 mm/s and a peak flow of 40 mm/s, assuming a parabolic flow profile. By analyzing a large subset of the acoustic frames, an average velocity of 30 mm/s was found. The capillary runs from the region where the arrow points in a direction of 2 o'clock. The left upper corner of the frames (ranges: x = 0 – 10 mm, z = 8 – 18 mm) contains a residual echo from the phantom container wall. Further reduction of the tissue signal was obtained with a background subtraction of the PM-processed frames, see Figure 7:2B. The background-subtracted images show the location and trajectory of the microbubble even clearer. Note that such a background subtraction step is equivalent to a DC wall filter in ultrasound Doppler processing. The resulting images do show an acoustic detection, which implies that the acoustic detection levels are above the noise.

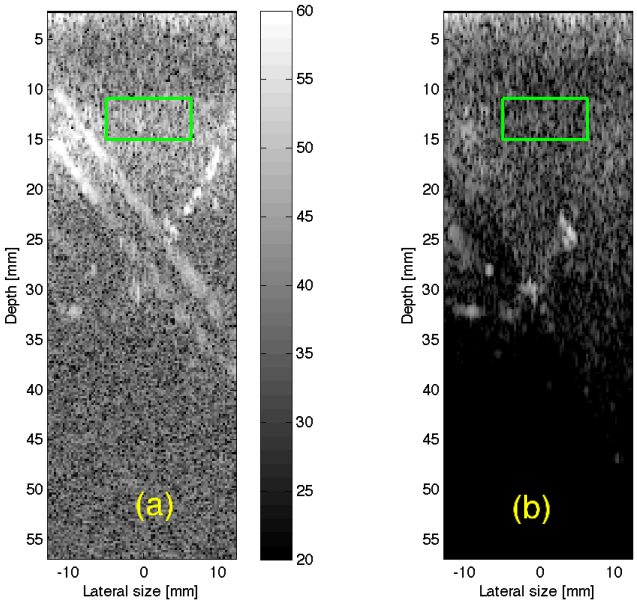

Figure 7:3 Images (a) before and (b) after PM processing of the acoustic frames. The box indicates the region wehere the tissue signals before and after PM processing are obtained.

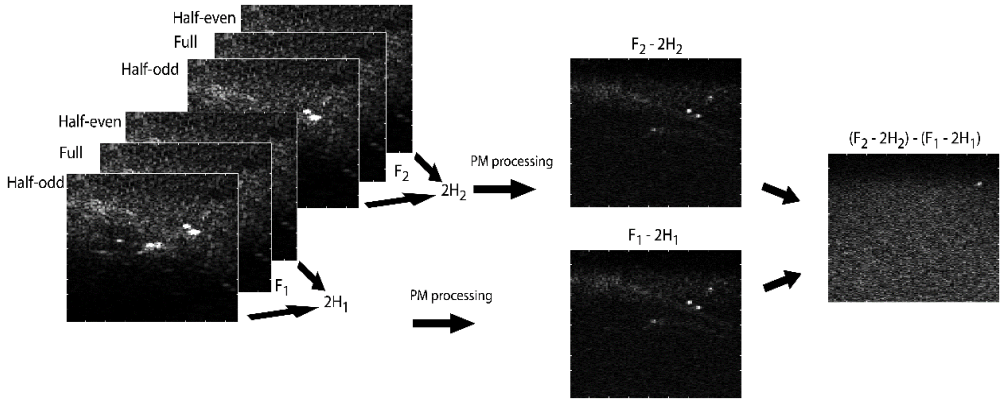

Figure 7:4 Schematic representation of the data processing steps before the spectra of signals could be analyzed. From left to right: The frames obtained by transmitting from all even, full, all odd elements are combined through PM processing into detection frames. To further suppress residual tissue signals and stationary bubble signals, the difference frame is calculated between two subsequent detection frames (40 ms interfame time).

A first quantitative analysis of the acoustical frames is done from these envelope-based frames, see Figure 7:3. Figure 7:3a shows an acoustic image before the PM processing. Again, the reflections from (-10 mm, 10 mm) to (12 mm, 35 mm) are caused by the inclined wall of the phantom. The capillary runs from (5 mm, 25 mm) to (12 mm, 12 mm) as visible by the brighter line, caused by acoustic reflection. Figure 7:3b shows the image after PM processing. The major reflections observed before PM processing are significantly suppressed. A remaining reflection is visible at (5 mm, 25 mm), which corresponds to the location of the tip of the steel needle holding the capillary. Although this reflection is suppressed by the PM processing, the amplitude of the reflection after PM processing still is larger than that of the surrounding tissue. The tissue power levels in the rectangular boxes in Figure 7:3 are reduced by 22 dB to 27 dB, with a mean of 24 dB, after PM processing. A minor difference between two measurement days exists for the mean tissue suppression, i.e., the tissue suppression is 22.6 dB on one day and 26.1 dB on the other. The reason for this difference between two days is not known.

The microbubble signal levels varied much more between various detections, which can be expected from the polydispersed size range and consequent different responses of microbubbles to the excitation. The range was 5 dB to 21 dB, with a mean value of 12.3 dB.

A second quantitative analysis is done by looking at the spectra of the signals in a tissue region, and around an acoustic detection. For this analysis, IQ-data based frames are taken before and after PM processing. To further isolate the acoustic

detection, residual tissue signals and those from stationary bubbles were removed by taking the difference of two subsequent PM processed frames. See Figure 7:4 for a schematic representation of the steps taken for analysis. The microbubble signal was manually located in the difference frame, since in that frame the location was most clear (See Figure 7:4, right hand side). Tissue signal was obtained from a region at equal depth as the microbubble, but located in the center of the image where only tissue mimicking material was presented.

Figure 7:5 shows the spectra of the signal at the bubble location and the tissue location before and after PM processing. The tissue spectra before PM processing, i.e., the **F** and **2H**=$\mathbf{H_E}$ + $\mathbf{H_O}$, are very similar. This is expected since tissue scattering is a linear process, nonlinear propagation will be negligible in the fundamental frequency band in the weak nonlinear regime. Within this assumptions, only noise can disrupt the correlation between the **F** and **2H** spectra. A high signal to noise ratio is indicated by the high similarity in tissue signals in the current setup, which will be further addressed in this analysis. The spectra in the **F** frame and **2H** frame for the microbubble location also are very similar to each other. Although a nonlinear response from the microbubbles is typically expected, such nonlinear response is not visible in these spectra. The microbubble signal level is below the tissue signal level and it is thus completely masked by the latter.

When PM processing is applied to the signals, the spectra denoted with **F-2H** in Figure 7:5 were obtained. The tissue signal at the transmit frequency of 3.5 MHz were suppressed by about -30dB. Note that the tissue reduction observed earlier in the image, i.e., in (x,z) domain, is a result of integration over the full frequency band, which therefore is lower than the -30 dB difference at exactly 3.5 MHz reported here. The spectrum from the microbubble shows a peak level of -20 dB at the transmit frequency. Therefore, the contrast-to-tissue ratio was +10 dB in this case. The contrast signal, originally buried in tissue signal, now has higher levels than tissue, showing the detection efficacy of the PM processing.

Residual tissue signals were further suppressed by calculating the difference between two subsequent frames (Figure 7:4, right hand side), which would clarify the detection levels and the source of the detection. Figure 7:6 shows these spectra, normalized by the bubble detection signal in the frame obtained by $\mathbf{F_2 - F_1}$ (blue solid line in Figure 7:6). The tissue **F** spectrum (dashed blue line) is suppressed to values of around -26 dB, while the **2H** tissue spectra are suppressed to about -23 dB. The PM

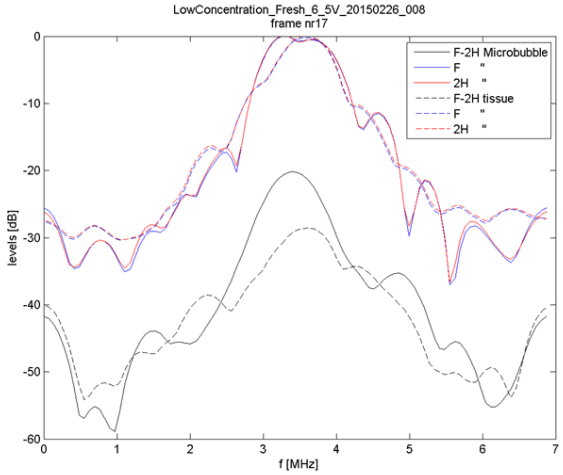

Figure 7:5 Spectra from the microbubble location and tissue location as obtained from the IQ-based images.

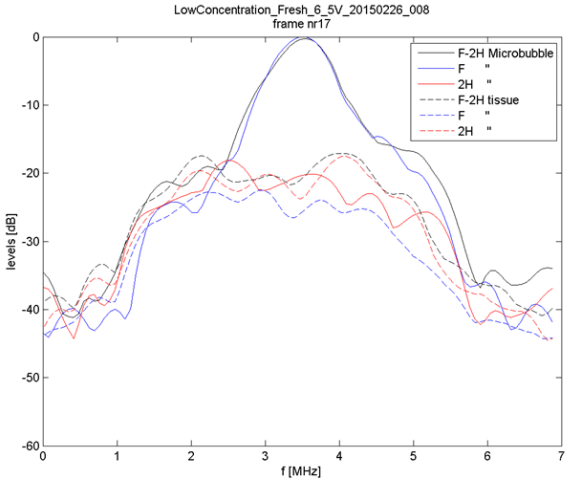

*Figure 7:6 Spectra from the microbubble location and tissue location as obtained from the difference of two subsequent IQ-based images. For example, the "**F** Microbubble" spectrum is obtained from the $\boldsymbol{F_1 - F_2}$ frames. The **F-2H** spectra are evaluated on the difference frame of two PM images, as depicted in Figure 4 (far right). The difference step further reduces residual tissue levels to below the noise floor.*

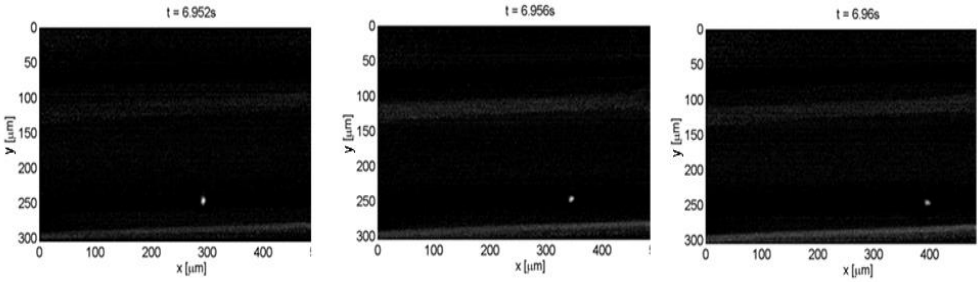

Figure 7:7 Optical images of the transit of a single microbubble, after background subtraction

processed spectrum is around -20 dB. These levels can be related to each other through the following rationale. After the difference processing, the **F** spectrum in Figure 7:6 is calculated by subtracting two IQ_based frames: $\mathbf{F_2 - F_1}$. The **2H** spectrum is calculated from four frames: $\mathbf{2H_2 - 2H_1} = (\mathbf{H_{E2}} + \mathbf{H_{O2}}) - (\mathbf{H_{E1}} + \mathbf{H_{O1}})$. Likewise, the **F-2H** spectrum is calculated from addition and subtraction of 6 frames in total. Addition and subtraction of N frames leads to $\sqrt{N}$ higher noise power. Consequently, for the **2H** and **F-2H** spectra, the noise can be expected to increase by a respective $\sqrt{2}$ = 3dB and $\sqrt{3}$ = 4.8 dB, compared to the noise in the **F**-spectrum. The observed trend indeed is consistent with the expectation. Consequently, the single frame noise level (without taking a difference frame) can be assumed another 3 dB below that of the difference **F**-frame, i.e., at a level of -29 dB compared to the bubble detection signal. Since that level already was 20 dB below that of non-processed tissue signal (Figure 7:5), we can conclude from this analysis that the tissue signals in a single frame have 49 dB SNR level. To summarize this example, the PM-processed contrast signal had a contrast-to-noise ratio of about 20 dB, and a contrast-to-tissue level of about 10 dB. The tissue SNR levels in a single **F** frame were estimated about 49 dB.

The microbubble spectra in the **F** frame and the PM-processed frame (**F - 2H**) are very similar, while that signal is lost in noise in the **2H** frame. This indicates the actual source of the PM detection signal: when the microbubble is insonified by the half-amplitude transmits, it does not respond significantly. When it is insonified by the full-amplitude transmit, it does respond, thus providing the contrast signal after PM processing. Such a non-linear response in the fundamental frequency band was previously attributed to a thresholding effect [19][20][21]. The theory [20][21] and experimental measurements [19][21] show that for specific combinations of size and driving pressure, microbubbles can have a pressure threshold below which they do not respond to the excitation, while above this threshold they do respond. The observed phenomenon in Figure 7:6 is consistent with this earlier experimental optical and numerical data, now shown in a realistic experiment with a commercial scanner and an ultrasound phantom.

7.3.2. Optical events

Figure 7:7 shows example optical frames in which the microbubble trajectory is clearly captured. In this case the microbubble has traveled 105 μm in 0.008 s (2 frame intervals at 250 frames/s), yielding a velocity of 13.1 mm/s. The background was suppressed by calculating the pixel mean over the 4500 frames and subtracting this mean frame from all frames. Because of out-of-focus effects a microbubble was generally not observed as clearly as in this example. The out-of-focus effect precluded a direct size estimate from the optical recordings, and there was no visible relation between the bubble size and the intensity of the bubble ultrasound echo (results not shown). Yet, by observing the shape of the microbubble detection, we could observe whether it were single microbubbles or clusters.

For a further analysis of the optical frames, we cross-correlated horizontal lines of subsequent frames. A displacing spot in the frames results in a local maximum of this cross-correlation function. The location of the local maximum is a direct measurement of the velocity by its location in the cross-correlation function (representative of the displacement between the frames) and the frame rate. Therefore, the cross-correlation method results in a velocity – frame number panel as depicted in Figure 7:8. A microbubble appears as a white vertical short line in this panel, for which the vertical location corresponds to its speed observed from the subsequent frames. The horizontal location is the frame numbers in which the microbubble appears. The white curve shows the relation between the apparent velocity in subsequent frames, and the expected arrival time of the microbubble, based on a 23 cm capillary length between the acoustical detection region and the optical field of view. This curve can be used to estimate the chance that an optically observed microbubble is the same as the acoustically observed microbubble.

The panel in Figure 7:8 shows 6 detections of microbubbles. Except for the detection in frame 2522, the microbubbles were optically verified to be single microbubbles. The image in frames 2522 and 3515 are shown in the insets. A detection of 6 microbubbles in 18 s, or 1 per 3 s, on average, can be looked upon as a highly diluted suspension of microbubbles. The average distance, with a mean flow 20 mm/s, is 60 mm, well above the voxel size of less than 1 mm^3. Therefore, we can safely assume that the microbubbles were isolated in the acoustical recordings.

By analysis of a large subset of the optical movies, the average velocity of detected microbubbles was 17 mm/s. This is slower than the acoustically observed velocities. This result and the implications are further discussed in the appropriate section below.

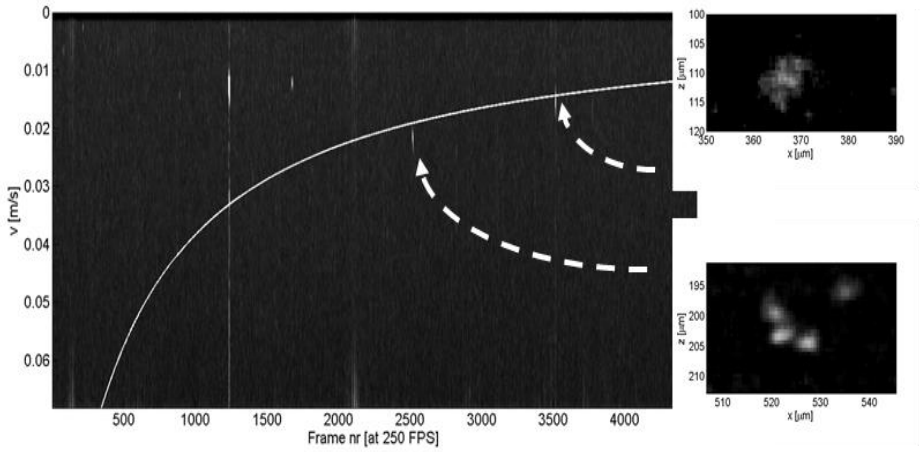

Figure 7:8 Detection panel for the optical frames. A microbubble appears as a white vertical short line in this panel, for which the vertical location corresponds to its speed observed from the subsequent frames. The horizontal location is the frame numbers in which the microbubble appears. The white curve shows the relation between the apparent velocity in subsequent frames, and the expected arrival time of the microbubble, based on a 23 cm capillary length between the acoustical detection region and the optical field of view. This curve can be used to estimate the chance that an optically observed microbubble is the same as the acoustically observed microbubble. The inset shows the optical detection in frame 3515 of a single out-of-focus microbubble and a cluster of microbubbles in frame 2522.

7.4. SUMMARY AND DISCUSSION

In this chapter we have shown that very low concentrations of microbubbles, down to the level of isolated microbubbles, can be detected with a multi-angle plane wave power modulation (PM) detection scheme. The isolation of the microbubbles was optically verified. The signal to noise ratio (SNR) of the contrast detection was on the order of 20 dB after PM processing, while the contrast to tissue levels were between 5 dB and 21 dB. These levels are quite remarkable given the small size of microbubbles (order 1 to 10 µm) while the depth of detection was 25 mm. The high SNR level can be attributed to a low noise performance of the ultrasound system, in combination with the multi-angle plane wave compounding which reduces noise by averaging [see chapter 6 of this thesis]. The good contrast to tissue levels are attributed to a high linearity in the ultrasound system. It can be expected that commercial high-end clinical systems are capable of achieving similar noise levels and linearity. Since the phantom setup included realistic tissue scattering, we do believe that such values are representative for in-vivo results as well.

The source of the signal was identified to be pressure-dependent microbubble response, which was earlier identified in in-vitro setups and numerical simulations [19][20][21]. This also led to the observation that most signal is present in the fundamental frequency band, which relaxes the bandwidth constrained which is generally encountered in second harmonic detection schemes. Moreover, the scattering amplitude of microbubbles generally is higher in the fundamental frequency band than the second harmonic, especially in the non-destructive regime that was aimed for in the current detection scheme. This all supports our hypothesis that we are able to detect single microbubbles in a realistic phantom setup.

We originally tried to match acoustic and optical events on a one-to-one basis in the experiments. In principle, the synchronization of optical and acoustical recordings should allow identification of the optical detection that most likely corresponds to the acoustic detection. The solid line in Figure 7:7, which predicts the frame number in which the microbubble should arrive for a given velocity, is an attempt in that direction. Yet, one-to-one synchronization was found not feasible in the current setup. In cases of very low concentrations (one or two detections per 18 s optical movie), the detections would not fit the frame/velocity curve. Moreover, in few cases, an acoustical detection would not lead to any optical detection of a microbubble. These results suggest that the semi-simultaneous acoustical and optical detection failed for real one-to-one matching. Various possible reasons could be identified:

i. Some bubbles were sticking in the capillary nearby the acoustic detection area. Such sticking down-stream the acoustic detection area would result in no possible optical detection;

ii. The bubble traveling speed is unknown, and depends on its position in the flow. Assuming a parabolic flow profile, the velocity could become anything between 40 mm/s (in the center) down to a few mm/s or even zero, in case of sticking. Moreover, because of buoyancy effects and lift forces, the microbubble may gradually change its position within this flow, leading to an error in the relation between expected detection frame and its apparent velocity;

iii. Bubble disruption / ultrasound induced deflation was experimentally observed to occur for the sticking microbubbles in the acoustic detection area after 1 second of insonation. This could have led to an unintentionally destruction of the bubble before travelling towards the optical detection area;

iv. Because of a limited optical focal area, microbubbles may have travelled in an area of the capillary where the out-of-focus blurring is too large to identify a microbubble. The error was attempted to be minimized by putting the focus roughly in the upper region of the capillary, where the microbubbles have a higher chance of being located during travel because of buoyancy.

To overcome the above reasons, it may be worthwhile to devise an optical window which is very near to the acoustical detection region, without disrupting the acoustic field and the tissue mimicking material, and having a larger focal area.

In addition to the points raised above, the Verasonics was operated in an asynchronous mode in which data are continuously captured by the hardware and streamed to the host PC, while the software running at the host PC is continuously and independently using the buffered data for image reconstruction and display; cyclically, this sequence of operations was interrupted whenever control was passed back to MATLAB® to allow it to perform user interface routines, as detailed in section II-A. This inconsistency in the dead time between frames can occasionally lead to apparent 'jumps' of microbubbles between frames in the acoustic recordings. When that was observed, those recordings were not taken into account for the mean velocity estimation for the acoustical data.

To further reduce residual tissue signals after PM processing, we applied either a background subtraction or a difference frame processing step (see Figure 7:4). Either step results in reduction of so-called tissue clutter. One implication of the improvement on the detection sensitivity by this clutter reduction is that a PM Doppler-like processing technique such as used by Tremblay-Darveau *et al.* [8][9] should be able to localize single displacing microbubble signals with an even greater sensitivity. The contrast signal remains 20 dB above the noise level, while in the original PM processing technique, the contrast signal is 10 dB above the tissue level. The difference, however, between PM processing alone or a Doppler-based PM detection technique is that the original PM processing works for both stationary and flowing contrast, while the Doppler processing needs flowing contrast to be detected. On the other hand, a recent paper [8] exploits the difference in stationary and flowing contrast by selection of the Doppler frequency bands for distinction of tissue perfusion and vascular imaging. Our results show that the sensitivity of the PM detection scheme, in combination with a flexible research system, should be able to track isolated microbubbles through the microvascular system.

REFERENCES

[1] D. E. Goertz, M. E. Frijlink, N. de Jong, and A. F. W. van der Steen, “Nonlinear intravascular ultrasound contrast imaging,” *Ultrasound in Medicine & Biology*, vol. 32, no. 4, pp. 491–502, Apr. 2006.

[2] D. E. Goertz, M. E. Frijlink, D. Tempel, V. Bhagwandas, A. Gisolf, R. Krams, N. de Jong, and A. F. W. van der Steen, “Subharmonic Contrast Intravascular Ultrasound for Vasa Vasorum Imaging,” *Ultrasound in Medicine & Biology*, vol. 33, no. 12, pp. 1859–1872, Dec. 2007.

[3] R. J. Eckersley, C. T. Chin, and P. N. Burns, “Optimising phase and amplitude modulation schemes for imaging microbubble contrast agents at low acoustic power,” *Ultrasound in Medicine & Biology*, vol. 31, no. 2, pp. 213–219, Feb. 2005.

[4] O. Couture, S. Bannouf, G. Montaldo, J.-F. Aubry, M. Fink, and M. Tanter, “Ultrafast Imaging of Ultrasound Contrast Agents,” Ultrasound Med. Biol., vol. 35, no. 11, pp. 1908–1916, Nov. 2009.

[5] G. Montaldo, M. Tanter, J. Bercoff, N. Benech, and M. Fink, “Coherent plane-wave compounding for very high frame rate ultrasonography and transient elastography,” IEEE Trans. Ultrason. Ferroelectr. Freq. Control, vol. 56, no. 3, pp. 489–506, 2009.

[6] M. Tanter and M. Fink, “Ultrafast imaging in biomedical ultrasound,” *IEEE Transactions on Ultrasonics, Ferroelectrics, and Frequency Control*, vol. 61, no. 1, pp. 102–119, Jan. 2014.

[7] P. Tortoli, L. Bassi, E. Boni, A. Dallai, F. Guidi, and S. Ricci, “ULA-OP: an advanced open platform for ultrasound research,” *IEEE Transactions on Ultrasonics, Ferroelectrics and Frequency Control*, vol. 56, no. 10, pp. 2207–2216, 2009.

[8] C. Tremblay-Darveau, R. Williams, L. Milot, M. Bruce, and P. N. Burns, “Ultrafast Doppler imaging of micro-bubbles,” in *Ultrasonics Symposium (IUS), 2012 IEEE International*, 2012, pp. 1315–1318.

[9] C. Tremblay-Darveau, R. Williams, L. Milot, M. Bruce, and P. N. Burns, “Combined perfusion and doppler imaging using plane-wave nonlinear detection and microbubble contrast agents,” *IEEE Transactions on Ultrasonics, Ferroelectrics, and Frequency Control*, vol. 61, no. 12, pp. 1988–2000, Dec. 2014.

[10] C. Tremblay-Darveau, R. Williams, Z. Zhang, L. Milot, M. Bruce, and P. N. Burns, “Adapting amplitude modulation to plane-wave non-linear Doppler imaging,” in Ultrasonics Symposium (IUS), 2014 IEEE International, 2014, pp. 1742–1745.

[11] C. J. P. M. Teirlinck, R. A. Bezemer, C. Kollmann, J. Lubbers, P. R. Hoskins, P. Fish, K.-E. Fredfeldt, and U. G. Schaarschmidt, “Development of an example flow test object and comparison of five of these test objects, constructed in various laboratories,” *Ultrasonics*, vol. 36, no. 1–5, pp. 653–660, Feb. 1998.

[12] M. Emmer, A. van Wamel, D. E. Goertz, and N. de Jong, “The Onset of Microbubble Vibration,” *Ultrasound Med. Biol.*, vol. 33, no. 6, pp. 941–949, Jun. 2007.

[13] P. Marmottant, S. van der Meer, M. Emmer, M. Versluis, N. de Jong, S. Hilgenfeldt, and D. Lohse, “A model for large amplitude oscillations of coated bubbles accounting for buckling and rupture,” *The Journal of the Acoustical Society of America*, vol. 118, no. 6, pp. 3499–3505, Dec. 2005.

[14] M. Overvelde, V. Garbin, J. Sijl, B. Dollet, N. de Jong, D. Lohse, and M. Versluis, “Nonlinear Shell Behavior of Phospholipid-Coated Microbubbles,” *Ultrasound Med. Biol.*, vol. 36, no. 12, pp. 2080–2092, Dec. 2010.

[15] M. Emmer, H. J. Vos, D. E. Goertz, A. van Wamel, M. Versluis, and N. de Jong, "Pressure-dependent attenuation and scattering of phospholipid-coated microbubbles at low acoustic pressures," *Ultrasound in Medicine and Biology*, vol. 35, pp. 102-111, Jan 2009

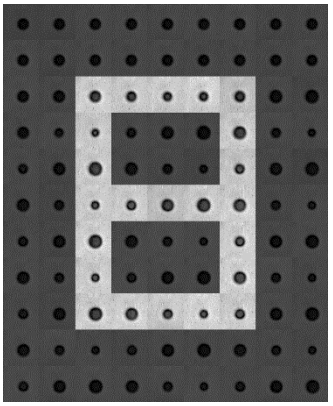

8. Summary and outlook

In the late eighties and early nineties contrast agents for ultrasound were developed consisting of small microbubbles. The main goal at that time was to enhance the Doppler signal. The Doppler signal was based on the scattering of red blood cells and was only about 10 dB above the noise level and could only be seen in larger vessels and cavities like the left ventricle cavity. The scattering in smaller vessels especially those vessels smaller than the resolution cell was much smaller than the surrounding tissue and therefore could not be detected. The solution to this problem were these small bubbles and it was believed that ultrasound contrast agents (UCA) could be sufficiently detected and imaged with the conventional imaging methods nowadays referred to as fundamental imaging. In the late nineties newer imaging techniques, like pulse inversion and power modulation proved to be more sensitive since they were based on specific properties of the UCA. In general, these new characteristics involve non-linear and transient characteristics of contrast agents. Imaging modalities used today for UCA are, besides fundamental imaging also second harmonic imaging, pulse inversion, amplitude modulation and subharmonic imaging. Also Doppler imaging proved to be very sensitive. Doppler methods are based on the phase relation in subsequent interrogations. If there is a high correlation (low velocity) in these subsequent signals the phase shift is low. Is there a low correlation (high velocity) then this result in a high phase shift. Microbubbles are in this respect very interesting scatterers. The scattering properties of these bubbles can change every time they are insonified and this change is of very high amplitude and frequency dependent.

Recently plane wave imaging became possible and currently the benefits and advantages are explored in this thesis and also by different groups over the world resulting in promising results. In general for optimal contrast imaging knowledge of the precise interaction of the microspheres in the UCA and the ultrasound wave is crucial.

When a gas bubble is hit by an ultrasound wave it generates two kinds of response, see Chapter 3. First, the wave will be reflected at the interface between the bubble and the surrounding tissue because of the large difference in acoustic impedance between the two. More important, however, is the volume pulsation which occurs when the bubble is hit by an ultrasound wave with a wavelength much larger than the bubble size (for a 3 MHz ultrasound wave the wavelength in water is 0.5 mm). In the simplest situation the size of the bubble decreases in the positive cycle of the ultrasound wave, and the bubble expands in the negative cycle. The volume pulsation of the bubble is frequency dependent and shows a clear maximum at a specific frequency, the resonance frequency. For a 4 μm diameter bubble, for example, the resonance frequency is approximately 1.6 MHz. For ultrasound contrast imaging

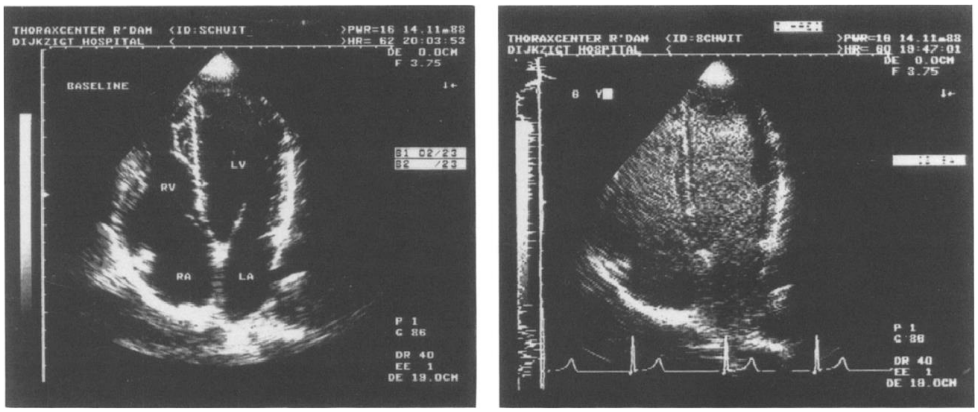

Figure 8:1 Representative example of a 2D-echocardiographic four-chamber view in one of the subjects. Left panel shows an echo image before intravenous injection of Albunex®; right panel, 40 s after injection.
Abbreviations: LA = left atrium; LV = left ventricle; RA = right atrium; RV = right ventricle, see [1]

the volume pulsation causes an enhancement of the backscatter signal from the bubble, as shown throughout this thesis, and this phenomenon is used to detect the bubble in the presence of tissue. This bubble vibration can be detected in fundamental imaging, harmonic imaging, pulse inversion, amplitude modulation or combination of pulse inversion and amplitude modulation (Chapter 5).

In the fundamental imaging mode the effect of the UCA is demonstrated by an increase in grey-scale value. This has been employed in combination with conventional two-dimensional imaging to create images of greater clarity. For example, left ventricle opacification improved the endocardial border detection resulting in better imaging of wall motion abnormalities.

An example of a 4 chamber view as recorded after an intravenous injection of Albunex is given in Figure 8:1. The left image shows the chambers before contrast administration, the right panel after. Delineation of the left ventricle cavity is clearly improved. However, in hyperechoic regions or very small vessels where the number of bubbles is low, echoes from surrounding tissue can easily mask the increase in grey-scale. For the myocardium, for example, the ratio of the blood volume and tissue is less than 10 and, consequently, the increase from UCA in the myocardium will be about a few dB, for concentrations used in clinical studies. Therefore, fundamental grey-scale imaging results in poor contrast agent detectability in the presence of tissue. This is very clear in Figure 8:2. Although it is believed that the contrast agent has flowed into the coronary system in the myocardium no intensity increase could be detected. New imaging techniques needed to be developed based on specific properties of UCA. By

utilising these properties it is possible to eliminate the tissue because of the absence of these properties in tissue.

8.1. HARMONIC IMAGING

For small amplitudes of the ultrasound wave the relative compression and expansion of the bubble is the about the same. For higher amplitudes, compression retards relative to expansion and non-linearity starts to occur, i.e the change in bubble size is not linearly related to the applied acoustic pressure. Consequently, the bubble also vibrates at second and higher multiples of the interrogating frequency, see Chapters 4b and 5. In this way, the backscatter signal from the bubble not only contains the transmitted fundamental frequency, but also other 'harmonic' frequencies, most notably twice the transmitted frequency. This effect is less prominent in tissue, and therefore it offers the possibility of separating the response of the bubble from that of the surrounding tissue. In this mode, the ultrasound system separates the harmonic part of the received signal from the fundamental part and then processes this harmonic signal alone. To increase the sensitivity of the system in detecting the agent, the contribution from tissue, due to spectral overlap between the fundamental and second harmonic parts, has to be reduced. This is carried out by transmitting narrow-band signals at the cost of a deterioration of the image resolution (see Chapter 4a).

Harmonic imaging, originally developed for imaging of UCA, is now a tissue imaging modality on its own, and is generally called 'native harmonic' or 'tissue harmonic' imaging, see Chapter 4a. Tissue harmonic imaging exploits the gradual generation of harmonic energy as the ultrasound wave propagates through tissue. This is due to a slight non-linearity in sound propagation that gradually deforms the shape of the wave, and results in development of harmonic frequencies, which were not present in the transmitted wave. In general this is bad news for contrast detection schemes. The non-linearities as generated during propagation are in competition with the nonlinearities of the bubble vibration.

8.2. PULSE INVERSION AND POWER MODULATION

Currently the most often used imaging methods are Pulse inversion or Power modulation or a combination of amplitude and power modulation. These methods have a better axial resolution than the harmonic imaging as described above since it can use the full bandwidth of the transducer. This comes at the cost of frame rate since multiple pulses has to be transmitted. In pulse inversion a sequence of 2 ultrasound wave is transmitted into the tissue. The second wave is transmitted after a suitable delay and is an inverted replica of the first wave. For a linear medium the response of

the second wave is an inverted copy of the response from the first wave, and the sum of these two responses is zero. For a non-linear system, such as bubbles the sum will not be zero and the rest value is related to the degree of non-linearity (see Chapters 6 and 7 in particular). In amplitude modulation the second wave has an amplitude which is 2 times of the amplitude of the first transmit wave. Now, first the scatter amplitude of the first transmission is multiplied by 2 and then subtracted from the scattering of the second transmission. For linear systems the outcome is again zero while this is nonzero for nonlinear systems.

8.3. SUBHARMONIC IMAGING

Although the harmonic nature of oscillating gas bubbles has been exploited extensively, new opportunities arise by applying the subharmonic component of an oscillating gas bubble, see Chapter 5. Under specific conditions, gas bubbles generate subharmonics, which occur at half the transmitted frequency. According to theory, the onset of subharmonic for a free gas bubble depends on the transmitted frequency and the applied acoustic pressure. The acoustic pressure for the onset of subharmonic scattering is at its minimum at twice the resonance frequency of the gas bubble. Additionally, narrow band signals are needed because the generated subharmonic components will be more dominant when the number of periods increases. This generally leads to a reduced axial resolution compared to higher harmonic sequences. Several investigators have described the possibility of subharmonic imaging for ultrasound contrast agents [2-4]. One of the main advantages of subharmonic imaging is that, unlike (second) harmonic imaging, the contribution of tissue is minimal at acoustic pressures currently used in diagnostic ultrasound, which will result in a high agent-to-tissue ratio. Yet, our results in Chapter 5 show that the contrast to tissue ratio and contrast to noise ratio are modest. The exact reason has not become clear, but spectral leakage from fundamental tissue signal is a good candidate for the apparent subharmonic signal from tissue. Subharmonics are currently not used in diagnostic ultrasound because the imaging resolution is too low. A new transducer design and imaging strategy are essential to optimally exploit the advantages of subharmonic imaging.

8.4. PLANE WAVE IMAGING

Bubble vibrations are very depending on the acoustic pressure. For low pressures (below 50 kPa) the vibration can be considered as linear. Between 50 and 150 kPa the amplitude of the vibration clearly increases and non-linear components arises which are depending on resonance frequency of the bubble together with the applied frequency of the ultrasound wave, see Chapters 2 and 3. Above 150 kPa the response of the microbubble is not stable anymore and will vary from one insonification to the

next one. The bubble becomes smaller after each insonification and starts to disappear. So to do continuous imaging then either the replenishment of the destroyed bubbles should be adequate or the acoustic pressure should remain clearly below the destruction level, say 100 kPa. This is called low MI imaging. Sufficient replenishment is obvious in high flow area like the left ventricle cavity and high acoustic pressures are allowed. In slow flow area, like the myocardium high acoustic pressures will continuous destroy the agent and no clear signal will be seen.

Pulse inversion imaging and amplitude modulation normally is performed in the low MI-mode, see Chapter 5. This means that the acoustic pressure is around 100 kPa and there is no serious bubble destruction. On the other hand, these PI and AM schemes are normally implemented in a system doing conventional imaging, this means line by line scanning. In line by line scanning all the acoustic elements are focussed on a specific line. In this focussed mode the highest possible acoustic pressure is close or above 2 MPa, but this pressure is not at all permitted in a contrast mode with continuous scanning. On the contrary, in the plane wave mode all the acoustic elements are excited in the same phase and the possible acoustic pressure reached in the region of interest is now much lower only a few hundreds of kPa. This makes plane wave intrinsically fit for low MI imaging, and it can easily be tuned to operate at a pressure where no bubble destruction occurs and yet the bubble vibrates nonlinearly.

In the study in chapter 6 we have investigated the difference in plane wave and focussed imaging. In this study we have also included the level of the resolution and this could be controlled by adapting the number of plane wave angles. As stated in this chapter a reasonable tradeoff between SNR, CBR, frame rate and image resolution is provided for plane wave with about 15-angle compounding. When using this number, the contrast is about 8 dB better than that obtained with conventional focused ultrasound in amplitude modulation mode. However, with plane wave transmission it is possible to improve contrast, and thus sensitivity, even beyond: it was shown in chapter 6 (see Figure 6:6) that the AM pulsing scheme is capable of suppressing tissue echoes by about 30 dB, whereas the echoes coming from a population of bubbles are suppressed only by 8 dB; by compounding a large number of plane wave transmissions, a dramatic improvement in both SNR and CBR can be achieved with respect to traditional focused AM, given that the imaging conditions allow for such an extensive number of plane waves to be compounded without destroying the contrast signal. Specifically, the flow speed should be very low, to prevent motion decorrelation of the contrast signal while transmitting a long ensemble of plane waves. Additionally, bubble disruption due to repeated ultrasound stress should be kept negligible; in the study in Chapter 3 we have shown that, when

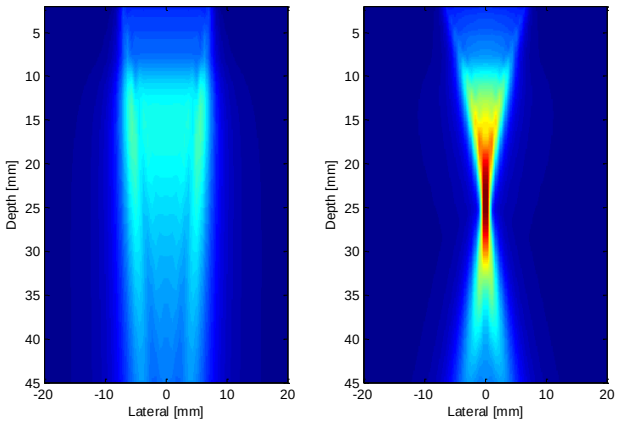

Figure 8:2 Simulated pressure distribution. Left Plane wave, right focused beam. The peak pressure point in plane wave transmission (left) is located at 18mm, at the focus of a simulated acoustical lens that focuses the beam on the elevation-depth plane (not shown). For a simulation with 64 active elements, the peak pressure for plane wave is 4 times less intense than the focused case.

using a very low MI (MI < 0.08), bubble destruction is not a noticeable phenomenon, although changes in bubble size (i.e. bubble deflation) can occur under a few hundred of transmitted pulses; therefore contrast bubbles have been shown capable of surviving thousands of low MI pulses. Finally, it should be considered that using a wide scan angle, although beneficial to image resolution, can lead to a partial suppression of target echoes if the target is not a perfectly isotropic one; for this reason, it is best to use a limited scan angle to maintain a high correlation between echoes obtained under different angles of view. We can therefore conclude that, if the resolution constraint is further relaxed from what we have shown in chapter 6 and the flow is only a few mm/s instead of 20 mm/s plane wave can provide a CBR improvement greater than 8 dB, possibly up to an improvement of 15-20 dB over focused amplitude modulation imaging.

REFERENCES

[1] de Jong N, ten Cate FJ, Vletter WB, Roelandt JR. Quantification of transpulmonary echocontrast effects. Ultrasound Med Biol. 1993;19(4):279-88. Epub 1993/01/01.

[2] Krishna PD, Shankar PM, Newhouse VL. Subharmonic generation from ultrasonic contrast agents. Physics in medicine and biology. 1999;44(3):681-94.

[3] Sarkar K, Shi WT, Chatterjee D, Forsberg F. Characterization of ultrasound contrast microbubbles using in vitro experiments and viscous and viscoelastic interface models for encapsulation. J Acoust Soc Am. 2005;118(1):539-50.

[4] Shi WT, Forsberg F, Hall AL, Chiao RY, Liu JB, Miller S, et al. Subharmonic imaging with microbubble contrast agents: initial results. Ultrasonic imaging. 1999;21(2):79-94.

Summary

Being able to directly image blood is a key ability in early detection of cardiovascular diseases and cancer. Direct imaging of blood with ultrasound, however, is hindered by the fact that blood is an hypoechoic medium compared to the surrounding soft tissues, and thus appears as a dark image area that can be difficult to effectively discriminate from other shadows appearing in the image.(see **chapter 1**).

To resolve this ambiguity, ultrasound contrast agents (UCA) were developed as a medium that is injected in a patient's circulation to enhance the backscattering properties of blood (see **chapter 2**). Simultaneously, specific methods were developed to reliably detect and image UCAs in the bloodstream. Nowadays, research effort on UCA and their imaging methods is still ongoing in order to maximize detectability and diagnostic effectiveness of contrast agents, whilst ensuring safety and minimal invasiveness for the patient.

The driving motivation behind this thesis is to help improve the visualization modalities for blood imaging in human arteries; most notably by exploring optimal imaging methods to maximize the contrast between UCAs and the surrounding tissues.

To pursue this objective, we first turned our attention to understanding the fundamental dynamics of a single coated bubble, when it oscillates in response to prolonged ultrasound excitation. In **chapter 3,** isolated phospholipid-coated microbubbles were placed in a thin capillary tube, excited with hundreds of ultrasound pulses at a low mechanical index (MI) and their oscillations captured using the Brandaris-128 ultrahigh-speed camera. This investigation showed that repeated excitation at a low MI does, in fact, prevent destruction of UCA; yet microbubbles undergo an irreversible shrinking process, which is associated with several strongly asymmetric oscillations, such as compression-only and expansion-only behavior, all of which were directly observed in our experiments. Notably, expansion-only behavior is associated with a rapid size reduction, whereas compression-only behavior mostly occurs without a noticeable change of the bubble radius.

Nonlinear response to ultrasound of UCA is a key feature that is commonly exploited in ultrasound imaging to identify and differentiate such agents from their surroundings. Traditionally, second harmonic imaging is employed to detect ultrasound contrast agents; however, as wave propagation through the tissue also generates nonlinear components, relying on second harmonic components only can sometimes provide unsatisfactory results in terms of both specificity and sensitivity to UCA. We thus investigated the benefits of using more than a single frequency to image

UCAs: in **chapter 4** we followed a double-pronged approach, first demonstrating how multi-frequency transmission can be effectively used as a novel approach to image tissue at a higher framerate than traditional approaches, while maintaining compatibility with second harmonic imaging; this laid the foundations to eventually perform fast harmonic imaging of UCA within tissue. Then, the UCAs itself were considered as a source capable of emitting more than a single frequency, leading us to investigate the advantages of using UCA imaging based on the third or higher harmonics, i.e. "superharmonic" imaging. In both investigations multi frequency imaging modes are shown to be advantageous compared to a traditional B-mode imaging approach.

Comparing the performance of different contrast imaging techniques can be difficult and somewhat confusing; despite a vast available literature on contrast imaging, each technique is typically tested using different in vitro setups, contrast agents, ultrasound transducers and systems. To achieve a systematic comparison of various available imaging methods, we report in **chapter 5**, on the implementation of arbitrary contrast-pulse-sequences (CPS) in the ULA-OP open ultrasound system. Combined with a home-made phantom, a convenient and consistent evaluation of the main parameters characterizing various techniques is obtained. Several experiments were performed exciting BR14 microbubbles at various dilution rates, with an average MI = 0.1, through 10 different excitation schemes including power modulation, chirp reversal and their combination. It was shown that amplitude modulation, and to a greater extent its combination with chirp excitation, denoted Chirp amplitude modulation, provide the highest contrast-to-tissue ratio, ensuring a high detectability of UCA at a very low MI.

Contrast detection methods with both high sensitivity and low contrast destruction rate, which is enforced by imposing a very low MI, are essential to maintain diagnostic capabilities. Plane wave transmission with high number of compounding angles was suggested in recent years to produce good quality images at pressure levels that do not destroy UCA. In **chapter 6**, we performed a quantitative evaluation of detection efficacy of flowing UCA with either traditional focused scanning or ultrafast plane wave imaging. The influence of the number of compounding angles, peak-negative pressure and flow speed on the final image quality was investigated. Results show that the images obtained by compounding multiple angled plane waves offer a greater contrast with respect to focused-scanning amplitude modulation. This increase is attributed mainly to noise reduction caused by the coherent summation in the compounding step. Additionally, we show that highly sensitive detection is already achieved with a limited compounding number, thus suggesting the feasibility of continuous contrast monitoring at high frame rate. This capability is essential to properly detect contrast agents flowing at high speed, as an excessive angle

compounding is shown to be destructive for the contrast signal, as the UCA motion quickly causes loss of correlation between consecutive echoes.

The findings of **chapter 6** were confirmed and further expanded upon in **chapter 7**, where we explored what contrast sensitivity levels can be obtained when combining plane wave emission and amplitude, or power, modulation for UCA imaging. This study shows, by optical confirmation, that the scheme can detect single microbubbles in a realistic phantom setup. This finding is relevant for vasa vasorum imaging of the carotid artery, since a detection event can now be related to single microbubbles, which can travel through vessels with equally small diameters (order 5 µm). Additionally, using plane wave emissions in a nondestructive pressure regime, the system is suited to track the motion of single bubbles thus revealing the vascular structure. Having obtained and discussed these results, we therefore reached our proposed goal.

A final summary and an outlook on the status of contrast agent imaging is finally discussed in **chapter 8**.

Samenvatting

Het afbeelden van bloed en daarmee de doorbloeding is van groot belang voor vroege diagnostiek van hart- en vaatziekten en kanker. Het direct afbeelden van bloed met ultrageluid wordt echter bemoeilijkt door het feit dat bloed weinig verstrooiing geeft ten opzichte van het omliggende zachte weefsel. Op echobeelden wordt bloed dan ook als een donkere regio weergegeven. Daardoor is het moeilijk om bloedregio's te onderscheiden van donkere schaduwdelen in het beeld (zie **Hoofdstuk 1**).

In het verleden is de oplossing van dit probleem gevonden in het gebruik van microscopisch kleine gasbellen, verkrijgbaar als commerciële ultrageluidscontrastmiddelen die intraveneus worden toegediend bij de patiënt. Deze belletjes hebben een diameter van ruwweg 1 tot 10 micrometer, en worden daarom microbellen genoemd. Vanwege hun grootte en de gebruikte materialen vormen ze geen gevaar voor de gezondheid. De microbellen blijven in de bloedbaan en verstrooien het ultrageluid beter dan weefsel zodat de bloedbaan beter oplicht op een echobeeld (**hoofdstuk 2**).

Omdat de golflengte van het ultrageluid veel groter is dan de beldiameter gaan de microbellen volumetrisch trillen in een ultrageluidsveld Ter illustratie, de golflengte van regulier ultrageluid van 3 MHz frequentie heeft een golflengte van 0,5 mm in water terwijl een resonerende microbel bij die frequentie een diameter heeft van ongeveer 2 µm. Het volumetrisch trillen is analoog met een massa-veersysteem, waarbij de 'veer' wordt gevormd door de compressibiliteit van het gas, en de 'massa' wordt gevormd door de omliggende vloeistof. De amplitude van de trilling hangt af van de frequentie waarmee de microbel wordt aangestraald en is maximaal op de resonantiefrequentie. De volumepulsaties geven een vergroting van het echosignaal van bellen ten opzichte van het omliggende weefsel, zoals beschreven is in dit proefschrift. In de loop der jaren zijn verschillende detectiemethodes ontwikkeld om deze contrastmiddelen nog beter te detecteren, en deze ontwikkelingen gaan nog steeds door. Dit is ook de onderliggende motivatie voor dit proefschrift. De aanpak die we hebben ligt in het optimaliseren van afbeeldingstechnieken om de detectie van de contrastmiddelen ten opzichte van het omliggende weefsel te vergroten.

Om dit doel te bereiken hebben we eerst een fundamentele studie uitgevoerd naar het gedrag van geïsoleerde microbellen in respons op een lange ultrageluidsexcitatie (**hoofdstuk 3).** Met behulp van een microscoop en de Brandaris-128 hogesnelheidscamera hebben we de vibraties optisch afgebeeld met 13 miljoen beelden per seconde Het resultaat van deze studie is dat de repeterende excitatie bij lage drukken van het ultrageluid geen volledige destructie veroorzaakt, maar het veroorzaakt wel een afname van de belgrootte. Deze afname gaat samen met sterke

asymmetrische vibraties, waarbij of de expansiefase of juist de compressiefase van de vibratie een grotere amplitude krijgt. Deze hebben we direct waargenomen in onze experimenten. Uitgesproken expansie was gerelateerd aan een snelle afname van de belgrootte, terwijl uitgesproken compressie juist samengaat met een stabilisatie van de belgrootte. De asymmetrie in compressie en expansie van de microbel is een niet-lineair effect in de volumepulsatie van de bel, die zich vertaalt in zowel fundamentele als harmonische frequentiecomponenten in het verstrooide veld. Het harmonische verstoringseffect is veel minder aanwezig in weefsel, en biedt daarmee een mogelijkheid om belresponsies te scheiden van weefselresponsies via de spectrale componenten. Traditioneel worden alleen de tweede harmonische signalen afgebeeld. Om de beldetectiegevoeligheid te vergroten moeten weefselsignalen verder worden onderdrukt. Dit wordt gedaan door relatief smal-bandige signalen uit te zenden zodat spectrale overlap tussen de (hoog-amplitude) fundamentele weefselresponsie en de (lage-amplitude) harmonische belresponsies wordt verkleind. Dit gaat dan wel ten koste van de axiale resolutie in het beeld (**Hoofdstuk 4a**). Daarnaast zal de propagatie van de uitgezonden drukgolf in het weefsel zelf ook niet-lineaire verstoring van de puls geven, die ook in de weefsel-reflectie signalen terecht komt. Het alleen afbeelden van de tweede-harmonische signalen zal hierdoor niet voldoende contrast opleveren tussen het contrastmiddel en weefsel.

In hoofdstuk 4 hebben we geavanceerde technieken bestudeerd waarbij meerdere frequenties worden gebruikt om contrastmiddelen af te beelden. In het eerste deel van het hoofdstuk hebben we een multi-frequentie aanpak beschreven waarmee weefsel kan worden afgebeeld via de niet-lineaire eigenschappen. Deze nieuwe methode leidt tot hogere beeldfrequentie dan die van de conventionele methodes, en is compatibel met de reguliere tweede-harmonische afbeeldingstechniek. Deze nieuwe methode heeft een fundering gelegd onder de methodes van snelle afbeeldingstechnieken van contrastmiddelen in de latere hoofdstukken. Daarnaast hebben we de contrastmiddelen beschouwd als bron van hogere harmonische waarbij we de voordelen hebben bestudeerd van het gebruik van de derde, vierde en vijfde harmonische reflecties ('superharmonische' afbeeldingstechniek, **hoofdstuk 4b**). Beide studies laten zien dat multi-frequentie afbeeldingstechnieken voordelen bieden ten opzichte van conventionele afbeeldingstechnieken.

Om een systematische vergelijking te maken van de verschillende detectie methodes van microbellen hebben we een studie gedaan met het ULA-OP open platform (**hoofdstuk 5**). In combinatie met een zelfgemaakt fantoom hebben we een consistente evaluatie kunnen doen van de invloed van de verschillende methodes op de detectieniveaus van contrastmiddelen. De experimenten zijn gedaan met BR14 contrastmiddelen (Bracco research, Genéve, Zwitserland) bij verschillende verdunningen. Het relatieve drukniveau in deze experimenten kwam overeen met een

MI van 0.1, waarbij MI staat voor de Mechanische Index, een maat gerelateerd aan de kans op het ontstaan van spontane cavitatiebellen in weefsel (maximale toegestane waarde is 1.9). Een waarde van 0.1 is heel laag en wordt gezien als niet-destructief voor ultrageluidscontrastmiddelen. We hebben tien verschillende detectieschema's bekeken, waaronder amplitudemodulatie, puls-inversie, chirp-reversie, en combinaties hiervan. Het bleek dat amplitudemodulatie, zeker gecombineerd met chirp-reversie, het hoogste contrast gaf tussen de contrastmiddelen en weefsel.

Contrast detectiemethodes met zowel een hoge gevoeligheid en een lage destructiegraad (verzekerd door gebruik van relatief lage akoestische drukken) zijn essentieel voor de diagnostische toepassing. Recent zijn vlakke-golf excitatiemethodes geïntroduceerd waarbij het hele afbeeldingsgebied in één of slechts enkele ultrageluidstransmissies wordt aangestraald. Deze methode vergroot de beeldfrequentie aanzienlijk, tot een factor honderd. Het gebruik van deze nieuwe vlakke golf excitatie voor de detectie van de microbellen wordt in **hoofdstuk 6** beschreven. In dat hoofdstuk voeren we een kwantitatieve vergelijking uit tussen traditioneel gefocusseerd ultrageluid en via vlakke-golf excitatie met een contrastmiddel in een stromende vloeistof. We hebben gekeken naar de invloed van het aantal vlakken dat gecombineerd wordt tot één beeld, de gebruikte akoestische drukken, en de doorstroomsnelheid op de beeldkwaliteit. De resultaten laten zien dat de beelden verkregen met de vlakke-golf excitatie een hoger contrast geeft dan de conventionele methode. Deze verhoging van het contrast wordt veroorzaakt door de verlaging van de ruis als gevolg van het coherent middelen van de verschillende signalen. We laten bovendien zien dat een verhoging van contrast al wordt bereikt bij een relatief klein aantal hoeken waarmee de geluidsgolven worden uitgezonden, hetgeen suggereert dat een hoge beeldfrequentie bereikt kan worden over langere periodes. Dit is van belang om hoge bloedsnelheden nog goed te kunnen afbeelden daar anders al de gereflecteerde signalen van opeenvolgende beelden al decorreleren..

De resultaten uit hoofdstuk 6 zijn verder bekeken in **hoofdstuk 7** waarin we de gevoeligheid meten van de vlakke-golf excitatiemethode gecombineerd met amplitudemodulatie. Deze studie laat zien, via optische verificatie, dat individuele bellen gedetecteerd kunnen worden in een realistische fantoom-opstelling. Dit gegeven is relevant voor het afbeelden van de zogenaamde *vasa vasorum* in de carotide arteriën, omdat nu een detectie van een contrastsignaal gerelateerd kan worden aan de detectie van geïsoleerde microbellen die in vaten van gelijke grootte kunnen reizen (orde 5 micrometer). De bewegingen van enkele bellen zijn te traceren dankzij het gebruik van vlakke golven, zodat het vaatstelsel nauwkeurig kan worden afgebeeld. Hiermee hebben we ons doel bereikt.

Sommario

La capacità di visualizzare il sangue costituisce uno strumento essenziale per la diagnosi precoce di patologie cardiovascolari ed oncologiche. Nel campo dell'ecografia ad ultrasuoni, tuttavia, tale capacità è resa difficile dal fatto che il sangue è un mezzo ipoecogeno rispetto ai tessuti molli circostanti; pertanto il sangue tipicamente appare nell'immagine ecografica come una regione scura, spesso difficile da distinguere da altre regioni altrettanto scure per cause diverse (es: shadowing). (vedi **capitolo 1**).

Per superare questa ambiguità sono stati sviluppati appositi agenti di contrasto (Ultrasound Contrast Agents - UCA,); tali agenti possono essere iniettati nel paziente per via endovenosa e migliorano le proprietà ecogene del sangue (vedere **capitolo 2**). Nel corso di intense ricerche, sono state sviluppate specifiche tecniche di elaborazione del segnale ecografico al fine di esaltare il contrasto tra UCA in circolo e tessuti molli circostanti. L'interesse di ricerca verso gli agenti di contrasto ed i relativi algoritmi per la loro individuazione e visualizzazione è notevole tutt'oggi, ed è mirato a massimizzare la capacità diagnostica degli UCA garantendola massima sicurezza e minima invasività per il paziente.

L'obiettivo di questo lavoro di tesi è di contribuire a migliorare le modalità di imaging ad ultrasuoni, attraverso l'esplorazione di nuovi metodi d'indagine mirati, in particolare, a massimizzare il contrasto tra gli UCA ed i tessuti molli circostanti.

A tale fine, è stata rivolta in primo luogo una particolare attenzione alla comprensione delle dinamiche fondamentali della singola microbolla, componente il mezzo di contrasto ed in generale costituita da un nucleo di gas racchiuso entro un guscio lipidico, in risposta ad una prolungata sollecitazione ultrasonica. Nello studio descritto all'interno del **capitolo 3**, alcune microbolle sono state isolate, posizionate all'interno di un sottile tubo capillare e sollecitate con un treno di centinaia di impulsi ultrasonici ad un basso indice meccanico (MI); le oscillazioni di tali microbolle erano registrate mediante la Brandaris-128 camera. Questa indagine ha mostrato che una sollecitazione a basso MI, anche se ripetuta centinaia di volte, non comporta la distruzione degli agenti di contrasto; le microbolle, tuttavia, subiscono un'irreversibile rimpicciolimento, che è associato ad oscillazioni fortemente non lineari, come ad esempio compression-only o expansion-only; ambedue i comportamenti sono stati osservati direttamente nel corso dei nostri esperimenti. In particolare, il comportamento di tipo expansion-only è correlato ad una rapida riduzione delle dimensioni, mentre il compression-only si manifesta senza che si osservi simultaneamente un cambiamento significativo nelle dimensioni della microbolla.

La risposta non lineare agli ultrasuoni è una caratteristica distintiva degli UCA che viene comunemente impiegata nelle tecniche di imaging per esaltare il contrasto (*contrast imaging*). Trasmettendo in fondamentale e ricevendo in seconda armonica, ci si aspetta di ricevere solo i contributi nativi degli UCA. Purtroppo però la propagazione dell'onda ultrasonica all'interno dei tessuti è essa stessa un processo non lineare che dà origine a contributi armonici indesiderati. E' pertanto possibile che le tecniche basate solo sulla seconda armonica non siano sempre in grado di fornire i risultati desiderati in termini sia di specificità che di sensibilità agli UCA. Per queste ragioni abbiamo quindi esplorato la possibilità di utilizzare più di una singola frequenza di trasmissione o di ricezione per creare l'immagine. Nel **capitolo 4** viene descritta tale indagine portata avanti su due filoni: in primo luogo si è dimostrato sperimentalmente come la trasmissione multi-frequenza possa essere usata efficacemente per a scandire i tessuti molli ad un frame rate più elevato di quello normalmente consentito dai metodi a scansione tradizionale; tale metodo mantiene inoltre la compatibilità verso l'imaging non lineare basato sulla seconda armonica.. In secondo luogo, gli UCA sono stati considerati come delle sorgenti capaci di emettere segnale su più di una frequenza; questo ci ha portato ad esplorare i benefici derivanti da un metodo basato su armoniche di ricezione superiori alla seconda, battezzato "superharmonic imaging". In entrambe le indagini, i metodi di imaging multi-frequenza hanno dimostrato alcuni vantaggi, a fronte di alcuni limiti, rispetto ad un approccio di tipo B-mode tradizionale.

Confrontare le prestazioni di differenti metodi di imaging con mezzo di contrasto presenta sfide di non banale risoluzione; nonostante sia disponibile un'ampia letteratura, ogni tecnica viene tipicamente testata e descritta utilizzando setup sperimentali differenti, rendendo quindi molto complesso, nel confronto tra due o più tecniche, individuare quali differenze siano imputabili al metodo e quali invece al particolare setup, mezzo di contrasto, sonda e macchinario ad ultrasuoni utilizzati. Un confronto sistematico e paritario tra le differenti tecnicheè riportato nel **capitolo 5**, dove si descrive l'implementazione sulla piattaforma aperta ULA-OP di metodi di imaging basati su sequenze di impulsi arbitrarie (Contrast Pulse Sequences, o CPS). Utilizzando la medesima piattaforma accoppiata con un test phantom appositamente realizzato si è riusciti ad ottenere in maniera efficace e consistente una valutazione comparativa dei principali parametri che caratterizzano le principali tecniche presenti in letteratura. Sono stati condotti diversi esperimenti, utilizzando un mezzo di contrasto BR-14 diluito a varie concentrazioni, per esplorare un totale di 10 differenti tecniche di imaging, tra cui power modulation, chirp reversal, e le loro combinazioni; ogni tecnica è stata valutata mantenendo un *Mechanical Index* (MI) medio di 0.1. Si riporta che amplitude modulation, ed in misura ancora maggiore la sua combinazione con una trasmissione chirp, che prende il nome di Chirp Amplitude Modulation,

fornisce il miglior contrasto tra UCA e tessuto, garantendo quindi una grande sensibilità agli UCA anche in condizioni di basso MI.

Riuscire ad effettuare imaging del mezzo di contrasto mantenendo simultaneamente una alta sensibilità ed una bassa percentuale di distruzione del mezzo di contrasto, che viene garantita imponendo un basso MI, è essenziale per permettere un esame diagnostico significativo. Negli ultimi anni, la trasmissione di onde piane ad angoli diversi, e la successiva ricostruzione sintetica dell'immagine attraverso la combinazione e l'elaborazione dei rispettivi echi, sono state proposte per produrre immagini a frame rate molto elevato (dell'ordine dei kHz). Abbiamo quindi valutato la possibilità di combinare tale tecnica con l'uso di mezzi di contrasto, mantenendo in trasmissione un MI sufficientemente basso da non causare una loro distruzione significativa. Nel **capitolo 6** abbiamo effettuato un confronto quantitativo della capacità di rilevamento di UCA in movimento utilizzando sia un approccio a scansione tradizionale, basato su trasmissione focalizzata, sia un approccio ad alto frame rate con trasmissione ad onda piana. In particolare si è indagato sull'influenza che il numero di angoli usati per la ricostruzione, la depressione di picco (peak-negative pressure, PNP), e la velocità del flusso degli agenti presentano sulla qualità dell'immagine finale. I risultati mostrano che le immagini di tipo amplitude modulation ottenute dalla combinazione di onde piane offrono un contrasto maggiore rispetto alle immagini ottenute con una tecnica di scansione tradizionale. Questo miglioramento è attribuito in misura principale alla riduzione del rumore dovuta alla somma dei segnali ecografici nel processo di combinazione. Inoltre viene mostrato che un' alta sensibilità agli UCA viene già raggiunta combinando un numero ridotto di onde piane, rendendo tale tecnica potenzialmente idonea per monitorare gli UCA in modo continuo ad alto frame rate. Questa capacità è essenziale per riuscire a rilevare correttamente il mezzo di contrasto quando si muove a grande velocità all'interno del vaso sanguigno. Una ricostruzione dell'immagine che utilizzasse un elevato numero di angoli sarebbe infatti distruttiva per il segnale eco degli UCA, poiché il movimento di questi ultimi porta rapidamente ad una decorrelazione del segnale tra echi successivi.

Quanto riportato nel **capitolo 6** è stato confermato ed espanso nel **capitolo 7**, dove è stata valutato quali livelli di contrasto siano ottenibili combinando trasmissione ad onda piana con amplitude, o power, modulation per il rilevamento degli UCA.. In questo studio viene mostrato, e confermato in maniera diretta tramite osservazione ottica, che la tecnica è capace di rilevare delle singole microbolle in un setup in vitro con un fantoccio realistico. Tale risultato è di significativa importanza laddove si desideri effettuare, ad esempio, l'imaging della struttura dei vasa vasorum nell'arteria carotidea, dal momento che un evento di rilevamento può in tal modo essere riferito anche a singole microbolle, che sono capaci di attraversare vasi di diametri comparabili al proprio (dell'ordine dei 5 µm). Inoltre, dal momento che viene fatto uso di trasmissioni ad onda piana in un regime di pressione non distruttivo, il sistema si

dimostra capace di inseguire lo spostamento di singole bolle, di fatto rendendolo capace di mappare completamente la struttura vascolare.

Un riassunto conclusivo e le considerazioni finali sullo stato dell'imaging con mezzo di contrasto viene infine discusso nel **capitolo 8.**

Acknowledgments

Looking back after four long years of PhD it is hard not to be impressed seeing how winding was the road that brought me to claim this milestone today. It was a road of traveling, personal growth, new experiences, memorable friendships, and, sadly, personal loss. All this would not have been possible without the support from many people whom I had the pleasure to meet along the way.

I'd like to thank Prof. Piero Tortoli, for selling me on the idea of pursuing a co-supervised Ph.D. in the first place, and in second place for being a mentor and a supervisor to me despite my lack of fervent support for the Fiorentina football team.

I'd like to thank Prof. Ton Van Der Steen for giving me the chance to work in a very stimulating and international environment that gave me the chance to enjoy each of my stays in Rotterdam.

I'd like to thank Prof. Nico de Jong, for accepting to be my Dutch supervisor and maintaining always a positive and interested mindset towards the progress of my work.

Rik, I wish you could have been my co-supervisor since day 0. Not only you were always very helpful in discussing my planning and my results, you were also very understanding of my doubts and fears whenever they surfaced, and always offered me a concrete help to keep things on track. You went a mile beyond what I saw as your role as my co-supervisor, and I enjoyed every moment spent working with you.

Riccardo, you left an impression on me that will not fade. I like your enthusiasm, your great energy and your humility. You proved yourself exceptional not just only as a scientist and a colleague, but as a personal friend. I will not forget our chats where we talked about science but also shared both our problems and our successes with a smile, even when our visions did not match. I will continue to take good care of the cactus you gave me.

Deep, I liked your confidence and your smile. You are very curious and open to talk about just anything: you did not hesitate to talk with me about your scientific research and ask me for my opinion; and whenever I had some doubts, you always had some good advice (and/or some good beer) to share. I liked our fusion dinners and our nights out. I wish you and your wife and baby all the best.

Alex and Rebecca, I am very happy to have met you two. Alex, in the year we lived together you were an elder brother to me and Ilya, bullying us around to keep the house clean and in good shape. And yet, right after Sara died, you just knew what to do with me: you brought me out and supported me in picking up so many new, interesting hobbies (playing bass guitar; bouldering; and even sailing) which I find myself still doing today.

Ilya, thank you for being my housemate and sharing with me the burden of tolerating the scary German guy who lived with us. You are one of the most generous person I have met, always volunteering to help anyone. Also, your cakes are great, keep up the good work!

Verya, I believe you brought every single person in the lab to the climbing gym at least once. It is clear to me that you are on a mission, which I don't fully comprehend; nevertheless, I enjoyed your company and your climbing lessons.

Robert, thank you for your chats on electronics, your humor and your technical help. "Don't panic, ask Robert" was a great piece of advice, which never let me down once.

To all the people in the BME family I send a thank you for the time we shared together and for making me feel part of your group.

A tutti i colleghi del laboratorio MSDLab di Firenze, ci siamo conosciuti lungo un percorso durato anni di sudore scientifico e momenti leggeri e mi ha fatto piacere maturare assieme a molti di voi. Grazie a Riccardo e a Valentino per le grandi feste, sempre rigorosamente a casa di Alex; grazie a Gabriele, per aver esplorato assieme a me il peggio del peggio dell'universo videoludico; grazie ad Alex (Dallai) per aver avuto la voglia di insegnarmi e per la stima dimostrata nelle mie capacità, che spero di continuare a meritare; grazie ad Alessandro (il Rama) per l'amicizia e per tutti i grattacapi di cui non si è mai lamentato ogni volta che gli ho chiesto di modificare Simag; e un sentito grazie anche a tutti gli altri colleghi italiani, dottorandi e dottorati, troppi da ricordare qui ma non per questo dimenticati.

Sara, questo percorso di dottorato non sarebbe mai stato possibile senza il tuo sostegno. Hai sostenuto la mia scelta di imbarcarmi in questa avventura tra due paesi senza lamentarti delle mie lunghe assenze; e quando questo percorso ha iniziato a lasciarmi addosso più frustrazioni che soddisfazioni, hai saputo ascoltarmi e trovare il modo di sostenermi; ed hai poi lasciato che io facessi lo stesso con te, nei tuoi momenti difficili. Accanto a te ho definito il significato di molte parole: felicità, sicurezza, amore. Tutto questo mi manca ogni giorno.

Agli amici di vecchia data, Cosimo e Bernardo, per tutte le sere passate a prendersi in giro e tirarsi su a vicenda. Il mio debito di sonno a causa vostra è grande, ma la gratitudine per il tempo passato assieme lo è ancora di più.

A tutti gli altri amici che mi sono stati particolarmente accanto nel corso di questi ultimi diciotto mesi; a Giacomo e Sara; ad Elisa, che mi ha guidato magistralmente per Bruxelles; e a Marco, che ogni domenica mi guida per mare col team Ariel; a Beatrice e Jacopo; a Martina e Francesco; a Simone, a Filippo, a Luca, per le serate di gioco e per quelle di musica; a tutti questi amici, ed altri ancora, un sentito grazie per il calore e le risate.

Alla mia famiglia; a mia nonna, a mia madre, a mio padre va il ringraziamento più grande di tutti. Per essermi sempre stati accanto, ed in particolare per avermi

sostenuto in ogni modo, economico, morale e materiale, prima ancora che potessi chiedere una mano. Per quello che avete fatto e che state facendo per me dopo la scomparsa di Sara non possono esserci parole adeguate per ringraziarvi. Non potrò mai ripagare quanto avete fatto.

Rik, Piero, Nico, Klazina and Rama, you deserve a very special "thank you" for the help you gave me when I needed it– the most in bringing this book into existence.

Finally, I would like to thank Nintendo, for creating the Wii; and all the people at GBATemp forums and of Team Twiizers who contributed to create the homebrew scene around it: their amazingly well-documented reverse-engineering of the Wii's system software was the most inspiring and fascinating work I have read in years.

Jacopo Viti
Rotterdam, January 2016

List of PhD activities and courses

Seminars and short lectures	Year
"Ultrasound methods for atherosclerosis research and prevention: what next?" (Attending Seminar at the Università di Firenze, Firenze, Italy)	2012
"R&D in Academia and Industry: Which role for the spin-off?" (Attending Seminar at the Università di Firenze, Firenze, Italy)	2012
"Estimating the blood flow velocity using data-adaptive spectral estimation techniques" (Attending Seminar at the Università di Firenze, Firenze, Italy)	2013
IEEE Short course "Ultrafast Imaging of Ultrasound contrast agents"	2014

Symposia and International Conferences	Year
The 16th European Symposium on Ultrasound Contrast Imaging (Rotterdam, The Netherlands) (Poster presentation)	2011
The Artimino Doppler Conference (Artimino, Italy) (Oral presentation)	2011
2011 IEEE International Ultrasonics Symposium (Orlando, FL, USA) (Poster Presentation)	2011
17th European Symposiuum on Ultrasound Contrast Imaging (Rotterdam, The Netherlands) (Poster presentation)	2012
18th European Symposiuum on Ultrasound Contrast Imaging (Rotterdam, The Netherlands) (Poster presentation)	2013
2013 IEEE International Ultrasonics Symposium (Prague, Czech Republic) (Poster presentation)	2013
2014 IEEE International Ultrasonics Symposium (Chicago, IL, USA) (Poster presentation)	2014
20th European Symposiuum on Ultrasound Contrast Imaging (Rotterdam, The Netherlands)	2015

Other activities	Year
Tutoring MS student	2013
Lecturing: practical workshop on programming the ULA-OP at TU/e	2014
Internal presentations at Biomedical Engineering Dept. (cumulative)	2011-2014

Publications

Journal Papers

- **Viti, J**., R. Mori, F. Guidi, M. Versluis, N.D. Jong, and P. Tortoli. "Correspondence - Nonlinear Oscillations of Deflating Bubbles." *IEEE Transactions on Ultrasonics, Ferroelectrics and Frequency Control* 59, no. 12 (2012): -. doi:10.1109/TUFFC.2012.2524.

- Demi, L., **J. Viti**, L. Kusters, F. Guidi, P. Tortoli, and M. Mischi. "Implementation of Parallel Transmit Beamforming Using Orthogonal Frequency Division Multiplexing-Achievable Resolution and Interbeam Interference." *IEEE Transactions on Ultrasonics, Ferroelectrics and Frequency Control* 60, no. 11 (2013): 2310–20. doi:10.1109/TUFFC.2013.6644735.

- **Viti, J.**, F. Guidi, H.J. Vos, N. de Jong and P. Tortoli. "Detection of Contrast Agents: Plane Wave vs Focused Transmission", accepted for publication in *IEEE Transactions on Ultrasonics, Ferroelectrics and Frequency Control* (2015), in press.

Conference proceedings, Abstracts, Posters and Talks

- **J. Viti**, R. Mori, F. Guidi, N. De Jong and P. Tortoli, "Nonuniform oscillations of deflating bubbles – a pilot study", appeared as poster and proceedings for the *2011 IEEE International Ultrasound Symposium*, Orlando, FL, USA.

- F. Guidi, R. Mori, **J. Viti** and P. Tortoli, "An optimal instrument to evaluate the best method for ultrasound contrast imaging", appeared as abstract and poster at the *17th European Conference on Ultrasound Contrast Imaging,* Rotterdam, The Netherlands, 2012.

- F. Guidi, R. Mori, **J. Viti,** N. De Jong and P. Tortoli "Implementation of Arbitrary Contrast imaging Strategies on an US Open Platform", appeared as poster and proceedings for the *2012 IEEE International Ultrasound Symposium,* Dresden, Germany.

- **J. Viti**, L. Demi, L. Kusters, F. Guidi, M. Mischi and P. Tortoli. "Parallel Transmit Beamforming by means of Orthogonal Frequency Division Multiplexing: Implementation on an open research platform", appeared as poster and proceedings for the *2013 IEEE International Ultrasound Symposium*, Prague, Czech Republic.

- **J. Viti,** R. Mori, F. Guidi, N. de Jong and P. Tortoli, "A systematic comparison of contrast imaging strategies", appeared as abstract and presented orally at the *18th European Conference on Ultrasound Contrast Imaging,* Rotterdam, The Netherlands, 2013.

- **J. Viti**, F. Guidi, H.J. Vos, N. de Jong and P. Tortoli "Contrast Detection Efficacy for Plane vs. Focused Wave Transmission", appeared as poster and proceedings for the *2014 IEEE International Ultrasound Symposium*, Chicago, IL, USA.

- D. Peruzzini, , **J. Viti**, P. Tortoli, M. D. Verweij, N. De Jong, and H. J. Vos. "Ultrasound contrast agent imaging: Real-time imaging of the superharmonics." Appeared in AIP Conference Proceedings 1685, presented orally at *Recent developments in nonlinear acoustics; 20th International Symposium on Nonlinear Acoustics including 2nd International Sonic Boom* Forum, Ecully (France (), 29 June-3 July, 2015. American Institute of Physics, 2015.

- **J. Viti**, F. Guidi, H.J. Vos, N. de Jong and P. Tortoli; "Effectiveness and limits of plane wave contrast imaging for moving contrast agents", appeared as abstract and poster at the *20th European Conference on Ultrasound Contrast Imaging,* Rotterdam, The Netherlands, 2015.

About the author

Jacopo Viti was born in Firenze (Florence), Italy on 14 March, 1986. In 2004 he started his university studies in Electronics Engineering at the University of Florence, from which he received his Bachelor degree in Electronics Engineering in September 2007, with a final mark of 110/110 *cum laude*. Later the same year he enrolled in his Master studies in Electronics Design at the same University. During the second year of his Master studies, he spent five months as an exchange student at the Erasmus Medical Center in Rotterdam, the Netherlands, where he started working on characterization of ultrasound contrast agents. In 2010 he received his Master degree in Electronics Engineering from the University of Florence, with a final mark of 110/110 *cum laude*, discussing his thesis titled "Acousto-optical investigation of single microbubble under programmable ultrasound excitation". For this work he was awarded the Chancellor's encomium. In 2011 he simultaneously enrolled in the COEUR Doctoral School at Erasmus Medical Centre, Rotterdam and in the Doctoral School Electronic Technologies for Information Engineering" at the University of Florence, and started working on his PhD on contrast enhanced ultrasound imaging and high-frame rate contrast detection under co-supervision of Prof. Piero Tortoli and Prof. Nico de Jong. Since September 2015 he is working as a consultant on infrared search & track optoelectronics systems at Finmeccanica (Selex ES), Firenze, Italy.